NASA CR-132686

UNSTEADY VORTEX LATTICE TECHNIQUES APPLIED TO WAKE FORMATION AND PERFORMANCE OF THE STATICALLY THRUSTING PROPELLER

by Gerald Forrest Hall

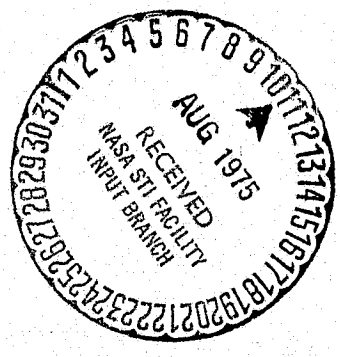

Prepared under Grant No. NGL 39-009-172 by
THE PENNSYLVANIA STATE UNIVERSITY
University Park, PA 16802

for

NATIONAL AERONAUTICS AND SPACE ADMINISTRATION

1. Report No.	2. Government Accession No.	3. Recipient's Catalog No.
NASA CR-132686		

4. Title and Subtitle	5. Report Date
UNSTEADY VORTEX LATTICE TECHNIQUES APPLIED TO WAKE FORMATION AND PERFORMANCE OF THE STATICALLY THRUSTING PROPELLER	6. Performing Organization Code
7. Author(s)	8. Performing Organization Report No.
Gerald Forrest Hall	10. Work Unit No.
9. Performing Organization Name and Address	11. Contract or Grant No.
The Pennsylvania State University University Park, PA 16802	NGL 39-009-172
12. Sponsoring Agency Name and Address	13. Type of Report and Period Covered
National Aeronautics & Space Administration Washington, DC 20546	Contractor Report
	14. Sponsoring Agency Code

15. Supplementary Notes

16. Abstract

The present study is concerned with the application of vortex lattice techniques to the problem of describing the aerodynamics and performance of statically thrusting propellers. A numerical lifting surface theory to predict the aerodynamic forces and power is performed. The chordwise and spanwise loading is modelled by bound vortices fixed to a twisted flat plate surface.

In order to eliminate any apriori assumptions regarding the wake shape, it is assumed the propeller starts from rest. The wake is generated in time and allowed to deform under its own self-induced velocity field as the motion of the propeller progresses. The bound circulation distribution is then determined with time by applying the flow tangency boundary condition at certain selected control points on the blades.

The aerodynamics of other less complex configurations, namely the infinite wing and finite wing, are also considered since many of the numerical problems involved are common with those of the propeller. The details of wake formation and roll-up are investigated, particularly the localized induction effect. It is tentatively concluded that proper wake roll-up and roll-up rates can be established by considering the details of motion at the instant of start. Investigations into blade-wake interference effects and wake-wake interactions lead to the conclusion that an effort is needed to develop vortex core requirements so that the singularity in the Biot-Savart law can be avoided.

17. Key Words (Suggested by Author(s))	18. Distribution Statement
Vortex lattice technique Unsteady aerodynamics Propeller Static thrust	Unclassified - Unlimited

19. Security Classif. (of this report)	20. Security Classif. (of this page)	21. No. of Pages	22. Price*
Unclassified	Unclassified	192	

*For sale by the National Technical Information Service, Springfield, Virginia 22151

Summary

The present study is concerned with the application of vortex lattice techniques to the problem of describing the aerodynamics and performance of statically thrusting propellers. A numerical lifting surface theory to predict the aerodynamic forces and power, including corrections for viscous effects is performed. The lifting surface is replaced by a twisted flat plate which reflects the radial twist distribution of the propeller blades. The chordwise and spanwise loading is then modelled by bound vortices fixed to the flat plate surface.

Since the major problem in predicting statically thrusting propeller performance is the prediction of the wake induced inflow, particular attention is paid to the formation of the wake. In order to eliminate any apriori assumptions regarding the wake shape as well as more accurately describe the physical processes involved, it is assumed the propeller starts from rest. The wake is generated in time and allowed to deform under its own self-induced velocity field as the motion of the propeller progresses. Thus the time history of its shape as well as the inflow at the blades is known. A unique circulation distribution is then determined by applying the flow tangency boundary condition at certain selected control points on the blades. The positions of the control points relative to the bound vortices are fixed by well established rules. The results, with certain reservations, generally point to the usefulness of such a model as a research tool.

The aerodynamics of other configurations, namely the infinite wing and finite wing, are also considered since many of the numerical problems involved are common with those of the propeller but the configurations are much less complex.

The details of wake formation and roll-up are investigated, particularly the localized induction effect. It is tentatively concluded that proper wake roll-up and roll-up rates can be established by considering the details of motion at the instant of start.

Investigations into blade-wake interference effects and wake-wake interactions lead to the conclusion that an effort is needed to develop vortex core requirements so that the singularity in the Biot-Savart law can be avoided while physically realistic flow geometries and performance results are consistently obtained.

Table of Contents

Page

List of Figures

List of Figures (Cont.)

List of Figures (Cont.)

List of Figures (cont.)

NOMENCLATURE

English

A	Bound vortex influence coefficient
AC,BC	Vector lengths from endpoints of a vortex filament, $\underline{X}_A$ and $\underline{X}_B$, to the point at which the induced velocity is calculated, $\underline{X}_C$
B	Number of blades
C	Blade chord, ft.
C_l	Lift coefficient, lift/1/2 $\rho V^2 C$
C_d	Drag coefficient, drag/1/2 $\rho V^2 C$
C_p	Power coefficient, $P/\rho V_T^3 \pi R^2$
C_T	Thrust coefficient, $T/\rho V_T^2 \pi R^2$
E	Coefficient matrix defined by equation (41)
F	Force, pounds
G	Known matrix defined by equation (42)
h	Perpendicular distance from a straight line vortex segment to the point at which the induced velocity is calculated
l	Vector length of vortex segment
M	Mach number
n	Blade number, n = 1,2,...,B
n	Unit normal
NOPAN	Number of spanwise load panels on the lifting surface
num	Number of chordwise vortices modeling loading and shed vortex at trailing edge

List of Figures (Cont.)

p	Pressure, lbs./ft.^{2}
P	Power, ft. sbs./sec.
$\underline{q}$	Vortex self-induced velocity, ft./sec. [equation (19)]
$\underline{r}$	Position vector of point on vortex filament
r	Radius from a vortex to point of calculation of induced velocity (Appendix C)
R	Propeller radius, ft.
S	Lifting surface segment area
$\underline{s}$	Vector length of vortex filament (3.8); coordinate of two-dimensional wake (Appendix C)
T	Thrust, lbs.
t	Time, sec.
$\underline{v}$	Velocity, ft./sec., blade induced; also vortex induced (equation 1)
$\underline{V}$	Velocity, ft./sec.
$\underline{w}$	Velocity, ft./sec., wake induced
$\underline{x}$	Position vector
x,y,z	Orthogonal components of $\underline{x}$, blade fixed except in (3.7) and (3.8) in which they are propeller disc plane fixed. x is directed along the chord, y along the span and z along the axis of rotation; x also is nondimensional propeller radius y/R in (3.12)
x^1,z^1	Section coordinates parallel and perpendicular to the chord respectively; origin at section leading edge.

Greek

α_o	Blade section angle of attack
α, β	Included angles between a vortex segment $\underline{X}_B - \underline{X}_A$ and the radii, $\underline{AC}$, $\underline{BC}$.
β	Blade pitch angle
Γ	Circulation, ft.^{2}/sec.
ζ	Distributed vorticity, ft./sec.
ε	core radius (3.8)
θ	Blade angular position
λ	Local dihedral of blade segment
ρ	Mass density slugs/ft.^{3}
σ	Local blade solidity, BC/R
τ	Time, sec.
ϕ	Velocity potential, ft.^{2}/sec.; blade inflow angle
ω	Propeller rotational speed, rad./sec.

Indices

A,B,C	Identify the endpoints of a vortex filament and the point at which the induced velocity is determined.
e	Effective
h	Hub
i	Induced
i,l	Indices for identifying blade control points; i-chordwise and i=1,2..., num -1; l-spanwise and l=1, NOPAN +1
j,k	Indices for identifying blade bound vortex elements; j-chordwise and j=1, num; k-spanwise and k=1,...NOPAN +1

k	Spanwise position at which wake element end points are shed.
m	Indices defining arms of bound horseshoe filament, m=1,2,3
n	Identifies a particular blade, n=1,2,...,B
p,q	Indices identifying a particular equation in the set of simultaneous equations (40); and a particular unknown in the $p^{\underline{th}}$ equation of that set, respectively
qs	Quasi-static
R	Stacking axis location with respect to section loading edge; also resultant
T	Tip
T.E.	Trailing edge
us	Unsteady
w	Wake
x,y,z	Components in x,y,z direction
	Free stream in flight speed, ft./sec.

Chapter I

Introduction

1.1 General Introduction

With the evaluation and acceptance of helicopters and other VTOL aircraft employing propellers as lifting elements, a greater need exists for the accurate prediction of performance at the early stages of design. With payloads now on the order of 25 percent of the gross weight, a 5 percent error in thrust estimation could mean a 20 percent error in the payload estimate. Thus it is necessary to develop methods for predicting the static (zero forward speed) performance of a propeller to a high degree of accuracy.

The problem is further complicated because economic considerations dictate that the propeller be designed for the mission cruise condition. High speed cruise specifies highly twisted inboard blade sections to maintain efficient loading over as much of the blade as possible, but this then leads to a configuration with a large percentage of the inboard radius stalled during static operation. Thus the static performance prediction problem is magnified by the requirement of extreme accuracy at a decided of design condition.

Comparisons between experimental results and theoretical analysis show predicted thrust values generally to be on the order of 10 percent optimistic. (Refs. 1 thru 13). General lack of knowledge in methods of static performance prediction has been reported by Adams (4) in citing some of the more extreme performance

claims of certain manufacturers. To make matters worse, Borst and Ladden (5) show inconsistencies on the order of 5 percent in figure-of-merit between test results obtained on different test rigs. Jenny, et al. (7) are able to show the sensitivity of hovering rotor performance on the tip vortex axial position and have observed the sensitivity of this location to random wind during open whirl tower tests. With such errors existing between theory and experiment, as well as apparent inconsistent measured values in simply changing installations, the need for a sound analytic base to predict the static performance of a propeller or rotor is apparent.

As in any aerodynamic problem the crux of predicting propeller static performance is the determination of the inflow velocities at the blades. Generally speaking, this inflow is determined by the flight speed and wake induced velocities of the propeller, but in hover the flight speed is zero so the inflow is entirely determined by the induced velocities of the system. The sensitivity of propeller static performance to the inflow can be appreciated when it is realized that for a given error in inflow, the percent error in thrust predicted in hover is approximately twice that in axial flight.

In order to predict the inflow at the blades, it is necessary to describe the blade surfaces and wake. Since the blades are simply lifting surfaces of finite span they can be replaced by a chordwise distribution of bound vorticity. The wakes must consist of vorticity trailing streamwise which accounts for spanwise variation in loading

and, if unsteady motion is present, vorticity must be deposited parallel to the trailing edge to satisfy the Kutta condition. These trailing vortex filaments travel in a generally helical path due to the propeller rotation but do distort under their own self-induced effects and the influence of other filaments. The resulting wake is an extremely complex form consisting of an intense tip vortex and a diffuse inboard sheet. By continuity the wake contracts drawing the tip vortex in radially so that it passes under the next following blade. This blade-vortex interference phenomenon can result in strong radial flows along the blade span and large variations in the radial distribution of angle of attack which, in turn, can promote tip stall.

If the propeller is in axial flight, the flight velocity is the primary factor in establishing the mass flow rate into the wake so that contraction effects can generally be neglected. This velocity also carries the tip vortex away from the disc plane so that it is relatively far removed from the next following blade at the instant of passage. The presence of the axial flight velocity tends to negate the serious interference effects. However, in static operation, the tip vortex remains in the plane of the propeller, drifting only with the induced velocity field, until it is driven axially, almost impulsively, by the next following blade. With wake contraction now important because of continuity considerations, the tip vortex passes under the next following blade at the 80-95 percent blade radius, depending on loading and number of blades.

Hence, for the hovering propeller the blade-wake interference problem is at its worst. Such a wake has been observed physically by several investigators (Reference 12, for example).

It is, in fact, the assumption of axial flight which leads to the classical vortex theory models for the propeller in which the wake is assumed to lie on constant pitch helical sheets. This idealization is permitted by assuming a loading light enough so that the induced velocity field is negligible regarding wake contraction, deformation and interference. Further, the solution to these models depend on normality relations between the induced velocity components in the ultimate wake. Considering the restrictions on the propeller and wake model implied by the axial flight velocity, it is not surprising that the representation becomes invalid in the static operation.

The classical vortex models as well as most ensuing ones generally neglect the chordwise variation of loading by simply replacing each blade by a concentrated bound vortex, a Prandtl lifting line model. Unfortunately, the strong radial flows noted in the vicinity of the blade-vortex interference region and the highly twisted inboard sections imply three-dimensional effects not adequately treated by such a simplification. These considerations can be quite far-reaching since they not only affect the lift loading but also the viscous boundary layer and so can alter considerably the drag characteristics. The boundary layer characteristics on propeller and rotor blades are quite complex and any attempt at

analyzing them requires a reasonable estimate of the pressure distribution.

A lifting line model requires implicit satisfaction of the flow tangency boundary condition at the blade surfaces. This means the wake geometry must be completely described before the loading can be determined, leading to either a semi-empirical method or an analytical method involving an iterative technique. The former correlates experimentally determined wake shapes with propeller design parameters and loading, and its accuracy is bounded by experimental accuracy and the particular parameters investigated. The latter assumes an initial wake shape, and then allows the wake to convect under its own induced velocity field to a final shape with the blade loading adjusting itself under the changing inflow to a value consistent with the final deformed wake shape. A typical procedure is to begin with an initial wake geometry and wake circulation distribution based on a given bound circulation distribution. The wake points are then allowed to convect under the induced velocity field until a wake geometry consistent with this circulation distribution is attained. The deformed wake alters the inflow which changes the bound circulation distribution which fixes a new geometry. The iterations are continued until a compatible wake geometry-circulation distribution is attained. Unfortunately, some evidence exists that the accuracy of the solution depends on the initial assumed values; certainly the rate of convergence of such a ponderous technique depends on how accurate are the initial assumptions.

The aerodynamics of the statically thrusting propeller depends entirely on the inflow as determined by the induced velocity field and this, in turn depends entirely on an accurate wake geometry. It has been shown too that a strong interference problem between a wake and the blades exists even after a final steady flow geometry is attained. This leads to considerations of the wake which until recently have received very little attention, notably the roll-up characteristics of the individual blade wakes. Historically, little interest has been shown in this area, probably because the vortex wake roll-up has negligible effect on the loading of the generating surface. What interest has developed has been in the area of wing wake interference with the tail-plane of an aircraft. Renewed interest has been generated along the same lines with regard to highly loaded V/STOL aircraft. However, the aerodynamic interference between propeller blades and their wakes is essentially the same problem so that accurately prescribed roll-up characteristics may be quite important in predicting an accurate wake geometry.

Apparently, then, what is needed to form a solid base for the prediction of propeller static performance is a completely analytical model of the propeller and wake system which can generate consistent wake (i.e., inflow) and loading conditions for arbitrary design parameters and which are flexible enough to consider three-dimensional flow considerations at the blades.

1.2 Statement of the Problem

The purpose of this investigation is the development of an analytical method for the prediction of propeller and rotor static performance. The method is to be general enough to permit determination of the blade pressure distribution. This implies an ability to consider blade aeroelastic and boundary layer characteristics, if desired, since these are both dependent in some measure on the shape of this distribution while performance is more or less dependent on the chordwise integrated value. This imparts no particular hardship since three-dimensional effects due to the strong radial flows in the vicinity of the blade-vortex interference region and the highly twisted inboard section must be treated. Hence lifting surface theory will be applied instead of the usual lifting-line theory.

As observed previously, the problem in determining the static performance lies in determining the correct inflow distribution which means knowing the correct wake shape. In order to eliminate any assumptions or empirical restrictions regarding wake shape it can be noted that the inflow is known exactly at one instant of time for any propeller; namely, at the instant of start of the propeller motion. Since no wake exists at this instant, the inflow is entirely determined by the blade motion. As the motion progresses, the wake is deposited and deforms continuously under its own self-induced effects until a final shape such as observed in Reference (12) is established. This means the inflow and therefore the loading change

continuously in time until the final wake is established and a steady state performance is reached. Essentially, the wake formation is treated as an initial condition problem in time. Such a formulation implies an unsteady aerodynamic analysis for propellers similar to the classical Wagner problem of fixed-wing aerodynamics.

Treating the wake as an initial condition problem gives rise to a completely different wake model during the response of the flow to the impulsive start. It has been observed physically that an impulsive thrust change by an impulsive change in either propeller rotational speed (14) or blade angle (15) results in a doughnut shaped starting vortex forming in the propeller plane and moving axially as a unit after the new thrust level is reached, leaving a wake as described in Reference (12) trailing from the blades.

The method of this investigation treats the wake formation of the statically thrusting propeller as an initial condition problem in time. Since lifting-surface theory is to be used and the wake generated serially in time with the inflow known at each instant, the flow tangency boundary condition and Kutta condition can be uniquely satisfied at each instant of time giving the bound vortex distribution explicitly. The loading is then determined by applying the unsteady Bernoulli equation.

Since a major element of the analysis is the self-convection of the wake, a nonlinear flow problem exists which precludes any hope of closed form solution. Therefore, numerical techniques are used, particularly vortex lattice methods. Such models represent

the simplest techniques, contain all the essential aerodynamics of the blades and wake and are most amenable to the nonlinear flow problem.

In summary, then, the problem to be investigated consists of applying numerical unsteady lifting-surface theory based on vortex lattice techniques to the problem of a propeller starting from rest. The wake is allowed to generate and deform under its own self-induced effects, thus presenting a consistent time history of the wake formation, blade inflow and blade loading as the motion progresses. Wake self-induced effects are due to the classical far-field effects as well as localized effects. Once the wake and inflow distributions are formed according to a potential flow model, final performance results are obtained by correcting for real fluid effects with existing airfoil data.

Chapter II

Previous Investigations

2.1 Propeller/Rotor Characteristics

A survey of the literature concerning propeller/rotor operating characteristics reveals the effects of the major design parameters on the static performance. Reference (5) contains a parametric study of the effects of these design parameters on the figure of merit. The results show an increase in the power coefficient for peak figure of merit as blade activity factor increases. Above peak figure of merit blade angle seems to have little effect on performance but peak figure of merit is reduced with increasing blade angle toward the tip; hence, performance at the highest efficiency is very sensitive to blade loading. Finally, figure of merit increases with increasing Reynolds' number, indicating difficulties in applying model results to full scale. Chopin (8) has performed a parametric study of a statically thrusting propeller including the effects of tip shape, twist, blade activity factor, total activity factor, blade camber and airfoil section. The results, in general, agree with those of Reference (5) in addition to which it is shown that camber increases the thrust coefficient at a given power coefficient, becoming more evident at the higher power coefficients. Round tips are seen to improve performance over square tips near the best lift-drag ratio but the advantage decreases as the power coefficient increases. While absolute performance values might be questioned due to the accuracy of the test facility (Reference (5)), the changes due to varying the design parameters should be quite good.

Attempts have been made to measure the pressure distributions on the blades of hovering rotors and statically thrusting propellers. Rabbott (2) showed that chordwise loadings maintain essentially classical form out to 95 percent radius with only minor differences in the vicinity of the trailing edge near the tip. Such differences might be expected to alter the aerodynamic moment but have little effect on performance. However, the spacing of the pressure taps was not fine enough to observe the flow details at the tip. Gilmore (9) has made extensive measurements of propeller blade chordwise pressure distributions showing a strong three-dimensional effect near the tip. Unfortunately, the reduced data yields integrated results which are implausible at best and measured forces show nonrepeatability as high as 50 percent, making the results in general suspect. It should be mentioned, however, that inboard of 95 percent radius the chordwise pressure distributions are similar to the classical forms.

The classical methods used to predict performance are mainly those analyses originally derived for axial flight and suitably modified for the static case. These methods, the Rankine-Froude momentum theory, the combined momentum-blade element theory and the vortex theories of Prandtl and Goldstein are well-known and can be found in the literature (16, 17, 18, for example). The Rankine-Froude theory assumes the propeller to be replaced by an actuator disc. The actuator disc is uniformly loaded and so develops a uniform axial induced velocity. The theory deals with average performance values and does not give detailed information on the blade loading and induced velocity distribution. The combined momentum-blade element theory attempts to remove the uniform inflow assumption by

balancing the blade thrust against wake momentum in radial annuli. Prandtl's vortex theory shapes the radial inflow distribution by assuming the flow in the ultimate wake to be very nearly like the flow exterior to an infinite number of semi-infinite strips. The results are expressed in terms of a tip-loss factor dependent on the number of blades, radial position and the wake helix angle at the tip. The vortex theory of Goldstein defines the inflow by assuming the ultimate vortex wake to lie on rigid helicoidal surfaces of fixed pitch. The results are expressed in a semi-infinite series of modified Bessel functions and cannot be easily handled for the general case without the aid of high-speed computation devices. It should be mentioned that with the advent of such aids in recent years, Goldstein's analysis has become more or less the standard classic analysis since it would appear to represent the most exact model. Prandtl's theory is easier to use since it is expressible in a single closed form and has been used successfully in propeller design (17). In one instance (2), it was even more accurate in predicting performance than Goldstein's analysis.

Reference (7) presents a correlation of conventional methods of hovering rotor performance showing a tendency to underpredict the power at given thrust by as much as 50 percent depending on blade loading, number of blades, tip Mach Number and twist. Generally, the predictions become more optimistic as these quantities increase. It is also shown that empirical correction factors to correlate experiments with theory developed for one configuration cannot be confidently generalized for another design.

Attempts at predicting rotor inflows have followed two courses, semi-empirical and analytical. The complex flow field of the steady state propeller has been visually observed and reported in References (4,7,10,12,19). This has led to experimental determination of wake position as a function of the propeller design parameters. This approach was initiated by Jenny, et al. (7) for a hovering rotor and extensively investigated by Landgrebe (12). It is shown in Reference (12) that: (1) the tip vortex axial coordinate before interaction by the next following blade is primarily a function of the blade loading and twist while following the intersection the primary dependence is on momentum induced velocity, i.e., proportional to $\sqrt{C_T}$; (2) the radial coordinate is primarily a function of thrust coefficient or disc loading; and (3) the inboard sheet coordinates are principally functions of the momentum induced velocity. Based on this study, empirical determination of the wake trajectory general enough to apply to a wide class of rotors is carried out.

Ladden (10) has applied Landgrebe's technique to 3- and 4- bladed propellers. The results in general fortify those of Reference (12) except that the axial coordinate after intersection by the next following blade seems to exhibit a weak dependence on the number of blades as well as thrust coefficient. Both Reference (10) and Reference (12) show the sensitivity of performance to the tip vortex location.

Analytical approaches to inflow prediction for the hovering

rotor were preceded by models developed for the rotor in forward flight. In general these methods utilize lifting line theory and some iterative techniques to determine a realistic wake. Vortex lattice techniques representing the wake by vortex segments are used to treat the deforming wake. The first of these methods was that of Piziali and DuWaldt (20) for investigation of harmonic airloading on the rotor in forward flight. The vortex wake is broken up into straight line segments with shed and trailing filaments lying on a prescribed trajectory and strengths determined by the time rate of change of bound vorticity and the blades replaced by lifting lines. The wake is truncated after approximately three revolutions. Crimi (21) attempted to include realistic wake effects by replacing the blade wake by a single tip vortex with a rotational core and a strength changing with the bound circulation. The trajectory of this vortex is prescribed, but as the blade moves, it is allowed to move (deform) under the ensuing induced velocity field. The segments of the vortex are taken to be straight line segments with curvature accounted for locally. The blades again are lifting lines. Trenka (22) applied the model of Reference (20) to a VTOL propeller, attempting to account for wake contraction by determining an axial contraction envelope from the trajectories of ring vortices shed below the propeller. Scully (23) represented the rotor by two trailing vortices with deformation permitted and was able to show that accurate inflow prediction required inclusion of both shed and trailing vorticity effects. A model by Landgrebe (24) treats each wake point as having a near

field in which deformation velocities depend on the local geometry and a far field in which the velocities are well represented by average values determined from an initial undistorted wake model.

Static operation of the propeller has been investigated directly by Erickson and Ordway (6). The blades are represented by single bound vortices and the wake by continuous vortex sheets. The model described attempts to account for the continuous deformation of the vortex sheets. The performance is determined by guessing at the inflow (thus the blade circulation) and the induced velocity field in the wake. Application of integral operators (The Biot-Savart Law) while allowing the wake to deform under the force-free condition and applying iteration techniques permit convergence to the final induced velocity field. The performance is then determined. The prominent result determined here is the dependence of the final results on the initial assumed inflow distribution. The method is extended by Erickson (25) in which heavily loaded actuator disc theory is used to fix the wake contraction. The results in general fortify those of Reference (6) in that the final results depend on the assumed initial ones. One important addition, however, is that the axial induced velocity over the chord varies sufficiently that large induced camber exists which negates lifting-line models and requires lifting-surface considerations.

Clark and Leiper (26) utilize a wake model which does start with an assumed shape and converges to a final, force-free and realistic deformed shape while predicting accurate performance. This model computes an induced velocity field at carefully selected

field points near the rotor and the wake is allowed to deform as it passes through this velocity field. The problem is a boundary value problem with the accuracy dependent on the selected field points. Rorke and Wells (27) having managed to combine the theory of Reference (26) and the experimental investigation of Reference (7), are able to formulate a wake which can be used to modify the combined momentum-blade element theory so that accurate performance estimates can be made for a wide range of rotors in the hover mode. Landgrebe (28) has compiled an extensive bibliography of propeller and rotor inflow prediction methods.

A significant deviation from the analytical models previously described is provided by Sadler (29). Instead of assuming an initial wake geometry and circulation distortion and iterating to a consistent wake geometry-circulation distribution model, he performs the simple expedient of letting the rotor start from rest, impulsively, while letting the wake generate and convect under its own induced velocity field as time progresses. This is simply the classic Wagner problem of fixed wing aerodynamics applied to the rotor. The wake geometry and circulation distribution are thus compatible at each instant of time. Local induced effects are included as by Crimi (21). The loading is modeled with lifting-line theory. The cases run are fairly coarse models of the forward flight rotor, and downstream truncation and neglect of shed vorticity in the wake may influence the results, but in principle this represents the most physically realistic approach to the problem.

2.2 Numerical Techniques

The accurate determination of inflow to a statically thrusting propeller or rotor system depends on the solution of a nonlinear flow problem. The problem will be treated in classical fashion by replacing the propeller blades and wake by distributed vorticity and treating the ensuing disturbance motions as a potential motion. The complexity precludes any hope of a closed form solution; hence, numerical methods employing vortex lattice techniques are used. A fairly complete bibliography of numerical lifting surface theory to 1968 is given by Landahl and Staark (30) which certainly shows the attention given these methods, particularly since the advent of high-speed digital computation techniques. Vortex lattice techniques have their foundation in the work of Falkner (31,32) in which finite wings in steady flight, with and without twist, were considered. The problem is solved by satisfying the flow tangency boundary condition at selected control points on the surface. In order to minimize computational details special loading functions are used. Kulakowski and Haskell (33) investigated the twisted delta wing case utilizing high-speed digital computers. An extensive numerical analysis of the steady motion of arbitrary planforms is performed by Rubbert (34). In this method the bound vorticity is determined directly, eliminating the need for special loading functions. Hedman (35) applies the same model to the quasi-steady problem while utilizing locally swept spanwise vortices in his model. Belotserkovski (36) treats a similar model but allows for vorticity to be shed all along the chord in response to unsteady motion.

The results of numerical analysis will depend on the locations of the vortices and the boundary control points. The proper chordwise positioning is indicated by Falkner (31,32) utilizing two-dimensional considerations and verified numerically by Rubbert (34). Reference (34) also evolves rules for handling spanwise spacing and the tips; it is noted that spanwise spacing is not too critical and that generally a constant (regular) or cosine law can be used. The chordwise spacing is verified in a more general sense by James (37) for two-dimensional steady motion by requiring both loading and moment to be accurately determined by the numerical results. This chordwise spacing consists of the following: if the wing is broken up into a number of chordwise segments, vortices placed on the 1/4-chord of the segments and the tangency condition satisfied at the 3/4-chord points will yield the proper chordwise loading and aerodynamic moment. DeYoung (38) shows the loading developed for this spacing converges to the classic form for an infinite number of chordwise panels.

2.3 Vortex Wake Roll-Up

The wake roll-up problem was studied initially by Kaden (39), both analytically and experimentally. The wake behind a wing is assumed to be initially a flat vortex sheet. A Trefftz plane analysis which assumes geometrically similar flow in any transverse plane behind the wing is performed. In treating the wake Kaden also assumed it is necessary to consider only one tip so that for

analysis the semispan of the wake is stretched into a semi-infinite length. The problem is then solved by treating the unsteady deformation of this semi-infinite strip of discontinuous potential in time, the result being the equation of a spiral.

Westwater (40) performed a numerical analysis on the roll up problem by replacing the continuous distribution of wake vorticity by 20 discrete vortices. The unsteady problem of determining the velocities and displacement of the individual vortex filaments over finite time intervals is performed with the wake assumed flat initially. The trailing vortices are assumed to be doubly infinite which implies a Trefftz plane analysis and two-dimensional flow. Westwater does test this assumption and finds that at about two spans downstream the flow is essentially two-dimensional.

Hackett and Evans (41) extend the Westwater model to wings with sweep, geometric incidence, high lift coefficients, ground effect and wind tunnel wall constraint. The finite upstream length of the trailing vortices and the wing bound vortex system are included. They expect geometric incidence to lower the whole sheet by an amount determined by the trailing edge position. Variation in lift coefficient has its major effect on streamwise length scales measured from the trailing edge, i. e., halving the lift coefficient doubles the downstream distance to a given roll up pattern. It is also implied that better roll up patterns are obtained by using equi-spaced, variable strength vortices rather than variable spaced, equal strength vortices. Numerical problems that can arise are

illustrated by a case in which the vortex sheet crosses itself, a physical impossibility.

Butter and Hancock (42) utilize a similar model but numerically somewhat cruder, i. e., fewer vortices and longer time steps. They experienced no difficulty in the program more by "good fortune than numerical insight", but correlation with experiment is not particularly good. They do note that current wake roll up models utilize Trefftz plane analyses.

Wilson (43) presents an analysis of wake roll up which departs from the Trefftz plane analyses of most investigators. The wing is allowed to start from rest so that the wake is generated in time and allowed to convect under its own self-induced velocity field. The model is somewhat constrained since the loading is held constant but this does eliminate the existence of shed vorticity in the wake. Also, no deformation of the starting vortex is permitted. The induced velocity field is computed in a more or less classical manner with the trailing vorticity laid down in straight line segments describes the wake motion. The induced velocity is calculated at the end points by application of the Biot-Savart law but no local effect, i. e., the effect of the vortex filament in the region near the point in question, is considered; this is usual in such a model since standard application of the Biot-Savart law results in an infinite velocity when the point at which the velocity is calculated lies on a vortex filament. Wilson's model yields reasonable wake geometries with the outboard filaments rolling up

into an intense tip vortex which remains near the plane of the wing while the inboard vortices remain in a diffuse sheet and are convected downward much faster. The results compare favorably at least qualitatively with other analyses and experiments.

Jordan (44) questions the Westwater approach on the argument that roll up in his model is initiated by an artificial disturbance in the downwash field which is created by the replacement of the continuous sheet by a finite number of vortices. In the finite vortex representation, a given vortex convects under the velocity induced by all other vortices. According to Jordan's arguments there is a definite deficiency in this velocity due to what amounts to be the effect of that part of the continuous distribution that is replaced by the discrete vortex in question. This downwash deficiency is the artificial disturbance which initiates the roll up of the flat sheet.

Jordan (44) further notes the failure of standard analyses to predict the correct roll up rate; typically these rates are much too slow. He places the blame on classical aerodynamic theory and the elliptic loading. As a consequence he presents an analysis which contains a logarithmic singularity just inside the tip at the trailing edge and claims this singularity will drive the roll up at a much faster rate. Unfortunately, he presents no hypothesis as to what this singularity might correspond physically.

In summary, it must be concluded that relatively little is presently known regarding the mechanism of vortex wake roll up as well as the numerical modelling of the phenomenon. Yet it promises

to be an important consideration in the determination of the interference characteristics of the statically thrusting propeller. A more complete bibliography of wake roll-up considerations can be found in the survey report by El Ramly, Reference (45).

Chapter III

Theoretical Considerations

3.1 Assumptions

Consistent with classical lifting aerodynamic theory the disturbance in the fluid created by the lifting blades and wakes is assumed to be a potential motion. This permits a lifting blade and wake to be replaced by a continuous sheet of distributed vorticity. The disturbance velocity is then given by the Biot-Savart law and the pressure field by the classic unsteady Bernoulli equation. The problem is solved at each instant in time for unknown bound vortex strengths by satisfying the tangency boundary condition on the blades, $\underline{V} \cdot \underline{n} = 0$ where $\underline{V} = \underline{V}_\infty$(Blade Motion) + $\underline{w}_i$ (Wake Induced) + $\underline{V}_i$ (Blade Induced) and $\underline{n}$ = Unit Normal on Blade Surface at each instant of time. The problem is time dependent, since $\underline{V}_\infty$ can be time dependent and the wake continuously deforms so that $\underline{w}_i$ and $\underline{v}_i$ are, in the general case, also time dependent. Thickness effects are neglected so the load generating surface is approximated by a cambered twisted plate; hence, the boundary condition satisfied by the bound vortices is applied to this cambered, twisted plate. With the blades so approximated, the planar wing assumption is applied so that the camber is taken to be small with respect to the chord. This amounts to placing the bound vortices on a twisted flat plate. Finally, it is noted that vorticity comprising the wake consists of two types. One is shed vorticity which is laid down initially parallel to the trailing edge and the other is trailing vorticity which provides for

spanwise variations in loading and is initially parallel to the blade chord.

The propeller is assumed to be operating in hover, i. e., a statically thrusting propeller. The "$\underset{\sim}{V}$" of the blade is just due to rotation; in general no flight speed exists. This simplifies the problem somewhat in that azimuthal symmetry for a multi-blade configuration exists which will allow the problem to be solved on one reference blade with identical conditions existing on the other blades. The following analysis considers only one blade and its wake with the necessary symmetry conditions for the multi-blade configuration discussed in Section (3.10).

The blade is taken as rigid so no blade flapping or aeroelastic motions are considered. These could of course be included in the "$\underset{\sim}{V}$" term, however.

3.2 Description of the Numerical Model

The numerical model for the blade and its wake consists of replacing the continuous distribution of vorticity by a mesh of vortex segments of finite length and strength. The geometry of the wake vortices is fixed by the motion of an ever increasing number of points moving under the influence of the bound vorticity and its own self-induced effect since it is assumed that these wake points are connected by straight-line vortex segments identified as shed and trailing vorticity. The description of the blade bound vortices is fixed by the blade geometry.

The vortices on the surface are arranged in a conventional

manner. The surface is broken up into a number of spanwise segments and each spanwise segment is subdivided into a number of chordwise segments. Each resulting panel contains a control point and is spanned by a straight-line vortex segment. The lifting surface planform is variable and the panel corners occur in pairs along the span located at the same percent local chord; hence, the spanwise vortex on a segment has sweep reflecting the variable chord. This vorticity must be supplied and removed according to the Helmholz law so the vortex is extended along the local chords at spanwise edges of the panel to the vortex lying along the trailing edge of the surface (this vortex is shed into the wake at the end of a time step to be replaced by another reflecting the time rate of change of bound circulation). This describes a rectilinear horseshoe vortex model like those of references (31, 32, 34, 35, 36) except that instead of extending to infinity as in the steady and quasi-steady cases they are truncated at the vortex to be shed. One major difference exists, however. The blade twist is reflected in the model, in part, as a skew to the horseshoe vortex since the chordwise elements are skewed with respect to each other. Hence, the configuration is highly nonplanar since for a propeller the twist distribution can be much greater than for a typical wing. For the horseshoe representation the twisted flat plate becomes a segmented (spanwise) plate with each segment being flat but having a different spatial orientation from its adjacent segments.

One requirement of this straight-line representation is that

the spanwise segments be small enough that the chord variation is adequately represented by straight-line segments between y and $y + \Delta y$. Typical airplane propellers and rotors will fulfill this adequately except perhaps at the tips. In keeping with well-documented methods of vortex lattice theory (31, 32, 34, 35, 36) based on two-dimensional analysis and Weissinger's lifting surface theory and recently verified for the two-dimensional case (37, 38), the proper load on a segment is obtained by determining the flow deflection at a point one-half the segment chord length from the vortex. Hence, the control points are located on the local chord $c(y + \frac{\Delta y}{2})$ with a chordwise spacing equal to one-half the segment chord from the spanwise vortex. In order to obtain the correct aerodynamic moment, the spanwise vortex must be located at one-quarter segment chord from the segment leading edge. Thus the first spanwise vortex filament lies at the 1/4-segment chord back from the leading edge. The final spanwise filament is 1/4-segment chord downstream from the blade trailing edge; this implies that the Kutta condition is satisfied approximately, the accuracy of approximation increasing as the number of chordwise segments increases. The first control point lies at 3/4-segment chord behind the blade leading edge, the last one at 1/4-segment ahead of the blade trailing edge. Figure (1) shows an example of this vortex system on an arbitrary spanwise panel.

3.3 Coordinate Systems

In dealing with propellers and rotors various coordinate systems exist and are convenient to consider for various calculations.

(1) Blade Fixed: An orthogonal system with the origin fixed at the axis of rotation, y directed along the span, x along the chord and z along the rotation vector. Hence, x and y lie in the disc plane and rotate with the blade. This system is convenient for blade force determination.

(2) Propeller Disc-Plane Fixed: This is a typical wind-tunnel configuration and allows a wake visualization as might be seen in a wind tunnel or whirl tower. x and y are orthogonal but fixed in direction so the blades rotate relative to them. z is also perpendicular to the disc plane. Wake deformation will be considered in this system.

(3) Fluid at Rest Fixed: Allows visualization of the wake at one position as a function of time as the rotating propeller passes with some flight speed. This is a spatially fixed Cartesian system. In general, concern is directed toward (1) and (2) but note that (2) and (3) coincide for the statically thrusting case. Figure (2) shows coordinate systems (1) and (2).

3.4 The Elementary Flow Field

Since the disturbance created in the fluid is a potential flow, the application of vortex lattice techniques is permitted. As previously described, the blade surfaces are replaced by a mesh of rectilinear vortices in order to approximate the continuous distribution with numerical analysis. Further, since small but finite time increments are considered, the wake contains a finite number

of points whose motion describes the deformation. These points are taken to be connected by straight line vortex segments which represent the disturbance. Hence, at a point in space and time, the elementary flow field is that due to a straight line vortex segment.

Referring to Figure (3), for a straight line vortex segment with end points at $\underline{X}_A$ and $\underline{X}_B$, a velocity at $\underline{X}_C$ is induced according to the Biot-Savart Law

$$\underline{V}_i = \frac{\Gamma}{4\pi} \frac{\cos\alpha + \cos\beta}{h} \underline{n} \tag{1}$$

where $\underline{n}$ is the unit normal perpendicular to the plane containing $\underline{X}_A(t)$, $\underline{X}_B(t)$, and $\underline{X}_C(t)$.

Now,

$$\underline{n} = \frac{\underline{1} \times \underline{AC}}{|\underline{1} \times \underline{AC}|} = \frac{\underline{1} \times \underline{AC}}{|\underline{1}| \ |\underline{AC}| \sin\alpha} \tag{2}$$

and $h = |\underline{AC}| \sin\alpha$

So that expanding $\underline{1} \times \underline{AC}$ yields the X, Y, Z components of $\underline{v}_i$ from

$$\underline{v}_i = v_{i_x} + \underline{j}\, v_{i_y} + \underline{k}\, v_{i_z}$$

$$v_{i_x}(\underline{X}_C, t) = \frac{\Gamma(t)}{4\pi} \frac{\cos\alpha + \cos\beta}{|1| \ |\underline{AC}|^2 (1 - \cos^2\alpha)} [(Y_B - Y_A)(Z_C - Z_A) - (Y_C - Y_A)(Z_B - Z_A)]$$

$$v_{i_y}(\underline{X}_C, t) = \frac{\Gamma(t)}{4\pi} \frac{\cos\alpha + \cos\beta}{|1| \ |\underline{AC}|^2 (1 - \cos^2\alpha)} [(Z_B - Z_A)(X_C - X_A) - (X_B - X_A)(Z_C - Z_A)] \tag{3}$$

$$v_{i_z}(\underline{X}_C, t) = \frac{\Gamma(t)}{4\pi} \frac{\cos\alpha + \cos\beta}{|1| \ |\underline{AC}|^2 (1 - \cos^2\alpha)} [(X_B - X_A)(Y_C - Y_A) - (X_C - X_A)(Y_B - Y_A)]$$

Superposition of the results of equations (3) for all the elements of the vortex mesh representing the blades and wakes give the components of disturbance velocity at any point in the field.

The form of equations (3) is suitable for the vortices fixed to the lifting surface since the geometry is fixed. For the wake vortices which are free to deform while conserving total circulation according to

$$\Gamma(t)\,|\underline{l}(t)| = \Gamma(\tau)\,|\underline{l}\,(\tau)| = \text{const.}\quad t>\tau \tag{4}$$

where $\Gamma(\tau)$, $l(\tau)$ are the circulation and length at the time of shedding, τ, respectively. It is convenient to use

$$\Gamma(t) = \frac{\Gamma(\tau)\;|\underline{l}(\tau)|}{|\underline{l}\,(t)|} \tag{5}$$

and rewrite the Biot-Savart Law in the form

$$\underline{v}_i = \frac{\Gamma(\tau)\,|\underline{l}(\tau)|}{4\pi}\;\frac{\cos\alpha + \cos\beta}{|\underline{l}(t)|\,h}\;\underline{n} \tag{6}$$

which has components similar to equations (3).

3.5 Influence Coefficients for the Twisted, Cambered Plate

The influence coefficients are simply the normal component of velocity induced by the q^{th} unit strength horseshoe vortex on the lifting surface at the p^{th} control point. The q^{th} horseshoe vortex is identified in a coordinate system rotating with the blade. The origin lies on the axis of rotation with y coinciding with the stacking axis and x parallel to the chord. The p^{th} coordinate system is located the same way. Now if we imagine i, j to represent the chordwise coordinate and k, l, the spanwise coordinate, the horseshoe vortex is identified by the coordinate of the left hand corner

nearest the leading edge $\underline{x}_{jk}$. The point $\underline{x}_{jk}$ has the Cartesian coordinates $\underline{x}_{jk} = \underline{i}\, x_{jk} + \underline{j} y_k + \underline{k}\, z_{jk}$. The control points are similarly identified by $\underline{x}_{cil}$. Figure (4) illustrates the convention for defining the vortices and control points.

The normal component of velocity induced at $\underline{x}_{cil}$ by the j^{th} unit strength horseshoe vortex is

$$v_n(\underline{x}_{cil}) = \sum_{m=1}^{3} \left[\frac{\cos\alpha + \cos\beta}{4\pi |\underline{l}|\ |\underline{AC}|^2 (1 - \cos^2\alpha)} (\underline{l} \times \underline{AC}) \right]_m \cdot \underline{n}\,(\underline{x}_{cil}) \quad (7)$$

where $\underline{n}$ is the unit normal at $\underline{X}_{cil}$ and m identifies a particular segment in the horseshoe filament. The coordinates associated with one vortex filament are $\underline{x}_{numk}$, $\underline{x}_{jk}$, $\underline{x}_{jk+1}$, $\underline{x}_{numk+1}$, starting at the trailing edge (shed vortex) and progressing clockwise around the vortex so that the filament has a horseshoe shape (see Figure (4)). "Num" identifies the trailing edge vortex whereas j identifies the chordwise position of the spanning element.

Thus,

$$v_n(\underline{x}_{cil}) = \sum_{m=1}^{3} (v_{x_m} n_x + v_{y_m} n_y + v_{z_m} n_z) = \text{influence coefficient},$$

$$A_{pq} \quad (8)$$

where v_{x_m}, v_{y_m}, v_{z_m} are given by equation (3). The indices p and q give the velocity induced at the p^{th} control point by the q^{th} rectilinear filament where p and q are serially numbered starting at the left-hand leading edge panel and progressing chordwise over the surface ending at the right-hand tip trailing edge (see Figure (4)). Note that A_{pq} due to a trailing edge vortex segment which is shed into the wake is due to a straight-line segment, a degenerate form

of the basic horseshoe configuration of the bound vortices.

The unit normal, utilizing strip theory for the moment, is given by

$$\underline{n}(\underline{X}_{cil}) = \underline{i} \sin\left(-\frac{dz'}{dx'}_{il}\right) + \underline{k} \cos\left(-\frac{dz'}{dx'}_{il}\right) \tag{9}$$

where x', z' are coordinates parallel and perpendicular to the blade chord, respectively. If the chord is pitched through an angle β_{C_l} with respect to the disc plane,

$$\underline{n} = \underline{i} \sin\left[\beta_{C_l} - \left(\frac{dz'}{dx'}\right)_{il}\right] + \underline{k} \cos\left[\beta_{C_l} - \left(\frac{dz'}{dx'}\right)_{il}\right] \tag{10a}$$

so that

$$n_x = \sin\left[\beta_{C_l} - \left(\frac{dz'}{dx'}\right)_{il}\right]$$

$$n_y = 0$$

$$n_z = \cos\left[\beta_{C_l} - \left(\frac{dz'}{dx'}\right)_{il}\right]$$

Including the effect of twist in satisfying the boundary condition it can be seen that within the limits of the model each spanwise segment has an effective dihedral. Thus, the unit normal has components

$$\begin{aligned} n_x &= \sin\left[\beta_{C_l} - \left(\frac{dz'}{dx}\right)_{il}\right] \cos\lambda_{il} \\ n_y &= \sin\lambda_{il} \\ n_z &= \cos\left[\beta_{C_l} - \left(\frac{dz'}{dx'}\right)_{il}\right] \cos\lambda_{il} \end{aligned} \tag{10b}$$

where λ_{il} is this dihedral angle.

Figure (5) shows the geometry of the unit normal. Referring to Figure (5) the local dihedral of the panel segment is taken to be the slope of the straight line joining the chordwise bound vortices

at the location of the control point. For the control point, i.e., the panel segment is bounded by chordwise vortices at k and k+1. The z-displacement of k^{th} vortex element at x_{cil} is $(-x_{cil} \tan \beta_k)$ and for the k+1 element, $(-x_{cil} \tan \beta_{k+1})$. The slope defining the dihedral then is just

$$\lambda_{il} = - \tan^{-1} \frac{-x_{cil}}{\Delta y_1} \{[\tan \beta_{k+1} - \tan \beta_k]\} \tag{11}$$

from which $\sin \lambda_{il}$, $\cos \lambda_{il}$ can be determined.

3.6 The Boundary Condition

The unknown vortex strengths are determined by satisfying the boundary condition $\underline{V} \cdot \underline{n} = 0$ at all control points which, in matrix form, is expressed as

$$A_{pq}\Gamma_q = - V_{np} \tag{12}$$

where V_{np} is the resultant normal component of all the externally applied velocities as the p^{th} control point. For the propeller in hover this is rotational motion of the blade and the wake induced velocity.

$$\underline{V} = \underline{r} \times \underline{\omega} + \underline{w}_i(t) \tag{13}$$

where $\underline{r}$ is from the axis of rotation to the control point in the disc plane and $\underline{\omega}$ is parallel to the z-axis. $\underline{w}_i(t)$ is the induced velocity of the wake at the control point. Thus,

$$\begin{aligned} V_{np} &= (\underline{r} \times \underline{\omega} + \underline{w}_i(t)) \cdot \underline{n} \; (\underline{X}_c) \\ &= [\omega y_1 + w_x(t)] \sin [\beta_{C_1} - (\frac{dz}{dx})_{il}] \cos \lambda_{il} \end{aligned} \tag{14}$$

$$+ [-\omega X_{cil} + w_y(t)] \sin \lambda_{il}$$

$$+ w_z(t) \cos [\beta_{C_l} - (\frac{dz'}{dx'})_{il}]$$

To utilize strip theory set $\lambda_{il} = 0$ in equation (11). The wake induced velocities are determined by utilizing equation (2) and summing over the trailing and shed vortex segments. Recall the shed vortices are laid down between spanwise segments to satisfy the Kutta condition while the trailing segments are formed essentially by the motion of the surface.

3.7 The Deformed Wake

The wake at any instant of time consists of those shed and trailing vortex segments which have been laid down between time equal 0 and the instant under consideration. These segments are allowed to move and deform under the influence of the velocity field at their end points due to the bound and wake vortices. Equations (3) and (6) yield these velocities with local induction effects of equation (19) also included. Wake elements are tracked by tracking the end points. Each end point initially lies at the shed vortex (trailing edge) at a particular spanwise station, y_k, and hence has a coordinate in the propeller disc plane at its instant of shedding of

$$\underline{x}_{w_k}(t) = \underline{i}\, x_{T.E._k}(t) + \underline{j} y_k(t) + \underline{k}\, z_{T.E._k} \qquad (15)$$

The motion of this point is traced by allowing it to convect under the induced velocity field, $\underline{w}_i(\underline{x}_{w_k}, t)$

$$\underline{x}_{w_k}(t + \Delta t) = \underline{X}_{w_k}(t) + \underline{w}_i(\underline{X}_{w_k} t)\,\Delta t \tag{16}$$

and it is replaced by another end point at y_k. In this way the wake grows and deforms continually. It is entirely recalculated at each time step. Each "end point" is really the end point of four vortices, two trailing and two shed.

In the coordinate system fixed to the propeller disc plane

$$x_{T.E._k}(t) = x_{num_k} \cos\theta(t) - y_{num_k} \sin\theta(t)$$
$$y_{T.E._k}(t) = x_{num_k} \sin\theta(t) + y_{num_k} \cos\theta(t) \tag{17}$$

where θ is the azimuth angle between the blade and disc plane y axis and x_{num_1} and y_{num_1} are the coordinates in the blade fixed system. Then the coordinates of the deforming wake are computed by equation (16). When the blade moves to $\theta + \Delta\theta = \theta + \omega\Delta t$ the new end point is

$$x_{T.E._k}(t + \Delta t) = x_{num_k} \cos(\theta + \omega\Delta t) - y_{num_k} \sin(\theta + \omega\Delta t)$$
$$y_{T.E._k}(t + \Delta t) = x_{num_k} \sin(\theta + \omega\Delta t) + y_{num_k} \cos(\theta + \omega\Delta t) \tag{18}$$

Note z is unaffected by the coordinate transformation.

3.8 Self-Induced Velocity Field of the Vortex Wake:

The induced velocity, $\underline{w}_i(\underline{X}_w, t)$ of equations (16) is the velocity induced at the wake coordinate, $\underline{X}_w(t)$, at time, t, by all the vorticity in the lifting surface-wake system at time, t. This velocity field consists of that induced by the bound vorticity and that induced by the wake vorticity. The wake contribution consists of the effect of the vortex filament containing $\underline{X}_w(t)$ on itself as

well as the inductance of all the other filaments. These contributions are all determined by application of the Biot-Savart Law. In principle, no difficulties arise except when the contribution of the filament containing $\underline{X}_w(t)$ to the velocity at $\underline{X}_w(t)$ (i.e., the velocity induced by a vortex on itself) is considered; then a logarithmic singularity arises at $\underline{X}_w(t)$ which requires special handling. Efforts in treating this problem (46, 47, 48, 49) have led to considering the velocity induced by a filament on itself as consisting of two parts: (i) the far-field contribution due to all the filaments except that point at which the velocity is calculated, and (ii) the contribution of the region containing this point, the localized-induction contribution. Investigation of the (ii) contribution shows that the local contribution to the induced velocity is proportional to the local curvature and directed along the binormal to the filament.

The majority of analyses which try to account for the deformed wake consider all the contributions except (ii), the localized induction (exceptions are (21, 23, 28) which account for localized induction by a circular arc model). The more or less classical numerical approach with straight-line segments modelling the wake elements approximates the flow field due to the entire wake except those elements adjacent to the point, $\underline{X}_w(t)$, in question. This classical contribution is determined by repeated application of equation (1) or (3).

The localized-induction contribution to the induced velocity has been determined (49) to be

$$\underline{q}_i = \frac{\Gamma}{4\pi} \frac{(\partial \underline{r}/\partial s) \times (\partial^2 \underline{r}/\partial s^2)}{|\partial \underline{r}/\partial s|^3} \ell n(\frac{1}{\varepsilon}) \tag{19}$$

where $\underline{r}$ is the position vector of a point on the vortex filament, s; Γ is the circulation; and ε is an effective core radius. For a continuous filament $\partial \underline{r}/\partial s$ and $\partial^2 r/\partial s^2$ can be determined immediately. For the numerical problem with the vortex filament being approximated by a finite number of points it is possible to express the derivatives at a field point in terms of the locations of the field point and the ones adjacent on either side. Let $\underline{r}$ be the position vector of the vortex filament with $\underline{x}_1$, $\underline{x}_2$, $\underline{x}_3$ the location of three numerically determined adjacent position vectors of the filament in the positive direction of the filament, s. Then, using second order Taylor series expansions about $\underline{x}_2$ a forward difference gives

$$\underline{x}_3 = \underline{x}_2 + \frac{\partial \underline{r}(\underline{x}_2)}{\partial s} \Delta s_2 \frac{\partial^2 \underline{r}(\underline{x}_2)}{\partial s^2} \frac{\Delta s_2^2}{2}$$

while a backward difference gives

$$\underline{x}_1 = \underline{x}_2 - \frac{\partial \underline{r}(\underline{x}_2)}{\partial s} \Delta s_1 + \frac{\partial^2 \underline{r}(\underline{x}_2)}{\partial s^2} \frac{\Delta s_1^2}{2}$$

With $\Delta s_1 = |\underline{x}_2 - \underline{x}_1|$ and $\Delta s_2 = |\underline{x}_3 - \underline{x}_2|$ two equations in two unknowns yield the necessary derivatives at $\underline{x}_2$, $\partial \underline{r}(\underline{x}_2)/\partial s$ and $\partial^2 \underline{r}(\underline{x}_2)/\partial s^2$.

$$\frac{\partial^2 \underline{r}(\underline{x}_2)}{\partial s^2} = \frac{\underline{x}_3 - \underline{x}_2}{\Delta s_2 (\frac{\Delta s_1 + \Delta s_2}{2})} + \frac{\underline{x}_1 - \underline{x}_2}{\Delta s_1 (\frac{\Delta s_1 + \Delta s_2}{2})} \tag{20}$$

$$\frac{\partial \underline{r}(\underline{x}_2)}{\partial s} = \frac{\Delta s_1}{\Delta s_2}\frac{\underline{x}_3 - \underline{x}_2}{(\Delta s_2 + \Delta s_1)} - \frac{\Delta s_2}{\Delta s_1}\frac{(\underline{x}_1 - \underline{x}_2)}{(\Delta s_2 + \Delta s_1)} \tag{21}$$

Equations (20) and (21) can be written in Cartesian component form for computation as

$$\frac{\partial^2 \underline{r}(\underline{x}_2)}{\partial s^2} = \frac{1}{\left(\frac{\Delta s_1 + \Delta s_2}{2}\right)}\left[\underline{i}\frac{x_3 - x_2}{\Delta s_2} + \frac{x_1 - x_2}{\Delta s_2}\right.$$

$$\left. + \underline{j}\frac{y_3 - y_2}{\Delta s_1} + \frac{y_1 - y_2}{\Delta s_2} + \underline{k}\frac{z_3 - z_2}{\Delta s_2} + \frac{z_1 - z_1}{\Delta s_2}\right] \tag{22}$$

$$\frac{\partial \underline{r}(\underline{x}_2)}{\partial s} = \frac{1}{\Delta s_2 + \Delta s_1}\left[\underline{i}\frac{\Delta s_1}{\Delta s_2}(X_3 - X_2) - \frac{\Delta s_2}{\Delta s_1}(x_1 - x_2)\right.$$

$$\left. + \underline{j}\frac{\Delta s_1}{\Delta s_2}(y_3 - y_2) - \frac{\Delta s_2}{\Delta s_1}(y_1 - y_2) + \underline{k}\frac{\Delta s_1}{\Delta s_2}(z_3 - z_2) - \frac{\Delta s_2}{\Delta s_1}(z_1 - z_2)\right] \tag{23}$$

The total velocity induced at the wake point $\underline{x}_w$ (t) at time, t, is the sum of effects of the bound vortices, all filaments not containing $\underline{x}_w$ (t) and the filaments; one trailing and one shed, containing $\underline{x}_w$ (t) up to the adjacent points as determined by repeated application of equation (6); to this is added the effects of the four segments having $\underline{x}_w$ (t) as one end point and the four adjacent points as the other by equation (19). This velocity then determines the wake distortion by way of equation (16).

In principle, no difficulties arise in evaluating $\partial r/\partial s$ and

$\partial^2 \underline{r}/\partial s^2$ at any of the wake points except those on the edges of the wake sheet. The problem here lies in trying to determine the curvature of a filament at the point where it ends at the sheet's edge. Crimi (21) assumes the circular arc representation. It is assumed here that the curvature of the truncating filament is zero at the coordinate on which it ends so that the filament has no localized effect here.

Another problem concerned with the numerical evaluation of equation (19) is the determination of the proper Γ at $\underline{x}_2$. In the numerical analysis the straight line segments connecting the field points have constant circulations and change discontinuously across the field points, i.e., a step change in Γ occurs at $\underline{x}_2$. The local value at $\underline{x}_2$ can be taken as the average value, $(\Gamma_1(t) + \Gamma_2(t))/2$, where $\Gamma_1(t)$ is the circulation on $\Delta\underline{s}_1 = \underline{x}_2 - \underline{x}_1$ and $\Gamma_2(t)$ is the circulation on $\Delta\underline{s}_2 = \underline{x}_3 - \underline{x}_2$. Finally, since $\Gamma_1(t), \Gamma_2(t)$ obey the conservation of circulation as the wake deforms, it is convenient from the numerical standpoint to apply

$$\Gamma(t) = \frac{\Gamma(\tau)\Delta s(\tau)}{\Delta s(t)} \qquad t > \tau$$

so that

$$\Gamma(\underline{x}_2, t) = 1/2\left[\frac{\Gamma_1(\tau)\Delta s_1(\tau)}{\Delta s_1(t)} + \frac{\Gamma_2(\tau)\Delta s_2(\tau)}{\Delta s_2(t)}\right] \tag{24}$$

where $\Gamma(\tau)$, $\Delta s(\tau)$ are the circulation and length at the time of shedding, τ, respectively, and $\Delta s(t)$ is the length at the current time, t.

3.9 The Force on a Twisted Flat Plate Segment

Any given segment of the lifting surface is bound on three sides by straight-line vortex segments. It is known for unsteady flow that the pressure difference across a plate supporting a continuous distribution of circulation is given by the unsteady Bernoulli equation

$$\Delta p = \rho V \gamma + \rho \frac{\partial \Delta \phi}{\partial t} \tag{25}$$

where $\rho V \gamma$ is a quasi-static Kutta-Joukowski force and $\rho \partial \Delta \phi / \partial t$ reflects the unsteady character of the flow. $\Delta \phi$ is the potential jump across the plate. V is the velocity tangent to the plate and Δp is normal to it.

If, in the numerical model, only the velocity tangent to the plate is considered, a force directly equivalent to Δp in the unsteady Bernoulli equation is obtained. However, according to Betz (50) the net force produced by a bound vortex is due to its effective velocity. This effective velocity is that found at the midpoint of the vortex due to all other disturbances. Now the force that is determined includes the leading edge suction force associated with airfoil and wing theory. This is a direct result of using the effective velocity at the bound vortex midpoints and results in correct estimates of induced drag. Finally, it is also noted that the vorticity on a segment is the net chordwise vorticity along the segment chord, directed positive toward the leading edge at y and y + Δy, and the spanning vortex at the segment 1/4-chord. Figure (6) shows this geometry. Utilizing the effects of the bound vortices, the wake at any instant of time and free stream

and propeller rotation, the effective velocity at any vortex midpoint is known. Γ_1, Γ_2, Γ_3 on the segment are also known, Γ_2 being determined directly since it is a spanning vortex while Γ_3 and Γ_1 are combinations of chordwise sums and spanwise differences at y and y + Δy. Referring to Figure (6) the effective chordwise vorticity on a segment extends from the spanning filament on its segment to the spanning filament on the next chordwise segment.

Accordingly, the quasi-static force on a segment defined by the control point $\underline{x}_{cil}$ is found from the Kutta-Joukowski Law. On the panel defined by the control point $\underline{x}_{cil}$

$$\frac{F_{qs_{il}}}{\rho} = \underline{V}_{e_1} \times \underline{\Gamma}_1 \underline{l}_1 + \underline{V}_{ex_2} \underline{\Gamma}_2 \underline{l}_2 + \underline{V}_{ex_3} \underline{\Gamma}_3 \underline{l}_3 = \sum_{m=1}^{3} \underline{V}_{e_m} \times \underline{\Gamma}_m \underline{l}_m \qquad (26)$$

or, in component form

$$\frac{F_{x_{qs_{il}}}}{\rho} = [V_{ey_1} \Gamma_{z1} - V_{ez_1} \Gamma_{y1}] \, l_1 + [V_{ey_2} \Gamma_{z2} - V_{ez_2} \Gamma_{y2}] \, l_2 + [V_{ey_3} \Gamma_{z3} - V_{ez_3} \Gamma_{y3}] \, l_3$$

$$\frac{F_{y_{qs_{il}}}}{\rho} = [V_{ez_1} \Gamma_{x1} - V_{ex_1} \Gamma_{z1}] \, l_1 + [V_{ez_2} \Gamma_{x2} - V_{ex_2} \Gamma_{z2}] \, l_2 + [V_{ez_3} \Gamma_{x3} - V_{ex_3} \Gamma_{z3}] \, l_3 \qquad (27)$$

$$\frac{F_{z_{qs_{il}}}}{\rho} = [V_{ex_1}\ \Gamma_{y1} - V_{ey_1}\ \Gamma_{x1}]\ l_1 + [V_{ex_2}\ \Gamma_{y2} - V_{ey_2}\ \Gamma_{x2}]\ l_2$$

$$+[V_{ex_3}\ \Gamma_{y3} - V_{ey_3}\ \Gamma_{x3}]\ l_3$$

where x, y, z here refer to blade fixed coordinates.

Now:

$$\Gamma_{x1} = \frac{x_{jk} - x_{jk=1k}}{l_1}\ \Gamma_1 \qquad \Gamma_{x3} = \frac{x_{jk+1} - x_{j+1\ k+1}}{l_3}\ \Gamma_3$$

$$\Gamma_{y1} = 0 \qquad \Gamma_{y3} = 0$$

$$\Gamma_{z1} = \frac{z_{jk} - z_{j+1k}}{l_1}\ \Gamma_1 \qquad \Gamma_{z3} = \frac{z_{jk+1} - z_{j+1k+1}}{l_3}\ \Gamma_3$$

and

$$\Gamma_{x2} = \frac{x_{jk+1} - x_{jk}}{l_2}\ \Gamma_2 \qquad \Gamma_{y2} = \frac{y_{k+1} - y_k}{l_2}\ \Gamma_2$$

$$\Gamma_{z2} = \frac{z_{jk+1} - z_{jk}}{l_2}\ \Gamma_2$$

with the segments of the rectilinear vortex supplying the load to the panel containing the "il" control point given by

$$l_1 = [(x_{jk} - x_{jk+1})^2 + (z_{jk} - z_{jk+1})^2]^{1/2}$$

$$l_2 = [(x_{jk+1} - x_{jk})^2 + (y_{k+1} - y_k)^2 + (z_{jk+1} - z_{jk})^2]^{1/2}$$

$$l_3 = [(x_{jk+1} - x_{j+1\,k+1})^2 + (z_{jk+1} - z_{j+1\,k+1})^2]^{1/2}$$

Hence, the force components are given by

$$\frac{F_x}{\rho_{qs}} = [V_{ey_1}(z_{jk} - z_{j+1k})]\,\Gamma_1$$

$$+[V_{ey_2}(z_{jk+1} - z_{jk}) - V_{ez_2}(y_{k+1} - y_k)]\,\Gamma_2$$

$$+[V_{ey_3}(z_{jk+1} - t_{jk+1\,k+1})]\,\Gamma_3$$

$$\frac{F_y}{\rho_{qs}} = [V_{ez_1}(x_{jk} - x_{j+1k}) - V_{ex_1}(z_{jk} - z_{j+1k})]\,\Gamma_1$$

$$+ [V_{ez_2}(x_{jk+1} - x_{jk}) - V_{ex_2}(z_{jk+1} - z_{jk})]\,\Gamma_2 \qquad (28)$$

$$+ [V_{ez_3}(x_{jk+1} - x_{j+1k+1}) - V_{ex_3}(z_{jk+1} - z_{j+1\,k+1})]\,\Gamma_3$$

$$\frac{F_z}{\rho_{qs}} = [-V_{ey_1}(x_{jk} - x_{j+1k})]\,\Gamma_1 + [V_{ex_2}(y_{k+1} - y_k)$$

$$- V_{ey_2}(x_{jk+1} - x_{jk})]\,\Gamma_2 + [-V_{ey_3}(x_{jk+1} - x_{j+1\,k+1})]\,\Gamma_3$$

Note that F_x is essentially the induced drag and F_z the thrust on the panel. F_y is a spanwise force, due in part to the interaction of z-velocity with what is ultimately flow around the tip and in part to the fact that twist presents spanwise area to the flow.

The unsteady contribution is determined from the unsteady pressure term

$$\frac{F_{us}}{\rho} = \underline{n}\ (\text{Segment Area})\ \frac{\partial \Delta\phi}{\partial t} \tag{29}$$

Cutting the lifting surface at a spanwise station it can be shown, for a continuous distribution of vorticity that

$$\Delta\phi(x,t) = \int_{\text{L.E.}}^{x} \gamma(\zeta, t)\, d\zeta \qquad \zeta, \text{ x chordwise coordinates} \tag{30}$$

In numerical notation

$$\Delta\phi(x,t) = \sum_{\text{L.E.}}^{J} \Gamma_j\ (t)$$

where Γj's are the solution to the simultaneous equations. Since the disturbance is potential, $\Delta\phi$ is independent of the path of integration; hence, the integral of (30) should suffice to describe the unsteady pressure terms and

$$\begin{aligned} \frac{\partial}{\partial t}\ (\Delta\phi) &= \frac{\partial}{\partial t} \int_{\text{L.E.}}^{x} \gamma(\zeta,t)\, d\zeta \\ &= \frac{1}{\Delta t} \sum_{\text{L.E.}}^{J} [\Gamma_j\ (t + \Delta t) - \Gamma_j\ (t)] \end{aligned} \tag{31}$$

in numerical form.

Referring to Figure (6)

$$\underline{n} = \underline{i}\, n_x + \underline{j}\, n_y + \underline{k}\, n_z = \frac{\underline{l}_2 \times \underline{l}_3}{|\underline{l}_2 \times \underline{l}_3|}$$

$$\underline{n}\ (\text{Segment Area}) = \frac{\underline{l}_2 \times \underline{l}_3}{|\underline{l}_2 \times \underline{l}_3|}\ h\Delta X_c = \frac{\underline{l}_2 \times \underline{l}_3}{|\underline{l}_2| \sin\alpha\ |\underline{l}_3|}\ |\underline{l}_2|\ \sin\alpha\ \Delta X_c$$

$$\underline{n}\ (\text{Segment Area}) = \frac{\Delta X_c}{|\underline{l}_3|}\ \underline{l}_2 \times \underline{l}_3$$

where

$$|\underline{l}_3| = [(x_{jk+1} - x_{j+1\ k+1})^2 + (z_{jk+1} - z_{j+1\ k+1})^2]^{1/2}$$

Expanding the x-product yields the components of the unsteady force

$$\frac{F_{x_{us_{il}}}}{\rho} = \frac{\partial\Delta\phi}{\partial t}\frac{\Delta X_c}{|\underline{l}_3|}\ [(y_{jk+1} - y_{jk})\ (z_{jk+1} - z_{jk})]$$

$$\frac{F_{y_{us_{il}}}}{\rho} = \frac{\partial\Delta\phi}{\partial t}\frac{\Delta X_c}{|\underline{l}_3|}\ [z_{jk+1} - z_{jk})\ (x_{jk+1} - x_{j+1\ k+1}) \qquad (32)$$

$$- (x_{jk+1} - x_{jk})\ (z_{jk+1} - z_{j+1\ k+1})]$$

$$\frac{F_{z_{us_{il}}}}{\rho} = \frac{\partial\Delta\phi}{\partial t}\frac{\Delta X_c}{|\underline{l}_3|}\ [-(y_{jk+1} - y_{jk})\ (x_{jk+1} - x_{j+1\ k+1})]$$

so that the total force on the segment is

$$\frac{\underline{F}_{il}(t)}{\rho} = \frac{\underline{F}_{qs_{il}}(t)}{\rho} + \frac{\underline{F}_{us_{il}}(t)}{\rho} \tag{33}$$

Summing the forces chordwise gives the spanwise distribution and the total is obtained by summing spanwise

$$\frac{\underline{F}(t)}{\rho} = \sum_{l=1}^{\text{no. of span panels}} \sum_{i=1}^{\text{no. chord panels}} \frac{\underline{F}_{il}(t)}{\rho} \tag{34}$$

A more formal determination of the numerical approximation (equations (28) and (32)) to the components of the unsteady Bernoulli equation can be found in Appendix A. An unsteady induced power is also presented here.

The force of equation (34) is determined in a blade fixed coordinate system. Since the induced velocities are calculated in a propeller fixed system they must be transformed to the blade system. Considering the horseshoe vortex modelling the load on the panel defined by the "il" control point, the effective velocity on that segment lying along the chord nearest the left-hand (m=1) tip has components given by

$$\begin{aligned} V_{ex_1} &= \omega y_k + w_{ix} \cos\theta + w_{iy} \sin\theta \\ V_{ey_1} &= \omega\left(\frac{x_{jk} + x_{j+1k}}{2}\right) + w_{iy} \cos\theta - w_{ix} \sin\theta \\ V_{ez_1} &= w_{iz} \end{aligned} \tag{35a}$$

where $\underline{w}_i$ is the induced velocity determined in the propeller disc plane at the midpoint of the segment $(\underline{x}_{jk} + \underline{x}_{j+1k})/2$. θ is the instantaneous angular orientation of the blade-fixed system with respect to the propeller disc axis system. V_{ex_1}, V_{ey_1}, V_{ez_1}, are thus the effective velocity components in the blade fixed system. Similarly, on that vortex segment lying on the chord bounding the panel on the right-hand side (m = 3) the effective velocity components are

$$V_{ex_3} = \omega y_{k+1} + w_{ix} \cos\theta + w_{iy} \sin\theta$$

$$V_{ey_3} = \omega\left(\frac{x_{jk+1} + x_{j+1\,k+1}}{2}\right) + w_{iy} \cos\theta - w_{ix} \sin\theta \qquad (35b)$$

$$V_{ez_3} = w_{iz}$$

where $\underline{w}_i$ is determined at $(\underline{x}_{jk+1} + \underline{x}_{j+1\,k+1})/2$. On the spanning vortex across the panel (m = 2), the effective velocity components in the blade-fixed system are

$$V_{ex_2} = \omega\left(\frac{y_{k+1} + y_k}{2}\right) + w_{ix} \cos\theta + w_{iy} \sin\theta \qquad (35c)$$

$$V_{ey_2} = \omega\left(\frac{x_{jk+1} + x_{jk}}{2}\right) + w_{iy} \cos\theta + w_{ix} \sin\theta$$

$$V_{ez_2} = w_{iz}$$

where w_i is determined at $(\underline{x}_{jk+1} + \underline{x}_{jk})/2$ in the propeller disc plane.

3.10 Multi-Blade Effects

So far only one blade and its wake have been considered whereas propellers generally have B equi-spaced blades such that the separation angle is $2\pi/B$. For pure hover or static operation it can be assumed that all blade wakes and loading are identical, and the motions are identical. Hence, the effect of all blades and wakes on a reference blade can be calculated which then yields the propeller performance.

$$\frac{\underline{F}_{TOT}(t)}{\rho} = \frac{B\underline{F}(t)}{\rho} \qquad B = \text{No. of Blades} \tag{36}$$

Also, if x,y is a point in the propeller disc fixed system from the reference blade, the corresponding point from the n^{th} blade is given by

$$\begin{aligned} x_n &= x \cos \frac{2\pi(n-1)}{B} - y \sin \frac{2\pi(n-1)}{B} \\ y_n &= x \sin \frac{2\pi(n-1)}{B} + y \cos \frac{2\pi(n-1)}{B} \end{aligned} \tag{37}$$

The same relation will put a point on the n^{th} blade into the coordinate system fixed to the reference blade.

3.11 Computational Procedure

The resulting computational procedure for calculating the

loading on the lifting surface Wagner problem applied to the propeller is presented in the following five steps.

(1) Input blade planform characteristics (chord, camber and twist distribution), external velocity, number of blades, RPM.

(2) Determine influence coefficients for unknown bound vortices (including vortex which is shed at the trailing edge at the end of each time step) at a prescribed number of control points (equation 5).

(3) Satisfy the boundary condition, $\underline{V} \cdot \underline{n} = 0$ at all control points simultaneously,

$$A_{pq}\Gamma_q(t) = -V_{n_p}(t) \qquad \begin{matrix} P = 1,\ldots, \text{no. of control points} \\ q = 1,\ldots, \text{no. of vortices} \end{matrix} \tag{38}$$

Where A_{pq} is the velocity component normal to the surface at the p^{th} control point due to the q^{th} unit strength vortex, Γ_q is the strength of the q^{th} unknown vortex and V_{np} is the total normal velocity at the p^{th} control point due to external sources. For a propeller or rotor this could include flight speed, rotational speed, blade flapping and aeroelastic motions, and wake induced velocities. For the rigid statically thrusting propeller only rotational speed and wake induced velocities are considered.

In general the number of unknown vortices exceeds the number of control points by the number of spanwise panels into which the surface is divided because the vortices to be shed at

the end of a particular time step are considered unknown. We make up this deficit in the simultaneous equations by applying the Kutta condition (51)

$$\sum_{j=1}^{num} \Gamma_j(t) = \sum_{j=1}^{num-1} \Gamma_j(t-\Delta t) \tag{39}$$

which corresponds to conservation of circulation on any "1" spanwise station. "num" represents the number of unknown vortices on a spanwise segment; "num-1" are bound and "num" is that which is shed at the end of a time step. The two conditions can be considered one set of N x N simultaneous equations of the form

$$E_{pq}\Gamma_q = G_p \tag{40}$$

where

$$E_{pq} = \begin{cases} A_{pq} & p = 1,\ldots, \text{no. of control points} \\ & q = 1,\ldots, \text{no. of unknown vortices} \\ 1\ 1\ldots1\ 0\ldots0\ 0\ldots0 & p = \text{no. of control points},\ldots, \text{no. of unknown vortices} \\ 0\ 0\ldots0\ 1\ldots1\ 0\ldots0 & q = 1,\ldots, \text{no. of unknown vortices} \\ 0\ 0\ldots\ldots\ldots1\ldots1 & \end{cases} \tag{41}$$

i.e., the coefficients in any row take on the value of 1 with the vortices on the particular spanwise segment on which the Kutta condition is applied; the remainder are 0.

$$G_p(t) = \begin{cases} -V_{np}(t) & p = 1, \text{ no. of control points} \\ \sum_{j=1}^{num-1} \Gamma_j(t-\Delta t) & p = \text{no. of control points, no. of vortices} \end{cases} \quad (42)$$

The equations are solved numerically by standard matrix inversion and multiplication techniques for the unknown Γ_q's

$$\Gamma_q(t) = E_{pq}^{-1} G_p(t) \quad (43)$$

(4) With Γ_q's known the unsteady loading is determined.

(5) The wake deformation and motion is then obtained by determining the velocities induced in the wake by itself and the bound vorticity and advancing the lifting surface at the rate, $\underline{V}_\infty$. A new wake is then determined by evaluating new wake coordinates.

$$\underline{X}(t + \Delta t) = \underline{X}(t) + \underline{V}(t)\Delta t \quad (44)$$

where $\underline{V} = \underline{V}_\infty + \underline{w}_i$ and $\underline{w}_i$ the total induced velocity at a wake point. $\underline{V}_\infty = 0$ for hover. With the new wake coordinates, the velocity induced at the control points on the surface is determined and $\sum_{j=1}^{num-1} \Gamma_j(t)$ obtained for each spanwise station so that $G_p(t + \Delta t)$ is known at $t + \Delta t$. Hence, $\Gamma_j(t + \Delta t)$ is determined and the process is repeated for a desired number of time steps.

3.12 Real Fluid Effects

Equation (33) yields a force distribution based on potential flow theory. In order to estimate the true performance characteristics, real fluid effects must be included as best as is possible. Realistic lift curve slopes and drag coefficients must be estimated for

the propeller sections, with Reynolds' number and Mach number effects also included. While two-dimensional data below the stall has been well tabulated (52), data, particularly drag data, at the stall and beyond is sparse. Since the propeller at the higher twists can have a large portion of the inboard sections stalled this can lead to difficulties in accurately predicting the power and thrust. Further, recent measurements of the pressure distribution on a propeller blade (9) indicate enough three-dimensionality, at least in the tip region, to make the application of two-dimensional data questionable. Unfortunately there is nothing better so this must be considered.

To apply the real section characteristics to propeller performance, the radial distribution of angle of attack must be determined. With the steady state radial distribution of x-force and z-force (F_{x1} and F_{z1}) determined by the equation (33) all the force is Kutta-Joukowski force; hence $F_{x1}^2 + F_{z1}^2$ is normal to the effective velocity. Then, referring to Figure (7), the effective angle of attack at the 1 section is

$$\alpha_{o1} = \beta_1 - \tan^{-1} \frac{F_{x1}}{F_{z1}} \qquad (45)$$

where β_1 is the pitch of the 1^{th} section. Assuming the section characteristics are known,

$$C_{l_1} = a_{o_1} \alpha_{o_1}$$

$$C_{d_1} = C_{d_1}(R_{e_1}, M, C_{l_1}) \tag{46}$$

This yields the section thrust and power on a spanwise segment, Δy_1,

$$\Delta T = \tfrac{1}{2} \rho V_{e_1}^2 C_{c_1} (C_{l_1} \cos \phi_1 - C_{d_1} \sin \phi_1) \Delta y_1$$

$$\Delta P = \tfrac{1}{2} \rho V_e^2 C_{c_1} (C_{l_1} \sin \phi_1 + C_{d_1} \cos \phi_1) \omega y_{c_1} \Delta y_1 \tag{47}$$

For a B-bladed propeller, the total thrust and power are

$$T = \frac{B}{2} \rho \sum_{r_h}^{R} V_{e_1}^2 C_{c_1} (C_{l_1} \cos \phi_1 - C_{d_1} \sin \phi_1) \Delta y_1$$

$$P = \frac{B}{2} \rho \sum_{r_h}^{R} V_{e_1}^2 C_{c_1} (C_{l_1} \sin \phi_1 + C_{d_1} \cos \phi_1) \omega y_{c_1} \Delta y_1 \tag{48}$$

Thus, with

$$C_T = \frac{T}{\rho \pi R^2 V_T^2} \tag{49}$$

$$C_P = \frac{P}{\rho \pi R^2 V_T^3}$$

$$C_T = \sum_{x_h}^{1.00} \frac{V_{e_1}^2}{V_T^2} \sigma_1 (C_{l_1} \cos \phi_1 - C_{d_1} \sin \phi_1) \frac{\Delta y_1}{R} \tag{50}$$

$$C_P = \sum_{x_h}^{1.00} \frac{V_{e_1}^2}{V_T^2} \sigma_1 \frac{yc_1}{R} (C_{l_1} \sin \phi_1 + C_{d_1} \cos \phi_1) \frac{\Delta y_1}{R}$$

Finally, since $F_{x_1}^2 + F_{z_1}^2$ is normal to V_{e_1}, its reaction in the fluid, the induced velocity at the blade is also normal to V_{e_1}. Then, again referring to Figure (7),

$$V_{e_1} = \omega y_{c_1} \cos \phi_1$$

then (51)

$$\frac{V_{e_1}}{V_T} = \frac{yc_1}{R} \cos \phi_1$$

so that

$$C_T = \sum_{X_h}^{1.00} \frac{y_{el}^2}{R^2} \cos^2 \phi_1 \sigma_1 (C_{l_1} \cos \phi_e - C_{d_1} \sin \phi_1) \frac{\Delta y_{c_1}}{R} \quad (52)$$

$$C_P = \sum_{X_h}^{1.00} \frac{y_c^3}{R^3} \cos^2 \phi_1 \sigma_1 (C_{l_1} \sin \phi_1 + C_{d_1} \cos \phi_1) \frac{\Delta y_{c_1}}{R}$$

where $\cos \phi_1$, $\sin \phi_1$ can be determined from

$$\cos \phi_1 = \frac{F_{z_1}}{F_{z_1}^2 + F_{x_1}^2} \quad (53)$$

$$\sin \phi_1 = \frac{F_{x_1}}{F_{z_1}^2 + F_{x_1}^2}$$

Note that no effects due to radial flow are considered here except those which arise in the determination of F_{x_1}, F_{z_1} from the numerical lifting surface theory.

Chapter IV

RESULTS AND DISCUSSION

4.1 Capabilities of the Analysis

The foregoing analysis leads to a digital program capable of treating the following lifting systems and their wakes:

(i) an infinite or finite wing moving unsteadily and generating either a linearized (flat) wake or a free, self-convecting (deformed) wake.

(ii) a multi-bladed propeller in static thrust. It is unsteady since the propeller usually starts from rest and the wake is deformed. It is restricted to the static thrust problem since wake symmetry between blades is assumed.

4.2 Comparison of Two Computation Systems

It is well-known that numerical lifting surface analyses based on vortex lattice techniques require large amounts of computer time and storage. As a result, even though initial programming was done on an IBM 360/67 computer at the Pennsylvania State University, it became obvious this machine was inadequate for the complete propeller solution. Maximum time available and core storage are both insufficient and for these reasons, the CDC 6000 series machines, with larger usable core, at NASA-Langley Field, Virginia, were considered. The analysis was re-programmed for this installation and, as will be shown subsequently, time requirements were measurably reduced.

As an added bonus much greater numerical accuracy was noted. Compile times on the CDC units are also considerably faster than on the 360/67.

A short study of the time requirements on the Penn State IBM 360/67 computer was made utilizing a model of the rectangular wing with 19 panels spanwise (20 trailing vortices). The wing was set at .1 rad. angle of attack, started impulsively from rest and allowed to generate its own wake. Run times up to 2000 sec., the maximum allowable, were considered. It was found that

$$\text{Computation Time (sec.)} = .937 \left(\frac{\text{wing travel distance}}{\text{chord}} \times 10\right)^{2.59}$$

not including compile time. While this case was not run on the CDC 6000 machines, the results for one wing geometry (three spanwise panels at .1 rad. angle of attack) were compared and shown in Figure (8). It can be seen the rate of increase of computation time is greater on the 360/67 than on the 6000 series. It was also found that the compile times are on the order of six times faster on the CDC machines.

Accuracy of the CDC machines are greater with the single-precision mode roughly equivalent to the 360/67 double precision mode and double precision arithmetic was necessary on the 360/67 to obtain acceptable results. Single-precision arithmetic on the CDC machines was quite adequate and this in turn results in a computation time saving.

4.3 Vortex Kinematics

Some time was spent in observing the velocity field induced by a

straight line vortex segment in hopes that some a priori assumptions regarding the wake and the number of elements needed to describe it could be made. Figure (9) shows the variation of induced velocity at a point located a fixed h/l from the vortex segment, but at different lateral locations; this effectively describes the variation a point would see as it translates in a plane past the filament. Figure (10) shows the variation this point would see as it moves on a circular path, in the plane, about the filament. As expected, regular variations occur from maximal when the point is at mid-segment to minima (zero) when the point is aligned with the segment. While these computations were done for a distance from segment mid-point to segment length ratio of 2, the trends will be the same for any other value, being higher or lower as the ratio is smaller or greater, respectively, and passing through 0 at δ or β equal 0.

Figure (11) illustrates an attempt to correlate the velocity at a point in the plane due to an angularly oriented filament with the projected length normal to the line from the point. It can be seen that the greatest difference for any angular orientation occurs at approximately $h/l \cong .2$. This vanishes rapidly until, at $h/l \cong 5$, the effect of the orientation vanishes.

Figure (12) shows the variation of induced velocity as a function of normal distance from the line segment. This figure is interesting because it shows the transition of the

induced velocity from an essentially two-dimensional flow near the segment ($v \sim 1/r$ for $h/l \lesssim .1$) to a fully three-dimensional field farther away ($v \sim 1/r^2$ for $h/l \gtrsim 1$).

While the foregoing figures describe to some extent the character of the elementary velocity field and the region of influence of an elementary piece, no particular convenient approximations applicable to the self-generating wake could be discerned. First, the results apply to the magnitude of the velocity field and so even if an approximation could be found to this, one is still faced with calculating the orientation relative to the specified coordinate system. This is the difficult part of numerically integrating the Biot-Savart Law. Hence the problem of streamlining the wake calculations reduces to the question of whether or not the wake can be numerically truncated. Since a major part of the static propellor problem concerns the interference of the vortex wake from one blade with another blade, it seems that no elements can be dropped, at least until the wake is well formed.

4.4 Results of the Unsteady Lifting Surface Theory

The following results have been accumulated as the program developed from the case of a finite wing with a linearized (flat) wake to that final one which treats the propeller starting impulsively in static thrust. Since concern is directed toward the propeller starting impulsively, most of the results utilize this mode of initiating motion; this is the classical Wagner problem. However, prior to investigating the propeller, considerable time was spent with the finite wing since this configuration contains essentially the same numerical problems as the propeller but is less complex. The wakes considered here are the classical types, either flat or deforming, without the localized induction results of Section (3.8). The infinite wing case is treated by simply considering a sufficiently high aspect ratio wing.

4.5 Infinite Wing

The infinite wing was modelled by considering a single spanwise panel, AR = 1000, at an angle of attack of 0.1 rad. The non-dimensional time step is $V\Delta t/C = 0.1$. Giving the wing an impulsive start describes a good approximation to the classical two-dimensional Wagner problem. These are compared in Figure (13) which shows the lift building up from rest to steady state with the distance the wing travels per unit chord. The comparison is good except in the initial instants where large deviations occur. The Wagner solution contains only the effect of the wake whereas the numerical solution

contains an "infinite" added mass lift solution with the impulsive start, or infinite frequency with the step change in angle of attack, which dies out rapidly.

To get some feel for aspect ratio effects, the results for AR = 0.1 are also shown. The lift drops rapidly from the high added mass condition to a steady state value somewhat less than the two-dimensional value. Here the trailing vortices are very effective in satisfying the boundary condition so that the bound circulation does not need to contribute as much as in the two-dimensional case.

Figure (14) shows the rapid change in the shape of the chordwise loading in going from predominantly added mass lift to the final predominantly steady state distribution for the AR = 1000 wing. The shape of the final distribution is evident after only .2 sec. time of motion or .2c distance of travel by the wing. It should be noted that in these calculations that the wake is a flat, classical wake. The chordwise pressure distribution was approximated by eight bound vortices; however, as will be seen subsequently, C_l is quite insensitive to the number selected.

A two-dimensional model was started from rest in a simple harmonic motion (Theodorsen) at a reduced frequency of 0.2. The fluctuating lift exhibited the "infinite" added mass characteristic at the instant of start but subsided into the classic form well within the first cycle of motion. It can be noted that convergence to the classic results of both the Wagner and Theodorsen problems was slightly better than the results of Reference (53).

4.6 Finite Wing

The finite wing investigated consists of an AR = 3 untwisted rectangular wing at $\alpha = 0.1$ rad. starting impulsively. This aspect ratio was selected as one sufficiently in the middle range so that neither lifting line nor slender wing approximations would enter the calculations. The numerical results for C_L, the wing lift coefficient, are compared to an approximation to DeYoung's (16) results for steady motion.

$$C_L = \frac{2\pi AR\alpha}{AR + 2\left(\frac{AR + 4}{AR + 2}\right)} \tag{47}$$

The AR is small enough that the loading is nearly elliptic so that the induced drag is given by

$$C_{D_1} = \frac{C_L^2}{\pi AR} \tag{48}$$

for steady motion.

The effect of the number of spanwise panels on the wing lift coefficient is shown in Figures (15) (AR = 3) and (16) (AR = 1.5). In both cases convergence to the DeYoung value requires a relatively large number of panels. Intermediate calculations indicate a noticeable loss of accuracy in C_L as less than 10 panels are considered. The C_L's are shown as functions of the length of the trailing vortices with a linearized wake. For AR = 3, a wake approximately 5 chords long is sufficient to guarantee convergence to the proper C_L. For AR = 1.5 the wake length required is less,

about 3 chords. This is due to the trailing vortices being more effective sooner in satisfying the boundary condition as the AR decreases as previously implied in Figure (13). It can be noted, however, that convergence is relatively insensitive to the number of spanwise panels modelling the wing. Five chord lengths for the AR = 3 wing suffices for 3 panels or 19 panels. Further, these wake lengths represent maxima in that no shed vorticity is present. These comparisons are based on steady state models and, if an unsteady Wagner motion and the shed vortices were present, convergence would occur faster.

Finally it must be noted that AR's are based on the spanwise distance between the tip vortices with no regard for Rubbert's rules (34) for handling the tips. If Rubbert's criteria are followed slightly better correlation between numerical C_L's and those given by equation (47) for the coarser spanwise spacing will be observed since the AR is measurably larger. Convergence to the proper C_L could then be expected to be more rapid. The present results are perhaps more properly interpreted as indicating the minimum spanwise spacing necessary so that Rubbert's rules for handling the tips can be neglected. For a given AR, then, these results should be more than sufficient to guarantee convergence to the proper C_L.

The effect of the chordwise distribution of bound vorticity on the wing lift and induced drag is shown in Figure (17). The Wagner problem is considered here with the wing given an impulsive start and laying down a linearized wake. Shed vorticity is present

and convergence to the steady state values occur in about 1.5 chords of travel. Twenty spanwise panels model the loading distribution. The initial "infinite" added mass force associated with the impulsive start is seen to quickly subside as the wing approaches the steady state condition. The cases considered compare chordwise loading approximated by 1 and 4 bound vortices and it is easily seen that both C_L and C_{Di} are insensitive to the number selected after the steady state is reached. For both quantities the tendency is to drop under the steady state value, then approach asymptotically from the low side. Figure 18 shows the effect of number of spanwise panels on induced drag. For the configurations shown the 3 panel vortex lattice over-predicts the 20 panel model by approximately 9%.

An attempt to show the effects of removing the linearizing effects on both the boundary condition and the wake (allowing it to deform) is given in Figure (19). Linearizing the boundary condition implies an inflow to a wing control point to be given by $V\alpha - w_{zil}$ instead of $V \sin \alpha - w_{zil} \cos \alpha + w_{xil} \sin \alpha$. For $\alpha = 0.1$ rad. the differences are negligible on the plot but consistent results could be seen in the computer output. Linearizing the boundary condition while allowing the wake to deform results in higher C_L's; then if the wake is linearized, the C_L's increase more. The greatest differences appear to be in whether or not the boundary condition is linearized and becomes more apparent at greater time. Apparently, at the instant of start when wake elements are strongest

and their effects would be greatest, they are very near the plane of the wing and so approximate the linearized wake; also strong added mass effects near the start will tend to overshadow the wake effects. Then as time progresses the strong shed vortices are carried away (their influence going like $1/r^2$) and the trailing vortices which now have nearly constant strength tend to be most effective. Taking the wing to be most sensitive to this near wake and noting the displacement of this portion from the plane of the wing to be small, the differences between the linearized and deformed wakes are small. Greater differences exist when considering the linearized vs. non-linearized boundary condition for this alters the impact velocity on the wing. In general this will decrease as V sin α instead of Vα; hence, less circulation is needed to satisfy the boundary condition so a smaller C_L results.

Examples of the deformed wake for crude models (2 chordwise panels, 4 trailing vortices) are shown in Figures (20) (α = 0.1 rad.) and (21) (α = 1.0 rad.). It is seen that the wake is convected downward behind the wing except for the first shed vortex which remains in the plane of the wing. The inboard filaments are convected downward more than the outboard, a fact in qualitative agreement with physical observation and numerical results (43). As time progresses more shed vorticity is collected in the vicinity of the one shed initially to form the fluid starting vortex. This vortex remains more or less in the plane of the wing, but slightly underneath it. There is little tendency for the vortices to roll up into the tip vortices. This is due probably in part to the

crudeness of the model in spanwise spacing, but also in part to the neglect of the localized-induction effects of (3.8). The case of $\alpha = 0.1$ rad. produces smooth, continuous results using just the integration technique of equation (44). The $\alpha = 1.0$ rad. case, however, exhibits an apparent oscillation in the tip filament. This oscillation is really a spiral motion of this filament due to the error involved in applying equation (44) directly. The trajectory needs to be determined by a more sophisticated integration scheme such as predictor-corrector (modified Euler).

The growth in C_L and C_{D_i} with time for $\alpha = 1.0$ rad. angle of attack is shown in Figure (22). Small amplitude oscillations, a direct result of the spiral trajectory of the strong tip vortices, is noted. The asymptotic C_L appears to be ≈ 3.0, something less than 10 times the $\alpha = 0.1$ rad. case (Figure 18). In fact, it is only slightly less than the value obtained if C_L varies as $\sin \alpha$ rather than α, a direct effect of a nonlinearized boundary condition. One should take care in interpreting the results entirely in this light, however, since wake deflection and the ensuing tilt-back of the Kutta-Joukowski force vector (16) will also result in a decreased C_L.

Finally, even at the high C_L, little interaction between trailing vortices was observed so that no strong tendency for the wake to roll-up could be seen. A model at $\alpha = 0.1$ rad., but with 20 spanwise panels to model the loading, was run and still no strong roll-up tendency could be seen. Although not so long a wake could be generated with this larger number of spanwise panels due

to computer limits, qualitative agreement among the three cases exists. However, roll-up rates as determined by these classical approaches appear to be much too slow. This leads to the belief that a further mechanism, notably the localized-induction effects of (3.8) must be considered.

4.7 Localized Induction Effects on the Vortex Wake Roll-up

Previous Attempts (39, 40, 41) to model vortex wake roll up have generally considered a Trefftz plane analysis and treated the wake distortion as an unsteady motion proceeding from an initially flat wake geometry. While the final geometries are generally realistic all show roll-up rates which are much too slow. Jordan (44) takes exception to the numerical procedures and develops a lifting surface theory which contains a logarithmic singularity in the downwash at the trailing edge slightly inboard of the tips. He claims this singularity will drive the wake roll-up at a much faster rate but unfortunately he can provide no physical insight into the existence of this singularity.

In an attempt to better model the vortex roll up rate consideration was given to the localized-induction concept presented in (46, 47, 48, 49). This approach was taken based on the physical observation of flow field development at the start of the motion, what is necessary to generate wake roll up, and the manner in which the localized induction concept can describe this requirement.

At the initial instant of start a shear layer leaves the trailing edge and rolls up into a well defined starting vortex with

circulation equal and opposite to that around the wing. In the case of a two dimensional flow this vortex is simply swept away by the free stream (for example, Ref. 54, Fig. 22). Similarly, at the instant of start of a finite wing the motion is nearly two-dimensional with the starting vortex forming essentially parallel to the trailing edge. The shear layer feeding this vortex from the trailing edge is highly curved, streamwise, as it is drawn into the starting vortex.

In order to promote wake roll-up the two dimensionality of the flow must be disturbed; a strong spanwise flow tending to convect the wake laterally provides this. The shear layer which feeds the starting vortex contains the shed and trailing vortex filament which model the wake. Hence, soon after the motion starts, the curved shear layer is reflected in the streamwise curvature of the trailing vortex filaments. According to the localized induction comcept described in (49) a curved vortex filament induces at a point on itself a velocity proportional to the local curvature and directed along the local binormal. This means that the curvature of the trailing vorticity can induce a spanwise flow which will tend to destroy the initial two dimensional character of the motion. Under this influence the vortex segment endpoints describing the wake will travel spiral paths which should promote interference between filaments and increase the roll up rate.

In order to assess the relative importance of considering the localized induction concept wake roll-up a short numerical study was performed. An aspect ratio 3 wing at 0.1 radian angle of attack was started impulsively from rest. The chordwise loading

was modeled by two bound vortices and the spanwise loading by four vortices. It traveled 0.1 chord lengths in each time step. Figures (23) and (24) show the Z-component (downwash) and y-component (spanwise) of induced velocity, respectively after 1.2 chord lengths of wing travel for the case of no localized induction. The downwash varies spanwise but is fairly uniform streamwise until the end of the wake is reached. This induced velocity is on the order of 0.03 ft./sec. to 0.08 ft./sec. The spanwise velocity, while appearing more erratic than the downwash, is generally smaller than the downwash by a factor of 10. The exception is in the vicinity of the end of the wake where it increases or exceeds the order of the downwash; this is due to the vortices shed initially beginning to distort. However, over the majority of this wake the fact that the downwash is greater than the spanwise velocity by an order of magnitude indicates the flow in transverse planes of the wake will be essentially two-dimensional.

The wing was rerun for the same conditions but with the wake allowed to convect under the localized induction process. Figures (25) and (26) show the induced velocity field in the wake after 1.2 chord lengths of travel. It can be seen that the downwash and spanwise components are both of the same order of magnitude, approximately 0.1 ft./sec., with the y-component peaking at over 0.8 ft./sec. The shapes of the curves indicate the trailing vortices are performing a spiral motion, and while the model is too coarse to permit interaction between the trailing vortices, the flow field is highly three-dimensional.

Another indication of the potential that the streamwise curvature has for inducing a spanwise flow can be estimated from Figure (22), Reference (53). The two-dimensional starting vortex shown in Reference (53), Figure (22), can be reasonably approximated by two turns of an hyperbolic spiral with an asymptotic displacement to chord ratio of approximately 1/3. The velocity induced by this spiral filament on itself by equation (19) is shown in Figure (27). The self induced velocity is normal to the plane of the spiral and increases as the center is approached. Utilizing circulation values from the AR = 3 wing at 0.1 radian with 2 chordwise vortices and 4 trailing vortices, a velocity on the order of 10 ft./sec. could be obtained. This means that, at the instant of formation shown in Reference (52), if the two-dimensional constraint could be removed a velocity parallel to the trailing edge on the order of 10 ft./sec. would exist. Such a velocity should be of sufficient magnitude to destroy the two-dimensional character of the flow typified by the 0.05 ft./sec. spanwise velocities of Figure (24).

As a final comparison an AR = 3 wing at 0.1 radian angle of attack with 2 chordwise vortices and 21 spanwise vortices to model the loading was run with and without the localized induction effect of equation (19). Figures (28) and (29) represent the classic wake with no localized induction while Figures (30) and (31) include the effect. Comparing the wake structure with and without this effect it can be seen that nearly 6 times the distance of wake is included to promote wake roll-up

without the effect of equation (19) as with it. The classic wake shows little interaction until it is about 3 chord lengths long and the distortions are quite gradual. At this point only two trailers are measurably affected. On the other hand, with localized induction, the tip vortex has broken down into a spiral motion after only about 0.5 chords of travel, is interacting strongly with the second and is beginning to affect the third. A further important observation is that once the vortices enter the spiral motion they apparently never recover and the wake roll-up is governed entirely by the localized induction process.

While the preceding results are quite limited they do give some indication into the requirements of wake roll-up modeling. Basically it can be concluded that in order to predict the proper wake roll-up, both as to shape and rate, the motion at the instant of start must be considered. The high curvatures of the trailing vorticity are required to induce the spanwise flow and destroy the initial two-dimensional character of the motion. Apparently it is precisely this two-dimensional nature of Trefftz plane motion that precludes the usual analyses from predicting the proper roll-up rate, also, apparently classical aerodynamic theory is quite capable of predicting proper wake roll-up characteristics provided the problem is properly posed, and recourse to new theory as has been suggested (44) is not required.

4.8 Effect of Core Radius

The Biot-Savart Law (equation (1)) contains a singularity if

the point at which the induced velocity is determined lies on the filament. In order to circumvent this difficulty it has been standard practice to define a core radius inside of which the potential flow field induced velocity does not exist. Either no velocity or a simple solid body rotation is assumed. A variety of methods for defining this radius (see Appendix B) exist with no particularly strong argument for any.

Comparison of Figures (28) and (29) show the effect of varying the core radius on the formation of the classic wake while Figures (30) and (31) show the same comparison for the wake with localized induction. Figures (28) and (30) illustrate a core radius which is proportional to the length of the filament while Figures (29) and (31) show the results for a fixed core radius of 10^{-6} ft. The proportional core varies slightly but generally has a radius of the order of 10^{-4} ft. In any case, no discernible effect on the wake formation due to changing the core radius can be observed.

Figure (32) shows the wake behind the wing with a core radius of 10^{-10} ft., including the localized induction effect. Comparing with the 10^{-6} ft. core, the disturbances at 1.5 chords of travel are noticably stronger for the former. At 1.0 chord of travel, interaction between the two outboard filaments is much more prominent with the third also being affected. At around 2 chord lengths of wing travel the first three outboard filaments are interacting with the fourth beginning to distort spanwise for the 10^{-10} ft. core. By the time the wing has moved through 2.9 chords, relatively strong interaction for the 10^{-10} ft. core is observed,

among the far outboard filaments. Obviously, then the core radius can be an important consideration if it is allowed to be small enough. It is important to notice these results are due primarily to the effect of core radius in the localized induction contribution (equation (19)) and not in the mutual interaction between filaments that has a maximum velocity defined by a minimum cut-off distance in equation (1).

Figure (33) compares the C_L and C_{Di} distributions for the classic wake and the localized-induction wake for the proportional core while Figure (34) makes the same comparison for the fixed core, 10^{-6} ft. In both cases the classic wake C_L's and C_{Di}'s do not vary significantly from the ideal flat (linearized) wake case. Small but measurable increases in the force coefficients for the localized induction wake over the classic wake exist due to small streamwise velocities induced by the spiral motion of the filaments.

One inconsistency in the wake analysis with localized induction has been permitted. The term, ε, in equation (19) is a core radius non-dimensionalized on the length of vortex segment which is used to determine the localized induction effect whereas in equation (1) the core radius is a minimum value of h, say h_c, used to cut off the velocity at a maximum and is a dimensional quantity. In the analysis both these core radii have been given the same value which is not necessarily correct since, conceptually, there is no reason they should be the same. In view of the fact that the logarithmic function in equation (19) is very slowly

varying the error involved in the velocity field of the wake is small. This is apparently borne out by the fact that discernible differences in the wakes were observed only when the core radii differed by several orders of magnitude.

The preceeding observations would imply the generated wakes are relatively insensitive to the selection of core radius, at least insofar as physically reasonable geometries are concerned. However it must be recognized that two core radii to be determined by different criteria can exist. The core radius, ϵ, of equation (19) should be selected to give reasonable locally induced velocities, while the core radius, h_c, of equation (1) will govern the velocities encountered in vortex interaction problems and will be determined by limits on the velocities and/or displacements due to this phenomenon. As will be seen subsequently, this core radius associated with interaction can be critical since it can ultimately affect the stability of the wake generation.

4.9 The Statically Thrusting Propeller

With the analysis established and verified for the finite wing under an impulsive start, the case of a statically thrusting propeller was run. The lack of a suitable test facility precluded any test procedure for experimental verification so recourse was made to the literature. The propeller selected is fully described in Reference (9), but briefly can be said to be a 4-bladed configuration with a radius of 3 ft., β at 0.75 radius of 7.3° and run at a tip speed of 600 ft./sec. This propeller was selected on the

basis of having blade load and power radial distributions as well as average thrust and power values available.

The computed performance is summarized in Figures (35) through (42). The numerical configuration consisted of 16 spanwise panels to model the radial load distribution and 2 chordwise panels to model the chordwise distribution. A vortex core radius of 10^{-6} ft. was chosen initially and this configuration was run for 20000 sec. on a digital computer for each of three azimuth increments (time steps), $\Delta\theta = 15^{\circ}$, $\Delta\theta = 7^{\circ}$ and $\Delta\theta = 3^{\circ}$. The propeller moved through 615°, 287°, and 122° respectively. In order to assess the effect of selected core radii on the wake the $\Delta\theta = 15^{\circ}$ case was re-run with a core radius of 10^{-10} ft.

The performance is determined by two methods. One is the direct numerical integration of the segment forces and powers as given by equations (33) or (A 13) and (A 14), respectively. In order to convert these to coefficient form, the integrated results are non-dimensionalized by $\rho V_T{}^2 \pi R^2$ on the thrust and $\rho V_T{}^3 \pi R^2$ on the power. The second method takes the z- and x-components of the spanwise load distribution as determined by integrating equation (33) or (A 13) chordwise to determine an inflow angle $\tan^{-1} F_{x1}/F_{z1}$. The section angle of attack is known from equation (45). This, in turn, permits the use of real airfoil data and equations (48) or (50) can be used to determine thrust and power including real fluid effects. The results are strictly valid, however, only in the limit as the steady flow state is reached. Finally, it should be noted that to draw a direct comparison with the results of

Reference (9), the C_T and C_P values must be multiplied by $\pi^3/4$ and $\pi^4/4$, respectively, since Reference (9) uses standard propeller convention ($C_T = T/\rho\ (\omega/2\pi)^2\ (2R)^4$ and $C_P = P/\rho\ (\omega/2\pi)^3\ (2R)^5$).

The thrust performance for the three configurations with varying $\Delta\ \theta$ is given in Figure (35) through (37). In all cases the propeller responds much like a small aspect ratio finite wing up until blade-wake interference with the starting vortex from the preceeding blade occurs. The interference effects are generally most severe with the first intersection as can be seen by the thrust response and occur approximately every 90^o of azimuth travel. For the $\Delta\ \theta = 15^o$ case interference extends from 75^o to 90^o from the direct numerical integration, but the change in C_T is only 0.025. At 180^o of blade travel no significant interference effects are noticeable. For $\Delta\ \theta = 7^o$, Figure (36), the first interference region extends from approximately 77^o to 98^o with the maximum change in C_T of 0.084. A second but weaker region appears at 175^o to 182^o. It should be observed that the interference effect for the smaller azimuth steps are more pronounced following the intersection due to the larger number of disoriented vortex segments in the wake. This is borne out by the results for $\Delta\ \theta = 3^o$ shown in Figure (37). Following the intersection with the starting vortex the interference effects appear to decrease in magnitude but do not really die out. For this small step size the region of interference extends from about 48^o to 93^o, a region covering 45^o of blade travel as compared to 21^o for the $\Delta\ \theta = 7^o$ and 15^o for $\Delta\ \theta = 15^o$. This increase in the size of the region is due to the

more gradual progression of the blade into the starting vortex for the smaller step size. The intensity of the interference is much greater for the $\Delta\theta = 3^{o}$ with a maximum change in $C_T = 0.27$ observed.

The steady state C_T given by equation (52) is also shown on Figures (35) through (37). This includes real fluid effects by utilizing two-dimensional static airfoil data and the section angle of attack determined by equation (45). The average values of C_T determined compare favorably with the numerical integration but the details of the interference are markedly different. This is due to the blade angle of attack being dependent on the induced drag as well as thrust and the two can be entirely different in behavior.

For $\Delta\theta = 15^{o}$ interference effects at $\theta = 90^{o}$ look much the same as for the numerical integration scheme. The magnitude of the C_T change are approximately equal, but the region itself is shifted by 15^{o}, extending from $\theta = 90^{o}$ to 115^{o}. At $\theta = 180^{o}$ a strong interaction region is observed which reflects the interference on C_{D_i}. For $\Delta\theta = 7^{o}$ the area of interference extends from about 70^{o} of azimuth and extends to 97^{o} so that it is somewhat broader than the numerical integration result. The maximum C_T change is 0.093, slightly larger than the numerical result. The region with $\Delta\theta = 3^{o}$ extends from $\theta = 72^{o}$ to 96^{o}, not nearly as wide as the result by lifting surface theory. Further, the maximum change in C_T is only 0.135, much less than the direct integration.

Comparison of the C_T with the measured steady state values (Figure (35) through (37)) are not particularly encouraging since the analysis seems to overpredict by a factor of two. Because of

this poor correlation a classical propeller analysis utilizing the Prandtl tip loss factor was applied to the cited propeller configuration and compares quite favorably with the lifting surface analysis. On this basis it is felt that the experimental data is seriously lacking. The fact that a non-standard airfoil section was used make estimations of the airfoil characteristics difficult at best; however data was synthesized for the section following guidelines of Reference (9). In the numerical analysis thickness effects were accounted for in both the lift curve slope and minumum drag coefficient. However stall effects were not included, either in terms of a limiting $C_{l_{max}}$ or a drag rise. It shall be shown subsequently that the inboard sections fo this propeller could be stalled so a definite effect would be felt if these were included but probably not a 50% thrust decrease. Because of the non-standard section, camber could not be estimated and so was assumed to be zero.

Figures (38) through (40) show the power characteristics of the propeller configuration. The induced power by numerical integration and the total power by equation (52) are compared with the momentum value of induced power, the total power of Reference (9) and total power predicted by classical theory. It can be seen immediately that good correlation exists between the measured result of Reference (9) and equation (52). Unfortunately, the measured value does not correspond to reasonable estimates. For example, the measured $C_p = 0.032$ corresponds to the momentum C_{p_i} based on the measured $C_T = 0.117$ with nothing left over for profile losses.

This coupled with the large discrepancy between the measured value and the results of classical analysis further reduce the confidence in the experimental data.

The induced powers determined by the vortex lattice technique compare favorably with the total power result of classical analysis. It is readily seen that the C_{p_i} is over-predicted when compared to the momentum theory value although increasing this value by 15% to account for the vortex wake (16) gives $C_{p_i} = 0.0835$ and better correlation.

Figure (38) shows the results for $\Delta\theta = 15^{o}$. Both C_{p_i} and C_p by equation (52) show relatively weak interference effects at 90^{o} and much stronger effects at 180^{o} (change in $C_{p_i} = 0.046$). Again, the interference regions are about the same size but the effects are different. The results for $\Delta\theta = 7^{o}$ are shown in Figure (39). Here the strong interference region exists in C_{p_i} at the first interaction ($70^{o} \leq \theta \leq 98^{o}$) and is preceeded by a decrease associated with a slower progression into the starting vortex of the preceding blade. The maximum change in $C_{p_i} = 0.096$. At 180^{o} the interference is not discernible. Finally, in Figure (40) for $\Delta\theta = 3^{o}$ the results are essentially the same as the 7^{o} case except the blade entrance into the starting vortex is much more pronounced. The change in C_{p_i} is 0.21, larger than either of the other cases.

The effect of azimuth step size on the bound circulation distribution is given in Figure (41). The azimuth station is $\theta = 90^{o}$, in a strong interference region. Two chordwise vortices are considered. The first bound vortex has a very regular shape with a

maximum at y/R = 0.5 for all three azimuth steps ($\Delta\theta = 3^o, 7^o, 15^o$). Small distortions appear inboard due to the inboard distortions of the vortex wake. The second bound vortex shows relatively violent oscillations radially, at least for $\Delta\theta = 7^o, 3^o$. These oscillations can occur from two possible primary causes. One is the possibility of a vortex element coming too close to a control point and having its influence weighted too strongly. Another is the relative closeness of the last chordwise control point to both the last (in this case, second) bound vortex and the shed vortex nearest the trailing edge which reflects the time rate of change of bound circulation. Analysis of the numerical results indicates that indeed the fluctuations in this bound vortex are of the same order as the spanwise variations in shed vorticity. Hence the time dependent change in total chordwise loading is felt predominantly in the loading nearest the trailing edge. The strength of shed vorticity in turn, is determined by the inflow at the control points and can be measurably affected by the relative position of wake element and control points. $\Delta\theta = 3^o$ shows the most radial oscillations ultimately indicating more wake segments in the vicinity of the blade.

The effect of azimuth step size on the radial distribution of blade angle of attack is shown in Figure (42). At $\theta = 30^o$, blade section angle of attack is relatively insensitive to the time step size. However, the angle for maximum lift coefficient for a NACA0012 airfoil is superimposed in order to show the possible stall region, out to approximately 40% span. At $\theta = 90^o$, the blade-wake element interference is dominant and no real comparison

can be made. The same trend as in the $\theta = 30^{o}$ case can be observed, but the fluctuations around this mean are dependent ultimately on the nearness of one or more wake segments to a local point.

Figure (43) shows the thrust and power distribution through the interference region at $\theta = 90^{o}$. The violent fluctuations indicate extremely strong interactions between wake segments and load points. The thrust and power distribution of Reference (9) are shown for comparison and, interestingly, the thrust distributions for $\Delta\theta = 15^{o}$ compares qualtitatively favorably with a peak at about 70% radius.

The relative accuracy of the vortex lattice technique from the runs examined has been difficult to assess. The wake patterns for $\Delta\theta = 15^{o}$ and $\Delta\theta = 7^{o}$ become unstable after $\theta = 165^{o}$ with wake elements taking large excursions from the region of influence. Once they move away, the lengths involved become so large that they cannot return either by interactions with other vortices or by localized induction effects. The excursions become great enough that the one-step Euler integration scheme for the wake displacements is invalid as is the second order Taylor series for the locally induced velocity. As a result the assessment of the method has been based on the performance predicted within the first 180^{o} of azimuth travel. Some conclusions as to average performance have been based on the more or less steady case generated before the first interference. In fact careful evaluation of the shed vorticity in this region between the start of the motion and the first blade-starting vortex interaction leads to a tentative favorable con-

clusion regarding the induced power. Since the propeller blades are reacting to an unsteady flow field shed vorticity is being produced and thus contributes to the induced drag and power. Before the interference takes place the shed vorticity decreases as the blade motion progresses from start and the induced drag tends to decrease as well. This result is best seen in the $\Delta\theta = 3^{o}$ case but is also observed in simpler configurations yet to be discussed. After the interference takes place the effects of the more or less disordered vortex segments are predominant and conclusions regarding average performance are nearly impossible to obtain.

The wake configurations corresponding to $\Delta\theta = 15^{o}$, 7^{o}, 3^{o} for an interaction core radius $h_c = 10^{-6}$ ft. are shown in Figures (44) through (46), respectively. Blade rotation is counterclockwise. For $\Delta\theta = 15^{o}$, large excursions in the tip vortex filament are observed at the end of the second time step ($\theta = 30^{o}$). The distortions in the tip filament worsen as the motion progresses although the motion is a spiral type. Beyond $\theta = 90^{o}$ the distortions increase until complete breakdown at $\theta = 180^{o}$ occurs. Beyond $\theta = 90^{o}$ inboard wake distortions increase due to wake-wake interference between the blade wake being observed and the starting vortex from the preceeding blade, and blade-wake interference between the observed wake and the next following blade. As noted previously, once a point is driven out of the flow field by an interaction it never returns. It is too far away to be measurably affected by interactions and the ensuing element lengths are too great for the second order Taylor series expansion to the local

geometry to be valid. Because of applying conservation of total vorticity the circulations decrease further decreasing the locally induced velocity of the filament on itself, but it also decreases the velocity induced by the filament on the majority of the blade and wake elements. The performance of the propeller is then most dependent on those vortex segments of length approximately $R\Delta\theta$ which remain in the vicinity of the propeller.

The wake generated by $\Delta\theta = 7^{\circ}$ azimuth steps is presented in Figure (45). The motion over the first 90° of travel is much the same as the $\Delta\theta = 15^{\circ}$ case but the spiral distortion in the tip vortex are not as evident. On the other hand the formation of the starting vortex is much more pronounced. At $\theta = 90^{\circ}$ effects of wake-wake and blade-wake interference can be observed. The tip filament begins relatively large excursions and finally reaches an unstable situation at $\theta = 175^{\circ}$. At this θ there are indications of a strong wake-wake interference just behind the blade trailing edge.

What appeared to be the most reasonable wake was generated by the smallest time increment $\Delta\theta = 3^{\circ}$ and shown in Figure (46). This starting vortex appears to start to form better than $\Delta\theta = 15^{\circ}$ and the tip vortex begins as spiral motion. Like the other cases the wake remains relatively undisturbed through nearly the first 90° of travel. Distortions in the starting vortex are noticeable at $\theta = 50^{\circ}$ and become more pronounced at 75° to 78° due to blade-wake interference. At $\theta = 81^{\circ}$ the tip filament starts a definite spiral motion and $\theta = 84^{\circ}$ sees the inboard filaments beginning the

C-2

same motion. The distortions in this region tend to intensify as time progresses but not necessarily toward divergence so it may be that beyond $\theta = 120^{o}$ the wake would remain stable although a chance encounter between two filaments is all that is necessary to promote instability.

An observation of all three of the wakes is that the spiral motion of the tip filament (and any others) describes the basic flow pattern at sudden start as observed by Taylor.

From the preceding results the breakdown of the analysis is obviously tied to the interaction between vortex elements and this is, in turn, governed by the core radius and the azimuth increment (time step) employed. To assess the effect of core radius on the wake, computations were performed, Figure (47), for a core radius of 10^{-10} ft. and a proportional core, h_c ~ length of the element, Figure (48). For $h_c = 10^{-10}$ ft., the pattern is much the same as for 10^{-6} ft., but when the instability is observed at $\theta = 180^{o}$ it is much more violent. The proportional core, however, while yielding relatively large excursions showed no tendency to promote instability in 315^{o} of travel. It may be the proportional core, in which the radius is proportional to the filament length, that warrants further consideration.

Azimuth increments smaller than $\Delta\theta = 3^{o}$ were not considered. The vast amount of computation time required to obtain this much information, 20000 sec. per run, seriously restricts the usefulness of the present formulation even for research work. In order to reduce computation time, it became necessary to consider simpler

configurations and return to $\Delta\theta = 15^{\circ}$ increments.

The first case considered was a one-bladed configuration, core radius = 10^{-6} ft., with the spanwise loading modelled by 5 trailing vortices and the chordwise loading modelled by a single bound vortex, the Weissinger model. Rubbert's rules for the tips (34) have been observed. A blade travel of 375° could be obtained in 100 sec. of computation time. Three runs were made to assess the effect of even spaced and cosine law spaced elements, spanwise; and the effect of including blade twist in satisfying the boundary condition. The latter is accounted for by determining λ_{il} according to equation (8), and this in turn, accounts for the spanwise deflection of the flow due to twist. The results are summarized in Figure (49). Using the case of even spacing and no twist as a base, inclusion of twist effects in the boundary condition increases the predicted thrust very slightly, approximately 2%. Cosine spacing over-predicts from 7% to 8%. The predictions are quite close up to the point of interaction in which case even spacing and cosine spacing are quite dissimilar due to the different length vortex segments involved.

Inclusion of blade twist also increases C_{P_i} by approximately 4.5%, slightly larger than a 3% increase that can be estimated from simple momentum theory for a 2% increase in C_T. However this implies a slightly larger power at a given thrust and, even if only a few percent change is involved, since accuracy within the last 10% of performance is desired this could be an important consideration.

An observation of this single bladed configuration is its behavior as a low aspect ratio wing. Even though the blade is AR = 5, the propeller thrust response to the impulsive start is more similar to the previously reported results for the AR = 3 wing. That is, following the impulsive start the propeller drops quickly to the steady state C_T much the same as the AR = 3 wing C_L responds. There is very little recovery to a higher value as in the case of high AR wings (see Figure (13) for the infinite aspect ratio wing).

Figures (50) and (51) show the effect of spanwise vortex spacing on the spanwise thrust distribution and section angle of attack distribution respectively. Both distributions are quite regular at $\theta = 0^\circ$ and $\theta = 180^\circ$ with major differences occuring at $\theta = 360^\circ$, within the first interference region. An area of large negative thrust occurs near midspan for cosine spacing; a region of small negative thrust is inboard for regular spacing. Large negative angles occur inboard for regular spacing; cosine spacing yields all positive angles.

At $\theta = 0^\circ$, the C_T distribution is symmetrical about the mid-span while the cosine spacing has a maximum value at approximately 62.5% radius. At $\theta = 180^\circ$, maximum is at 62.5% span for even spacing while, for cosine spacing, the maximum has moved to 85% radius.

In a further attempt to assess the value of considering simplified geometry in the interest of savings in computation

time, a one blade and two blade configuration were run for 1000 seconds. The performance results are summarized in Figure (52) and (53). Both propellers used 5 spanwise even spaced vortices and a single bound vortex to model the loading. Azimuth steps of $\Delta\theta = 15^{o}$ were used. The analysis of Appendix B yielded a core radius of 10^{-3} ft. and $\lambda_{i1} = 0^{o}$. The single bladed propeller turned through 960^{o} of travel while the two bladed configuration rotated 870^{o}. In both cases these simpler configurations reinforce the observations made for the four bladed case. A small aspect ratio wing type response in C_T and C_{Pi} are observed up to the first intersection ($\theta \cong 360^{o}$ for the single bladed and $\theta \cong 180^{o}$ for the two bladed). The single bladed propeller also shows a gradual decline in C_{Pi} toward the momentum theory value prior to the first intersection. The average values obtained are nominally 25% and 50% the four bladed, excepting interference effects, indicating that relatively simple configurations can be used to assess average performance.

The major interference areas are quite well defined. The single bladed propeller has definite spikes at $\theta = 360^{o}$, 720^{o} in thrust and induced power. The maximum change in C_T is 0.035 at $\theta = 360^{o}$ and 0.0128 at $\theta = 720^{o}$. The change in C_{Pi} is 0.048 at $\theta = 360^{o}$ and 0.0246 at $\theta = 720^{o}$. Within the first two revolutions the average performance is relatively smooth, but beyond $\theta = 720^{o}$ it appears the presence of discrete vortex segments provides severe interference conditions.

The two bladed propeller, Figure (53), shows essentially the

same characteristics. Major interference regions occur twice as frequently, $\theta = 180^{o}$, 360^{o}, 540^{o} and 720^{o}. The maximum change in C_T and C_{pi} are more intense ($\Delta C_T \doteq 0.110$, $\Delta C_{pi} = 0.087$ @ $\theta = 360^{o}$). Also, the fluctuations between interference regions do not die out as rapidly.

The wake of the two bladed configuration is shown in Figure (54). It consists of five trailing vortices, a time step corresponding to $\Delta\theta = 15^{o}$ in azimuth and $h_c = 10^{-3}$ ft. The motion persists through 525^{o} of azimuth before an instability occurs. Excursions in the spiral motion are quite large, probably too large for realistic flow geometries. It can be noted also that very little distortion of the trailing vorticity until acted upon by a blade or wake interference is observed (at $\theta = 150^{o}$ to 180^{o}, for example). This is due directly to the relatively large increment in time prescribed by $\Delta\theta = 15^{o}$. By way of comparison, the wake distortions for the finite wing were carried out for $V\Delta t/c = 0.1$. For the propeller, $V\Delta t/c \sim (V_T\Delta\theta/\omega c) = 1.2$, over 10 times the value for the wing. As a result, the time of the motion is much too great to allow a proper starting motion to form and the vortex segments established are too long for the Taylor series expansion on the local induced velocity to be valid. To reduce $V\Delta t/c$ to 0.1 for the propeller in order to promote reasonable locally induced effects requires a $\Delta\theta$ of approximately 1.5^{o}, or approximately one half of the smallest value considered. This has the undesirable effect of increasing computation time.

The large excursions and eventual instability are due primarily to cumulative effects. The results of Appendix B generally restrict the motion properly, but cannot account for summation effects when one point comes under the strong influence of several vortex segments. To counteract this effect, some limit has to be put on the displacement due to cumulative velocities or the limit on displacement due to one velocity increment must be strongly reduced, perhaps to a size on the order of boundary layer thickness. A positive note can be observed in this crude wake, however, and that is the apparent tendency to generate the Taylor "doughnut" (13) during the impulsive start.

The results of the analysis indicate crude geometries can be utilized to predict average performance, but the corresponding wakes are generally unstable and unrealistic. To verify this completely requires a solution to be run for several revolutions to give the motion time to reach a steady state. In order to obtain good wake geometries requires very small azimuth steps (time steps) as well as a relatively large number of spanwise segments in order to keep the vortex segments relatively small and allow the wake flow time to develop. This leads to unrealistically large computation times for the present method. However, the present formulation is quite inefficient from a computation standpoint. On each panel the wake induced velocities must be computed four times, once at the control point to determine the bound circulation, and then at three load points on the horseshoe vortex bounding the panel.

The existing computations perform the four integrations over the wake utilizing the Biot-Savart Law. A method has been recently conceived to reduce the time required for the wake integrations by only computing the Biot-Savart Law once for a given panel and wake geometry. Because the relative panel geometry is fixed; i.e., the distances between a control point and the three load points at the vortex midpoints is fixed. The velocity increments at one point, say the control point, can be computed for a wake segment and modified by factors containing the relative panel geometry. The method was conceived after the acquisition of the previous data and as yet is unproven. If feasible, however, it could reduce computation time by as much as 50% to 75%. A two-dimensional discussion of the method is given in Appendix C. The three-dimensional counterpart will be more complex but no more difficult to apply.

Chapter V

Summary and Conclusions

The foregoing analysis applies vortex lattice techniques to the problem of a lifting surface starting impulsively from rest. The lifting surface can be an infinite wing, a finite aspect ratio wing or a propeller in static operation. The wake generated can be flat and constrained to the plane of the lifting surface motion or free to deform under its own induced velocity field. The impulsive start condition allows the wake to be known at every instant of time and eliminates the need for an assumed initial shape. The wake deforms under the influence of mutual interaction between filaments and the velocity each filament induces on itself. Application of lifting surface techniques permits an exact solution for the chordwise and spanwise loading to be determined. Even though difficulties in correlating the analysis for the statically thrusting propeller with limited experimental results for the propeller exist, it is believed the present analysis is basically sound since it does compare well with classical methods for the propeller as well as for the finite wing.

Prior to investigating the lifting surface technique, some time was spent in observing the velocity field of the elementary straight line vortex segment in hopes that some a priori assumptions regarding the wake and the number of elements needed to describe it could be made. These were generally unsuccessful because the orientation of the free wake elements had to be computed and this is the most time consuming aspect of the problem. However, one interesting result was obtained

regarding the magnitude of the induced velocity. The velocity on the bisector of a straight line vortex segment is essentially two-dimensional for $h/\ell \lesssim 0.1$ and varies as $1/r$. For $h/\ell \gtrsim 1.0$, the magnitude varies as $1/r^2$. Thus, with a vortex filament of prescribed geometry which is to be numerically broken up into finite length segments, the magnitude of the induced velocity calculated from the Biot-Savart Law can be simplified so that a saving in computation time is obtained.

To evaluate the present analysis, the simplified geometries corresponding to a flat, rectangular wing starting impulsively from rest were considered first. These wings were allowed to generate flat, linearized wakes and deforming, self-convecting wakes, with and without the localized self-induction velocity. In general it was found that the wing C_L and C_{D_i} could be predicted quite well provided the velocities at the bound vortex midpoints were used. Further, the wing C_L and C_{D_i} are relatively unaffected by wake roll-up.

The problem of determining the wake roll-up characteristics, notably rate as well as final geometry, was also considered. It is well known that final geometry can be satisfactorily obtained by the usual analyses employing Trefftz plane aerodynamics, but the roll-up rates by this approach are much too slow. The results of the numerical analysis indicate that the accurate prediction of the wake roll-up geometry and rate can be obtained provided that the details of the motion at the instant of start and vortex filament self-induced velocities are considered. With the inclusion of self-induced velocities proportional to the local curvature, calculations show that the wake roll-up behind a lifting wing is initiated after only 0.5 chords of travel. This is

primarily due to spanwise induced velocities which are of the same order of magnitude as the downwash so that the filaments lie on a spiral trajectory. Without these self-induced velocities, the downwash is an order of magnitude greater than the spanwise flow so that a two-dimensional character of the motion is maintained and there is about three chord lengths of wing travel before any roll-up is noticed. This is more in line with Trefftz plane results.

After the basic validity of the analysis, including the wake roll-up model, was established for the finite wing, a four-bladed propeller configuration was run for comparison with experimental results. It was found that the theoretical results for the propeller configuration did not correlate well with the experimental results. In an effort to obtain further comparisons, a classical Prandtl analysis was performed and calculations based on momentum theory were made. In general, reasonable comparisons in thrust prediction can be obtained between the present analysis and the Prandtl analysis while the actual measurements of Reference (9) were considerably lower. Then, using an average C_T of the value predicted by either the present analysis or the Prandtl analysis, a momentum C_{p_i} was calculated. It was found that the present analysis compares favorably with this C_{p_i} value as well as with the total C_p of the Prandtl analysis. However, all of these calculated values are much higher than the measured C_p of Reference (9), indicating that possibly the measured C_p is too low. The error observed in these results was much greater than anticipated, particularly since the finite wing results were so encouraging.

Further error in the analysis could be due to poor synthesis of the airfoil section data. Although care was taken and the guidelines of Reference (9) were followed, the airfoil section was non-standard and difficult to describe. Poor estimates of the drag characteristics could explain, in part, discrepancies in the power calculations among analyses with reasonable thrust comparisons.

Error might also be due to the relatively short wakes generated. Even though extremely long computational run times (20,000 sec.) were performed, only about two revolutions of wake could be generated at best, and it is quite conceivable that this is not enough to predict the steady state performance. It was noted that the average C_T and C_{P_i} respond to the impulsive start much like a low aspect ratio wing. That is, following the impulsive start the performance drops very quickly to what appears to be the steady state value. It is possible that steady state has not been attained and more revolutions are necessary. This would lead to an increased inflow which, by decreasing blade angle of attack, could lead to decreased thrust prediction. Regions of inboard stall would be determined by this inflow, and performance would be measurably affected by the extent of these regions.

Finally, there is an error due to the vortex wakes deposited by the propeller blades. The time steps considered were much too large to predict accurate wakes (except perhaps for the $\Delta\theta = 3^o$ case). As a result, all the wakes of the four-bladed configuration except $\Delta\theta = 3^o$ became unstable; this instability was enhanced by interaction core radii that were too small. The resulting wake geometries then contained extremely long straight line vortex segments which, once formed by a

strong interaction induced velocity acting over a relatively large time step, could produce completely erroneous velocities at the blades. To make matters worse these segments might never return to a reasonable geometry as time progresses since they might never pass through enough interactions to counteract the effect of one strong one. It should be noted that wake instabilities noted in the analysis are believed to be only numerical with no physical counterpart.

Even though the comparison of theoretical and experimental results leaves much to be desired, some parametric results were successfully obtained. Small time steps (1.5^{o} to 3^{o} in azimuth) are required for accurate wake prediction. This is necessary to determine an accurate vortex filament radius of curvature for calculating the locally induced effects. This is also a requirement to obtain reasonable vortex induced curved paths for the wake points from the one-step Euler integration scheme which can only provide straight line translation of a point.

The sensitivity to time step of blade airloads due to passage through a vortex is significant. The smallest time step, $\Delta\theta = 3^{o}$, shows a much greater fluctuation in both C_T and C_{p_i}, as well as a much larger azimuthal extent of interference, than does the $\Delta\theta = 15^{o}$ case. The accuracy of blade-wake interactions not only depends on small time steps, but also on interaction core radii large enough to limit the movement of a wake point to a reasonable value.

Inclusion of blade twist in satisfying the boundary condition increased the computed average C_T by approximately two percent. This is a relatively small effect, but since interest in static performance prediction is generally within the last 10 percent, this is significant.

Variations in spanwise spacing were examined by comparing the results of an evenly spaced configuration with a cosine spacing. Cosine spacing tends to predict average C_T's approximately seven percent to eight percent higher than even spacing. Corresponding wake interference regions exhibit completely dissimilar characteristics. This indicates that the freedom of choice in spacing one has in modeling the spanwise loading for a finite wing with a flat wake does not carry over to the propeller or into regions of aerodynamic interference.

In order to reduce computation time, propeller geometries utilizing coarser spanwise spacings were considered. The results indicate that for computing average performance as few as four or five spanwise panels could be considered.

Time dependent changes in chordwise loadings are felt predominantly in loadings nearest the trailing edge. This is significant in the higher harmonics of aeroelastic torsional modes and noise.

The conclusion of this work must admit that the accuracy of the present analysis when applied to the statically thrusting propeller has not been satisfactorily demonstrated since correlation with the selected experimental results was poor. Even though the basic formulation is believed sound from comparison with other analyses and finite wing results, final correlation will have to await better experimental results, more accurate airfoil section characteristics, relief from the numerical inaccuracies associated with the aerodynamic interference region and larger computational runs to numerically establish the wake. This procedure, like other vortex lattice techniques, uses an inordinate amount of computer time due to the

repeated calculations of the Biot-Savart Law in the wake. Unfortunately, no wake simplification or approximations are apparent because of the importance of the nonlinear flow of the induced velocity field. This is further aggravated by the small time step requirement to compute interference aerodynamics of the problem accurately. This seriously restricts the usefulness of the analysis, at present even as a research tool. However, vortex lattice techniques are those which most readily apply to nonlinear aerodynamic problems so that further attempts at reducing the computation time of this analysis, as well as accepting long time computer runs, are perhaps justified, at least in research problems.

In spite of the inconclusiveness of the primary results of this analysis, several positive results have been obtained. Perhaps the most significant of these is the modeling of the wake roll-up with the localized induction concept while considering the three-dimensional flow about a lifting surface starting from rest. Inclusion of blade twist in satisfying the flow tangency boundary condition has been shown to give a small but significant increase in thrust. It has been shown that relative freedom of choice in selecting the spanwise spacing for the vortex lattice does not apply to propellers or any problem in which aerodynamic interference is important. It has been shown that average performance can be obtained, if necessary, by considering coarse spanwise spacings. A cursory investigation into the chordwise loadings shows that time dependent changes are felt nearest the trailing edge.

Chapter VI

Recommended Further Research

In spite of the generally favorable trends established from applying vortex lattice techniques to the statically thrusting propeller, the primary objective of obtaining the high degree of accuracy necessary to correlate theory and experiment has not been accomplished. However, the major problem areas in the aerodynamic modeling have been identified and the foregoing analysis represents a tool to investigate these areas. Thus to extend the present analysis further into the modeling of propeller performance continuing investigations are strongly urged.

Efforts to reduce computation time must continue. Attempts to more accurately predict the potential inflow lead to small time increments corresponding to an azimuth step size, $\Delta\theta \lesssim 1.5^{o}$, fully one-half the smallest value considered and at least one tenth a value at present practical. This limit has been established by estimates necessary to promote good wake roll-up characteristics. Attempts in the present analysis to reduce computer central processor time (and core storage) with special data handling techniques have been generally unfruitful. As a start in this direction, the method of Appendix C can be extended to three-dimensions and applied.

Reductions in computation time would also permit more accurate representations of the wake. The numerical integration scheme considered in the present analysis is a simple one-step Euler scheme,

shown to be less accurate (54) than either a Runge-Kutta method or a one-step predictor-corrector technique. The inherent inaccuracy of the method lies in the fact that points can only translate under the influence of a vortex induced velocity whereas the true path is circular. Unfortunately this method is the most economic from the point of view of computation time and core storage, although to get a sufficiently close approximation to the circular path requires very small time increments.

Another, perhaps more subtle, error associated with the wake modeling and which points toward smaller time steps as a solution is the representation of the vortex elements in the wake by straight line segments. Figure (55) shows the effect of curvature on the velocity induced along the bisector of the vortex filament. The two models consist of joining two points by 1) a straight line segment of length, 1, and 2) a circular arc, radius of curvature, R. "e" is a point on the bisector and "Z" is the maximum distance from the straight line segment to the circular arc (the "camber" of the arc). For the case shown the circular arc is a semi-circle and Z = R. It can be seen that the velocity induced by the two configurations are similar only beyond approximately one segment length on the concave side and one half segment length on the convex side. As the filaments are approached from either side the induced velocities quickly become dissimilar and between the two filaments the velocities have opposite sign. Hence any point falling within this region will be convected totally incorrectly. As the "camber" of the arc decreases (radius of curvature increases) this region of

inaccuracy decreases. Assuming the two endpoints to be formed by the consecutive motion in time of a lifting element, the inaccuracy can be made to vanish only in the limit as the time step vanishes. Numerically, this points to extremely small time steps.

Core radius criteria for consistent reasonable predictions of blade-wake and wake-wake interference conditions should be established. The present analysis has shown that to correctly model the vortex wake and eliminate the singularity in the Biot-Savart Law two vortex core radii can exist. One governs the local induction effect and the other determines the interference or interaction effects. Criteria for firmly establishing the former can probably be determined from the original references (46, 47, 48, 49). The latter will probably require more effort; the various methods considered have been mentioned in Appendix B of this report. Johnson and Scully (55) indicate core radii ranging from one tenth chord to 20% radius are necessary. A reasonable and consistent method for estimating these core radii should be available.

An alternate method to equation (52) for viscous correction is needed. The present approach, while corresponding to classical propeller theory, is numerically inefficient since it is valid only for steady state. A method such as that of Reference (29) is simpler to apply, numerically more efficient and is probably easier to extend into the unsteady regime.

Valid experimental results for comparison are needed. This includes blade load data as well as average preformance.

Perhaps rotor data could be used, at least initially.

Long time runs, at least on the simple configurations, should be made to establish steady state wake configurations. Comparisons could then be made with existing flow visualization results to determine the accuracy and stability of the model.

References

1. Carpenter, Paul, J., and Paulnock, R. S., "Hovering and Low Speed Performance and Control Characteristics of an Aerodynamic - Servocontrolled Helicopter Rotor System as Determined on the Langley Helicopter Tower", NACA TN 2086, May 1950

2. Rabbot, J. P. Jr., "Static Thrust Measurements of the Aerodynamic Loading on a Helicopter Rotor Blade", NACA TN 3688, July 1956

3. Norton, Harry T., Jr., "Static-Thrust Characteristics of the NACA 8.75-(5)(05)-037 Dual-Rotation Propeller", NACA RM L56C27, July 10, 1956.

4. Adams, G. N., "Propeller Research at Canadair Limited", CAL/USAAVLABS Symposium Proceedings, Vol. 1, Propeller and Rotor Aerodynamics, June 22-24, 1966

5. Borst, H. V., and Ladden, R. M., "Propeller Testing at Zero Velocity", CAL/USAAVLABS Symposium Proceedings, Aerodynamic Problems Associated with V/STOL Aircraft, Vol. 1, Propeller and Rotor Aerodynamics, 22-24 June 1966

6. Erickson, J. C., Jr. and Ordway, D. E., "A Theory for Static Propeller Performance", CAL/USAAVLABS Symposium Proceedings, Vol. 1, Propeller and Rotor Aerodynamics, June 22-24, 1966.

7. Jenny, D. S., Olson, J. R., Landgrebe, A. J., "A Reassessment of Rotor Hovering Performance Prediction Methods", Journal of the American Helicopter Society, Vol. 13, No. 2, April 1968.

8. Chopin, M. H., "Propeller Static Performance Tests for V/STOL Aircraft", ASD-TR-69-15, Aeronautical Systems Division, A. F. Systems Command, W.-P. AFB, January 1970. Part 1 - Summary Report Part 2 - Test Data (Appendix 3)

9. Gilmore, D. C., "Advanced V/STOL Propeller Technology-Surface Pressure Measurements on a Propeller Blade Operating at Zero Advance Ratio", Tech. Rept. AFFDL-TR-71-88, Vol. 5, Sept. 1971, Air Force Flight Dynamics Laboratory, Air Force Systems Command, Wright-Patterson AFB.

10. Ladden, R. M., "Static Thrust Prediction Method Development-Part 1, Prescribed Wake Static Propeller Method Dvelopment", Advanced V/STOL Propeller Technology, TR AFFDL-TR-71-88, Vol. II, AF Flight Dynamics Lab, AF Systems Command, W-PAFB, Sept. 1971

11. Clark, D. R., and Landgrebe, A. J., "Wake and Boundary Layer Effects in Helicopter Rotor Aerodynamics", AIAA Paper No. 71-581, AIAA 4^{th} Fluid and Plasma Dynamics Conference, June 21-23, 1971

12. Landgrebe, A. J., "An Analytical and Experimental Investigation of Helicopter Rotor Hover Performance and Wake Geometry

Characteristics", USAAMRDL Tech. Rept. 71-24, Eustis Directorate, U.S. Army Air Mobility Research and Development Laboratory, Fort Eustis, Va., June 1971

13. Landgrebe, A. J. and Cheney, M. C., Jr., "Rotor Wakes-Key to Performance Prediction", Presented at the Symposium on Status of Testing and Modeling Techniques for V/STOL Aircraft (Session on Mathematical Modeling and Simulation Methods) Mideast Region of the American Helicopter Society, October 26, 1972

14. Taylor, M. K., "A Balsa-Dust Technique for Air-Flow Visualization and Its Application to Flow Through Model Helicopter Rotors in Static Thrust", NACA TN 2220, November 1950

15. Carpenter, P. J. and Fridovich, B., "Effect of a Rapid Blade Pitch Increase on the Thrust and Induced Velocity Response of a Full-Scale Helicopter Rotor", NACA TN 3044, November 1953

16. McCormick, B. W., Jr., "Aerodynamics of V/STOL Flight", Academic Press, 1967

17. McCormick, B. W., Eisenhuth, J. J., Lynn, J. E., "A Study of Torpedo Propellers - Part I", Ordnance Research Laboratory, Serial No. NOrd 16597-5, March 30, 1956

18. Goldstein, S., "On the Vortex Theory of Screw Propellers", Proceedings of the Royal Society, A123, 440, 1929

19. Tanner, W. A., and Wohlfeld, R. M., "Vortex Field, Tip Vortex, and Shock Formation on a Model Propeller", Proceedings Third CAL/AVLABS Symposium, Aerodynamics of Rotary Wing and V/STOL Aircraft, Vol. I, Rotor/Propeller Aerodynamics Rotor Noise, June 18-20, 1969.

20. Piziali, R. A. and DuWaldt, F. A., "A Method for Computing Rotary Wing Airload Distributions in Forward Flight", TCREC Tech. Rept. 62-44, November, 1962

21. Crimi, P., "Theoretical Prediction of the Flow in the Wake of a Helicopter Rotor - Part I - Development of Theory and Results of Computations", CAL No. BB1994-s-1, September 1965

22. Trenka, A. R., "Prediction of the Performance and Stress Characteristics of VTOL Propellers", CAL/USAAVLABS Symposium Proceedings, Vol. I, Propeller and Rotor Aerodynamics, June 22-24, 1966.

23. Scully, M. P., "A Method of Computing Helicopter Vortex Wake Distortion., MIT ASRL TR 138-1, June 1967

24. Landgrebe, A. J., "An Analytical Method for Predicting Rotor Wake Geometry", JAHS, 14, Oct. 1969

25. Erickson, J. C., "A Continuous Vortex Sheet Representation of Deformed Wakes of Hovering Propellers", Proceedings Third CAL/AVLABS Symposium Aerodynamics of Rotary Wing and V/STOL

Aircraft, Vol. I, June 18-20, 1969

26. Clark, D. R. and Leiper, A. C., "The Free Wake Analysis: A Method for the Prediction of Helicopter Rotor Hovering Performance", Journal of AHS, Vol. 15, No. I, January 1970

27. Rorke, J. B. and Wells, C. D., "The Prescribed Wake-Momentum Analysis", Proceedings Third CAL/AVLABS Symposium, Aerodynamics of Rotary Wing and V/STOL Aircraft, Vol. I, June 18-20, 1969

28. Landgrebe, A. J., "The Wake Geometry of a Hovering Helicopter Rotor and Its Influence on Rotor Performance", JAHS, Vol. 17, No. 4, Oct. 1972

29. Sadler, S. Gene, "Development and Application of a Method for Predicting Rotor Free Wake Positions and Resulting Blade Airloads - Vol. 1 - Model and Results", NASA CR - 1911, Dec. 1971

30. Landahl, M. T. and Staark, V. J. E., "Numerical Lifting Surface Theory - Problems and Progress", AIAA Journal, Vol. 6, No. 11, November 1968

31. Falkner, V. M., "The Calculation of Aerodynamic Loading on Surfaces of Any Shape, R & M, No. 1910, Aeronautical Research Council, Great Britain, August 1943

32. Falkner, V. M., "The Solution of Lifting-Plane Problems by Vortex Lattice Theory", R & M No. 2591, Aeronautical Research Council, Great Britain, September 1947

33. Kulakowski, L. J. and Haskell, R. N., "Solution of Subsonic Nonplanar Lifting Surface Problems by Means of High-Speed Digital Computers", Journal of Aerospace Science, Vol. 28, No. 2, February 1961

34. Rubbert, P. E., "Theoretical Characteristics of Arbitrary Wings by a Non-Planar Vortex Method", Document No. D6-9244, The Boeing Co., 1964

35. Hedman, S. G., "Vortex Lattice Method for Calculation of Quasi-Steady State Loadings on Thin Elastic Wings in Subsonic Flow", Rept. 105, The Aeronautical Research Institute at Sweden, 1966

36. Belotserkovski, S. M., "Calculating the Effect of Gusts on an Arbitrary Thin Wing", Mekhanika Shidkosti i Gazi, Vol. 1, No. 1, pp 51-60, 1966

37. James, R. M., "On the Remarkable Accuracy of Vortex Lattice Discretization in Thin Wing Theory", Rept. No. DAC 67211, McDonnell Douglas Corp., Feb. 1969

38. DeYoung, John, "Convergence - Proof of Discrete Panel Wing Loading Theories, AIAA J. Aircraft, Vol.-8, No. 10, Oct. 1971.

39. Durand, W. F. Editor-in-Chief, "Aerodynamic Theory", Vol. II, Dover Pub., Inc., 1963

40. Westwater, F. L., "The Rolling Up of the Surface of Discontinuity Behind an Aerofoil of Finite Span", ARC R&M No. 1962, Aug. 1935

41. Hackett, J. E. and Evans, M. R., "Vortex Wake Behind High-Lift Wings", J. Aircraft, Vol. 8, No. 5

42. Butter, D. J., and Hancock, G. J., "A Numerical Method for Calculating the Trailing Vortex System behind a Swept Wing at Low Speed", The Aero. J. of the RAS, Vol. 75, Aug. 1971

43. Wilson, J. D., "Real Time Development of the Wake of a Finite Wing", M. S. Thesis, West Virginia University, 1970

44. Jordan, P. F., "Span Loading and Formation of the Wake", AFOSR 70-2873 TR (RIAS TR 70-12c), Presented at AF-OSR-Boeing Symposium on Aircraft Wake Turbulence 1-3 Sept. 1970, Dec. 1970

45. El-Ramly, Z., "Aircraft Trailing Vortices; A Survey of the Problem", Rept. No. ME/A72-1, Carleton University, Ottawa, Canada, Nov. 1972

46. Hama, F. R. and Nutant, J., "Self-Induced Velocity on a Curved Vortex", Physics of Fluids, Vol. 4, No. 1, Jan. 1961

47. Hama, F. R., "Progressive Deformation of a Curved Vortex Filament by Its Own Induction", Phys. Of Fluids, Vol. 5, No. 10, October 1962

48. Hama, F. R., "Progressive Deformation of a Perturbed Line Vortex Filament", Phys. of Fluids, Vol. 6, No. 4 April 1963

49. Arms, R. J., and Hama, F. R., "Localized Induction Concept on a Curved Vortex and Motion of an Elliptic Vortex Ring", Phys.

of Fluids, Vol. 8, No. 4, April 1965

50. Betz, A., "Behavior of Vortex Systems", NACA TM 713, June 1933

51. Geising, J. P., "Vorticity and Kutta Condition for Unsteady Multi-Energy Flows", ASME, Applied Mechanics Western Conference, August 25-27, 1969, Paper 69-A PMW-19

52. Abbott, I. H., and VonDoenhoff, A. E., "Theory of Wing Sections", Dover Publications, Inc., New York, 1959

53. Rudhman, W. E., "A Numerical Solution to the Unsteady Airfoil with Application to the Vortex Interaction Problem", M.S. Thesis, The Pennsylvania State University, Dec. 1970

54. Von Karman, T., "Aerodynamics: Selected Topics in the Light of Their Historical Development", Cornell University Press, 1957

55. Johnson, W., and Scully, M. P., "Aerodynamic Problems in the Calculation of Helicopter Airloads", Symposium on Status of Testing and Model Techniques for V/STOL Aircraft, Mideast Region, American Helicopter Society, Oct. 26-27, 1972

Appendix A

Determination of the Numerical Expressions for Force and Induced Power on a Lifting Surface Element

Classical subsonic aerodynamic theory assumes the disturbance motion produced in a fluid by the passage of a lifting surface to be an irrotational motion. The fluid is assumed to be incompressible and inviscid. At a point, $\underline{x}$, on the lifting surface the pressure difference across the surface at the instant of time, t, is determined to be

$$\frac{\Delta p(\underline{x},t)}{\rho} = V(\underline{x},t)\ \gamma(\underline{x},t) + \frac{\partial}{\partial t}\left[\Delta\phi(\underline{x},t)\right] \qquad \text{A1}$$

from the unsteady Bernoulli equation. Δp is the pressure difference across the lifting surface, γ is the net distributed vorticity on the lifting surface and $\partial\Delta\phi/\partial t$ is the time rate of change of the potential difference across the lifting surface, all at the point, $\underline{x}$, of the lifting surface at the instant of time, t. The force exerted on an element of the lifting surface area, dS' is thus

$$\frac{d\underline{F}(\underline{x},t)}{\rho} = \frac{\Delta p}{\rho}(\underline{x},t)\ \underline{n}(x)dS$$

$$= \underline{V}(\underline{x},t)\ x\ \gamma(\underline{x},t)\ dS + \frac{\partial}{\partial t}\left[\Delta\phi(\underline{x},t)\right]\ \underline{n}(\underline{x})\ dS' \qquad \text{A2}$$

The power, dP_i required to sustain this force is just

$$\frac{dP_i}{\rho} = (\underline{x},t) = \underline{V}_R(\underline{x},t) \cdot \frac{d\underline{F}(\underline{x},t)}{P} \qquad \text{A3}$$

$$= \underline{V}_R(\underline{x},t) \cdot [\underline{V}(\underline{x},t) \times \gamma(\underline{x},t)\, dS] + \underline{V}_R \cdot [\frac{\partial}{\partial t}[\Delta\phi(\underline{x},t)\, \underline{n}(\underline{x})\, dS]$$

where $\underline{V}_R$ is the resultant velocity of the point on the lifting surface relative to the fluid. On a finite segment of the lifting surface, A_{il}, the force and power are given by

$$\frac{\underline{F}_{il}}{\rho}(t) = \iint_{A_{il}} [\underline{V}(\underline{x},t) \times \gamma(\underline{x},t)\, dS + \frac{\partial}{\partial t}[\Delta\phi(\underline{x},t)\, \underline{n}(\underline{x})\, dS]$$

$$\frac{P_{il}(t)}{\rho} = \iint_{A_{il}} \underline{V}_R(\underline{x},t) \cdot [\underline{V}(\underline{x},t) \times \gamma(\underline{x},t) dS + \frac{\partial}{\partial t}[\Delta\phi(\underline{x},t)]$$

$$\underline{n}(\underline{x})\, dS'] \qquad \text{A4}$$

Now, $\underline{\gamma} dS' = \underline{\Gamma} dl$ by Stokes theorem so that the quasi-static terms become

$$\iint_{A_{il}} \underline{V}(\underline{x},t) \times \gamma(\underline{x},t) dS = \int_{l_{il}} \underline{V}(\underline{x},t) \times \underline{\Gamma}(\underline{x},t) dl \qquad \text{A5}$$

$$\iint_{A_{il}} \underline{V}_R(\underline{x},t) \cdot [\underline{V}(\underline{x},t) \times \gamma(\underline{x},t) dS'] = \int_{l_{il}} \underline{V}_R(\underline{x},t) \cdot [\underline{V}(\underline{x},t)$$

$$\times \underline{\Gamma}(\underline{x},t) dl] \qquad \text{A6}$$

where l_{il} is the length of the vortex elements on A_{il}. If S_{il} contains a rectangular horseshoe vortex configuration with three arms,

$$\int_{l_{il}} \underline{V}(\underline{x},t) \times \underline{\Gamma}(\underline{x},t)dl \tilde{=} \sum_{m=1}^{3} [\underline{V}_m \times \underline{\Gamma l})_m]_{il} \qquad A7$$

$$\int_{l_{il}} \underline{V}_R(\underline{x},t) \cdot [\underline{V}(\underline{x},t) \times \underline{\Gamma}(\underline{x},t)dl] \tilde{=} \sum_{m=1}^{3} \underline{V}_{R_m} \cdot [\underline{V}_m \times \underline{\Gamma l})_m]_{il} \qquad A8$$

where $\underline{V}_m$, $\underline{V}_{R_m}$ are determined at the midpoints of the finite length segments $(l_m)_{il}$ which lie on S_{il}.

The unsteady contributions can be approximated by assuming S_{il} to be small. Then

$$\iint_{A_{il}} \underline{n}(\underline{x}) \frac{\partial}{\partial t} \Delta\phi\ (\underline{x},t)dS \tilde{=} \overline{\underline{n} \frac{\partial \Delta\phi}{\partial t}} S_{il} \qquad A9$$

$$\iint_{A_{il}} \underline{V}_R(\underline{x},t) \cdot \underline{n}\ (\underline{x}) \frac{\partial \Delta\phi}{\partial t}\ (\underline{x},t)dS' \tilde{=} \overline{\underline{V}_R \cdot \underline{n} \frac{\partial \Delta\phi}{\partial t}} S_{il}$$

$$= \overline{V_{R_n} \frac{\partial \Delta\phi}{\partial t}} S_{il} \qquad A10$$

where $\overline{\underline{n}\ \partial\Delta\phi/\partial t}$, $\overline{V_{R_n}\ \partial\Delta\phi/\partial t}$ are average values over S_{il}. Since $\partial\Delta\phi/\partial t$ is constant over the area bounded by the horseshoe vortex segment and the area S_{il} is taken to be flat plate segment of the lifting surface so that its spatial orientation is defined

by the unit normal at the control point, $\underline{X}_{cil}$, located on the segment

$$\overline{\underline{n}\,\frac{\partial\Delta\phi}{\partial t}} = \underline{n}(\underline{x}_{cil})\,\frac{\partial\Delta\phi}{\partial t}\,(\underline{x}_{cil},\,t) \qquad \text{A11}$$

$$V_{Rn}\,\frac{\partial\Delta\phi}{\partial t} = V_{Rn}\,(\underline{x}_{cil},\,t)\,\frac{\partial\Delta\phi}{\partial t}\,(\underline{x}_{cil},\,t) \qquad \text{A12}$$

where $\underline{n}\,(\underline{x}_{cil})$ is the unit normal at the control point, $\underline{x}_{cil}$, where the boundary condition is satisfied numerically on S_{il} and $V_{Rn}\,(\underline{x}_{cil},\,t)$ is the normal component of the resultant velocity of A_{il} relative to the fluid, i. e., the component of the resultant velocity in the direction of the unsteady force.

Utilizing equations (A7), (A8), (A9) and (A10) the unsteady force and power associated with the segment of lifting surface, A_{il}, can be determined from

$$\frac{\underline{F}_{il}(t)}{\rho} = \sum_{m=1}^{3} [\underline{V}_m \times (\underline{\Gamma}_1)_m]_{il} + \underline{n}(\underline{x}_{cil})\,\frac{\partial\Delta\phi}{\partial t}\,(\underline{x}_{cil},\,t)\,S_{il} \qquad \text{A13}$$

$$\frac{P_{il}(t)}{\rho} = \sum_{m=1}^{3} \underline{V}_{R_m} \cdot [\underline{V}_m \times (\underline{\Gamma}_1)_m]_{il} + V_{Rn}(\underline{x}_{cil},\,t)\,\frac{\partial\Delta\phi}{\partial t}\,(\underline{x}cil,\,t)\,S_{il} \qquad \text{A14}$$

$\underline{n}(\underline{x}_{cil})$ is the unit normal at $\underline{x}_{cil}$ on S_{il} and the average unsteady pressure $\partial\Delta\phi/\partial t$ on S_{il} is obtained from equation (31). $V_{Rn}(\underline{x}_{cil},\,t)$ is determined from

$$V_{Rn}\,(\underline{x}_{cil},\,t) = \underline{V}_R\,(\underline{x}_{cil},\,t)\cdot\underline{n}\,(\underline{x}_{cil})$$

Appendix B

Determination of Vortex Core Size for Numerical Modelling of Interaction Phenomena

Because the Biot-Savart law yields infinite velocities as a vortex filament is approached, the numerical application of this law can lead to unrealistically large velocities and displacements if the point at which the velocity is to be computed approaches too close to the inducing segment. Typical procedures in maintaining a realistic velocity field have been to assign a core radius to the filament segment at which the velocity is a maximum and within this core either no velocity exists or a simple solid body rotation is assumed. The proper selection of this core radius is an important consideration and in the past has been selected, variously, on continuity considerations, a physically plausible maximum induced velocity, and experience in terms of what works for the job at hand.

Selecting the radius based on a maximum allowable induced velocity is largely a question of experience. Sadler (29) has used this approach and has found this can lead to erroneous averages. A further drawback would seem to be in certain aeroelastic and acoustic applications in which the high harmonics might be important and would be noticably affected by such a velocity cutoff.

Another method of estimating the core radius which has not yet been tried is to limit the displacement allowed any point under

the induced field of a single segment. Such a limit could be any reasonable physical dimension of the system, say a wing span, propeller radius, chord, etc. Suppose the maximum interaction displacement is Γ_{max}. Then

$$\Gamma_{max} = v_{imax} \Delta t \qquad \text{B1}$$

where V_{imax} = max. allowable induced velocity

Δt = Time step of the motion.

Close to the filament $V_{imax} = \Gamma/2\pi h_c$ and, for propellers, $\Delta t = \Delta\psi/\omega$ where ω is the propeller rotational speed and $\Delta\psi$ the azimuth travel in the time step, Δt. Therefore

$$h_c = \frac{\Gamma}{2\pi} \frac{\Delta\psi}{V_{max}\omega} \qquad \text{B2}$$

If $\Gamma_{max} \sim R$, the propeller radius,

$$h_c \sim \frac{\Gamma\Delta\psi^{o}}{V_T\ 360} \qquad \text{B3}$$

where, for an estimate, Γ could be taken as the maximum Γ on the propeller blade. Going a step further

$$\Gamma = \frac{V}{2} cc_l \sim \frac{V_T}{2} c\bar{C}_L = \frac{V_T}{2} c \frac{6C_T}{\sigma}$$

in hover. Thus the core radius can be estimated from

$$h_c \sim c\left(\frac{C_T}{\sigma}\right) \frac{\Delta\psi^{o}}{120} \qquad \text{B4}$$

As an example, suppose a propeller generates a $\Gamma = 50$ ft.^{2}/sec. at a $V_T = 600$ ft./sec. Then, for $\Delta\psi = 15^0$, $h_c = 0.00347$ ft. and $\Delta\psi = 3^0$ gives $h_c = 0.00069$ ft., both on the order of .001 ft.

For a finite wing, a corresponding dimension to limit the interaction displacement is the semi-span, b/2.

Hence $$h_c = \frac{\Gamma \Delta t}{\pi b} \qquad \text{B5}$$

Then $$\Delta t = c/v$$

$$h_c = \frac{\Gamma}{\pi v(\frac{b}{c})} = \frac{\Gamma}{\pi VAR} \qquad \text{B6}$$

so that $$h_c = \frac{cc_l}{\pi AR} \qquad \text{B7}$$

gives a reasonable estimate. It can be noticed here that the desired core radius is proportional to the induced angle of attack.

Finally, it should be restated that other suitable physical dimensions could be used. Based on results of the present analysis a distance as small as the trailing edge boundary layer thickness might be required.

Appendix C

A Method to Determine Wake Induced Velocities at a Bound Vortex Load Point Knowing the Velocities at the Control Point on the Same Panel.

The major criticism of the vortex lattice model developed in the main body of this text is the inordinate amount of computer time required to perform the numerical integration over the wake to generate the wake induced velocities first at the control points in order to satisfy the boundary condition and then at the load points (bound vortex midpoints) to obtain the load distribution. A method has been recently conceived to eliminate one of these integrations by utilizing the fact that the relative geometry between load points and control points on a panel is fixed. This means that each contribution to the velocity field at one set of points due to a given vortex element need only be modified by a correction factor to yield the velocities at another set of points; the correction factor is a function only of the relative geometry between the sets of points. The idea can be clearly illustrated in the two dimensional case.

Assume a flat plate airfoil has started impulsively from rest. The flat plate is assumed to be modelled by a single bound vortex at c/4 and a point of flow tangency at 3c/4. A deforming wake of shed vorticity exists behind the airfoil at any instant of time with the elements of shed vorticity having strength determined by the airfoil-wake configuration at the instant of shedding. The

strength of wake vorticity is thus expressable as a function of the wake coordinate, s. Referring to Sketch 1, the x- and z- induced velocity components at the control point and the bound vortex due to the wake can be easily determined.

Sketch 1

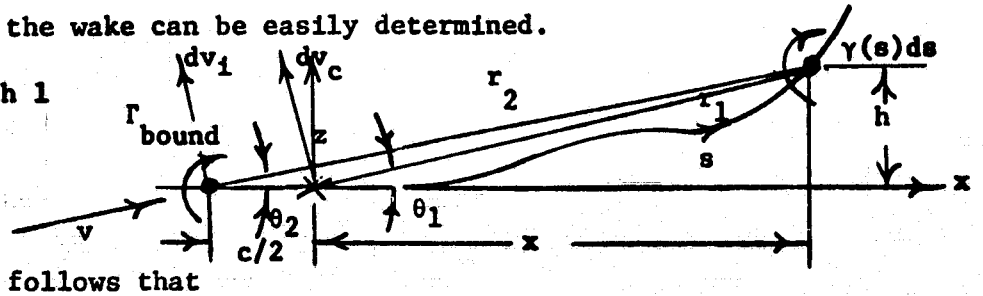

It follows that

$$V_{cx} = -\int_0^1 \frac{\gamma(s)ds \sin\theta_1}{2\pi r_1(s)} = -\int_0^1 \frac{\gamma(s)ds\, h(s)}{2\pi r_1^2(s)} \tilde{=} -\sum_0^1 \frac{h(si)\,\Gamma(s_i)}{2\pi r_1^2(s_i)} \qquad C1$$

$$V_{ix} = -\int_0^1 \frac{\gamma(s)ds \sin\theta_2}{2\pi r_2(s)} = -\int_0^1 \frac{\gamma(s)ds\, h(s)}{2\pi r_2^2(s)} \tilde{=} -\sum_0^1 \frac{h(s_i)\,\Gamma(s_i)}{2\pi r_2^2(s_i)} \qquad C2$$

where $\sum_0^1$ is the numerical approximation to $\int_0^1$ and $\gamma(s_i) \tilde{=} \Gamma(s_i)/\Delta s$

It follows that

$$V_{ix} = -\int_0^1 \frac{h(s_i)\,\Gamma(s_i)}{2\pi r_1^2(s_i)} \frac{r_1^2(s_i)}{r_2^2(s_i)} = \sum_0^1 \Delta V_{cx} \frac{r_1^2(s_i)}{r_2^2(s_i)} \qquad C3$$

where ΔV_{cx} is the x- velocity increment at the control point due to the concentrated wake vortex $\Gamma(s_i)$ located at $X(s_i)$, $h(s_i)$.

Similarly the z- component can be obtained as

$$V_{cz} = \int_0^1 \frac{\gamma(s)ds \cos\theta_1}{2\pi r_1(s)} = \int_0^1 \frac{\gamma(s)ds\, x}{2\pi r_1^2(s)} \tilde{=} \sum_0^1 \frac{Xi\,\Gamma(s_i)}{2\pi r_1^2(s_i)} \qquad C4$$

$$V_{iz} = \int_0^1 \frac{\gamma(s)ds \cos\Theta_2}{2\pi r_2(s)} = \int_0^1 \frac{\gamma(s)ds\ (x+\frac{c}{2})}{2\pi r_2^2(s_i)} \cong \sum_0^1 \frac{(\frac{c}{2}+x_i)\ \Gamma(s_i)}{2\pi r_2^2(s_i)} \qquad C5$$

Then

$$V_{iz} = \sum_0^1 \frac{X_i\ \Gamma s_i}{2\pi r_1^2(s_i)} \frac{r_1^2(s_i)}{r_2^2(s_i)} (1+\frac{c}{2x_i}) = \sum_0^1 \Delta V_{cz} \frac{r_1^2(s_i)}{r_2^2(s_i)} (1+\frac{c}{2x_i}) \qquad C6$$

where ΔV_{cz} is the z- velocity increment at the control point. Since $r_2^2(si)/r_1^2(si) = 1 + (c/2r_1)^2 - 2(c/2r_1)\cos(\pi - \Theta_1)$ the induced velocity at the load point due to a wake vortex can be expressed in terms of the velocity induced at the control point by that vortex and the relative geometry (c/2) between the control point and the load point. It is easy to see the same type corrections apply if the flat plate is a segment of a two-dimensional airfoil except that c/2 is now a fraction of the segment chord. Further such procedures should be applicable to the three-dimensional case and finite length vortex filaments. From a computational standpoint, the major time consumption is involved with the calculation of the ΔV_{cx} , ΔV_{cz} by the Biot-Savart Law. In the vortex geometry of the present method there are three load points associated with each control point so that each wake is integrated across four times to obtain a compatible set of circulations and loads for a given geometry. The application of this correction factor procedure requires that this integration be done only once and should result in a considerable time saving.

Figures

Figure 1. **Bound Vortex and Control Point Geometry on One Spanwise Panel Divided into "Num-1" Chordwise Panels and "Num" Unknown Vortices.**

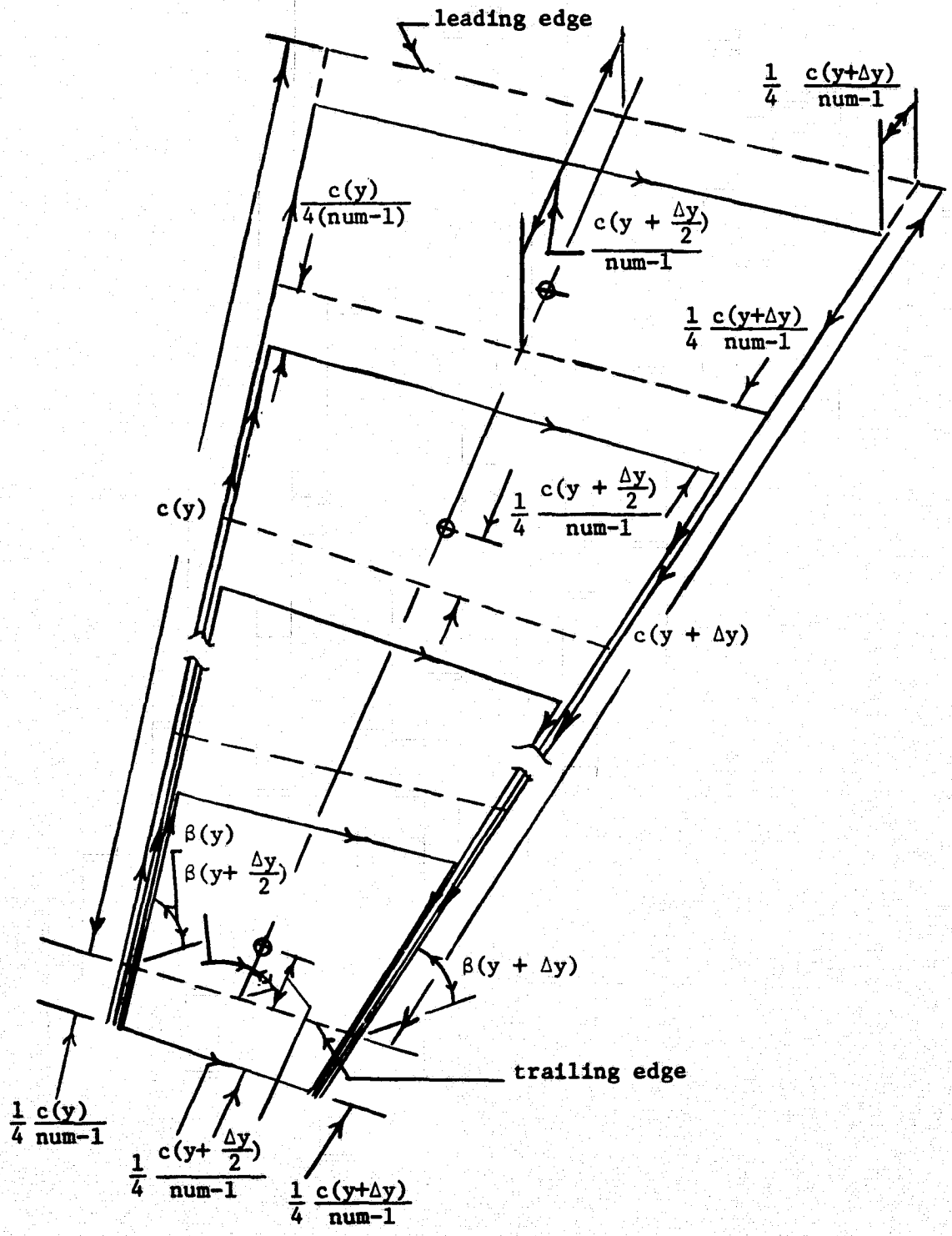

Figure 2. Propeller and Wing Coordinate Systems.

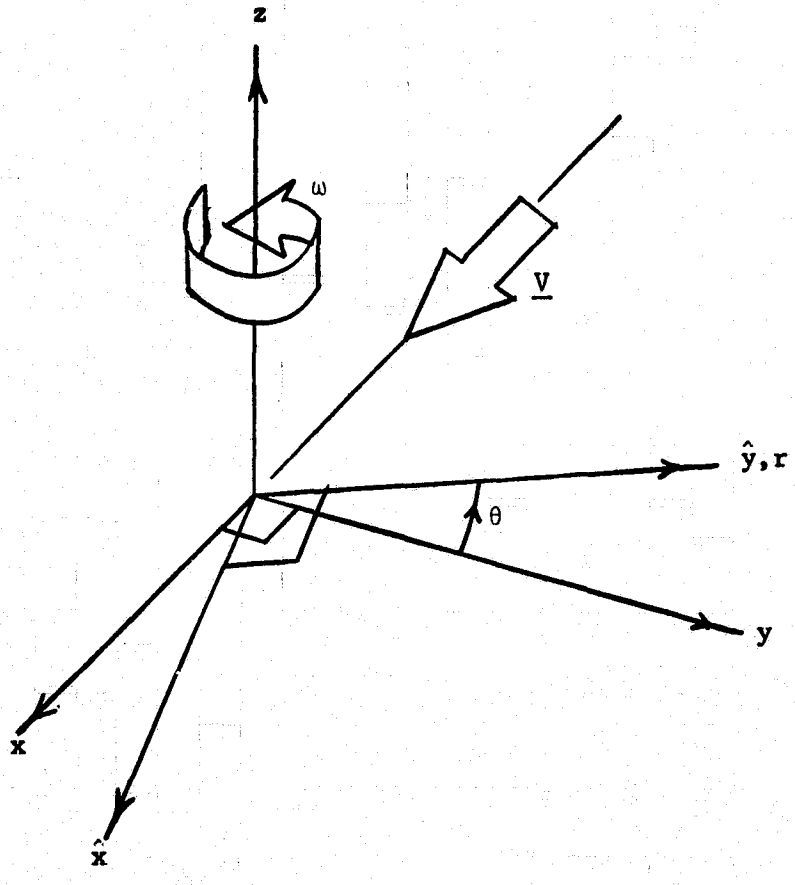

x,y,z ~ Inertial Reference

$\hat{x},\hat{y},z$ ~ Rotating Coordinate System

NOTE: $\hat{y} = r$, the propeller radial coordinate

Figure 3. Geometry of a Straight-Line Vortex Segment.

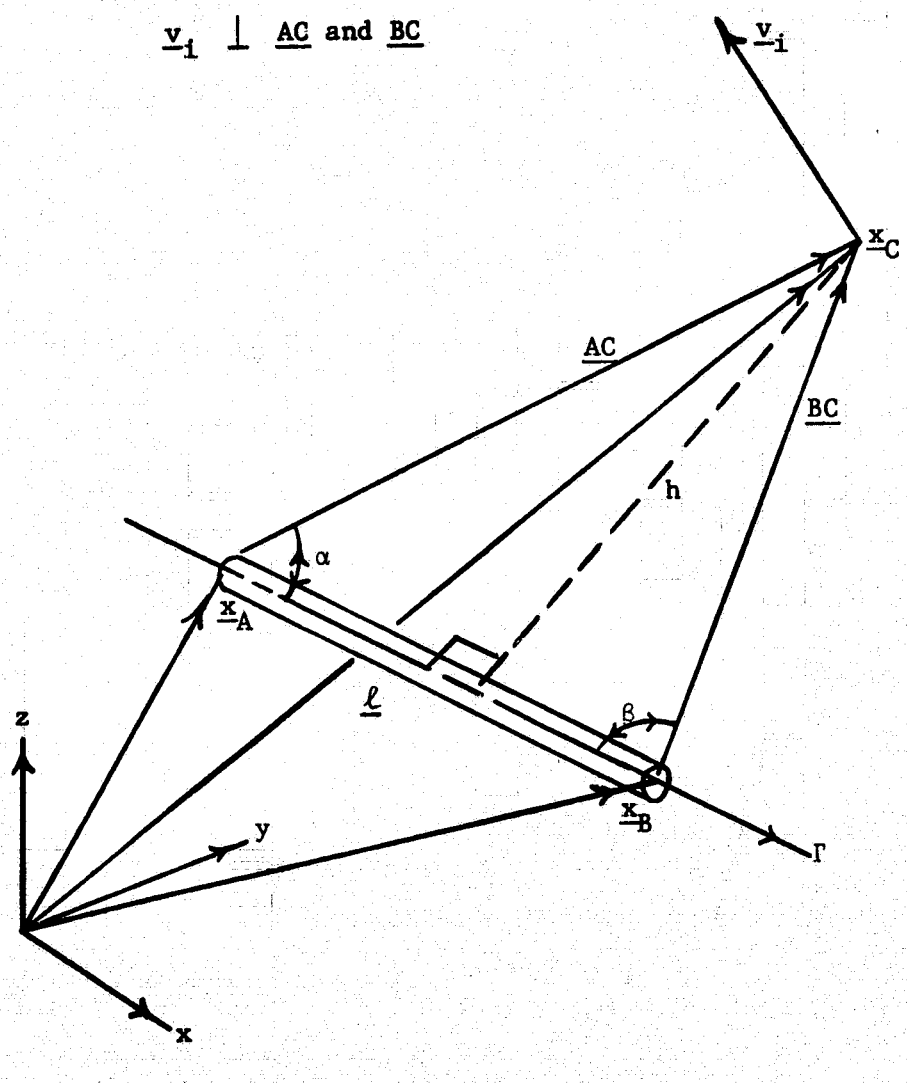

Figure 4. Index Convention for Blade Bound Vortices and Control Points

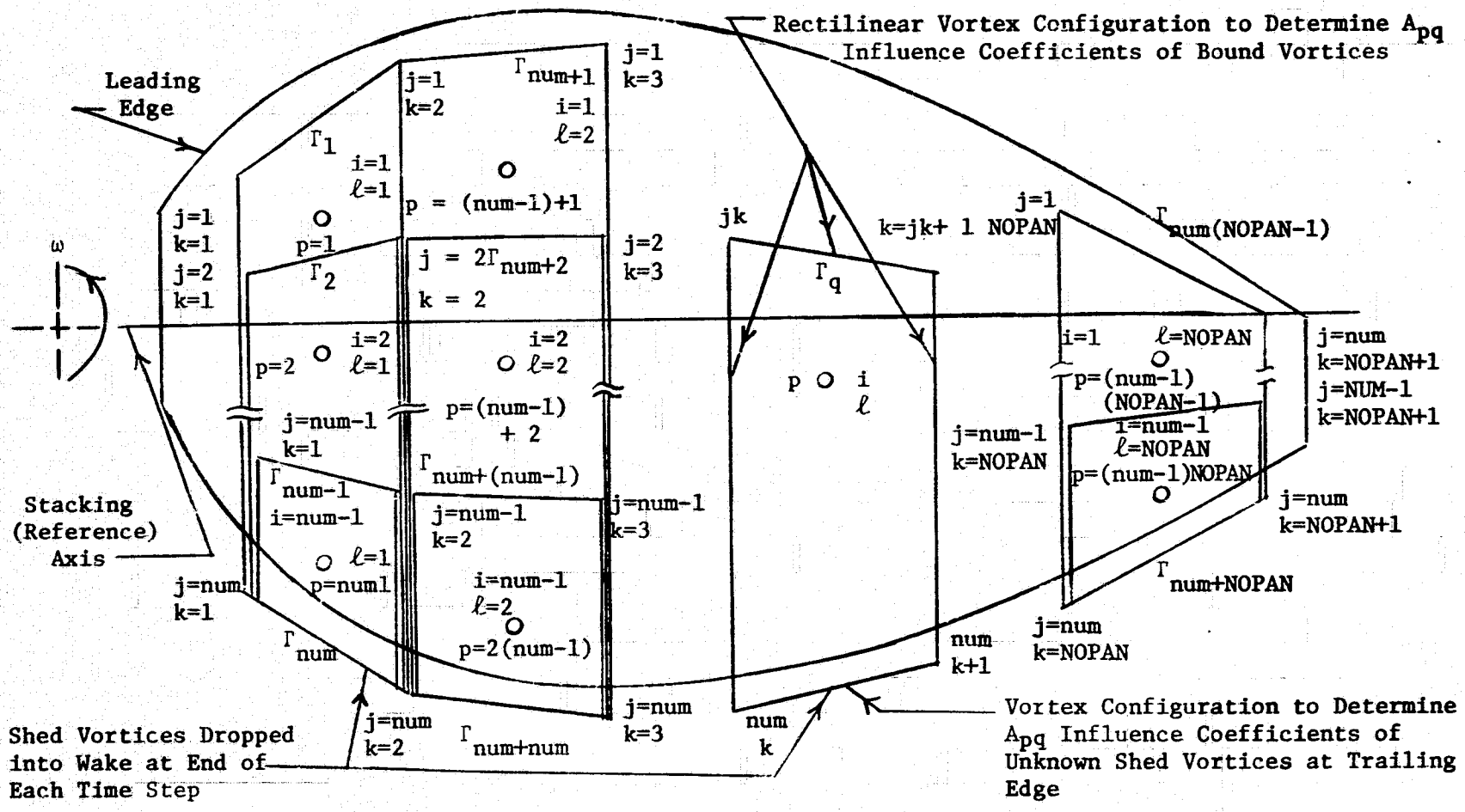

Figure 5. Geometry of Unit Normal at a Control Point.

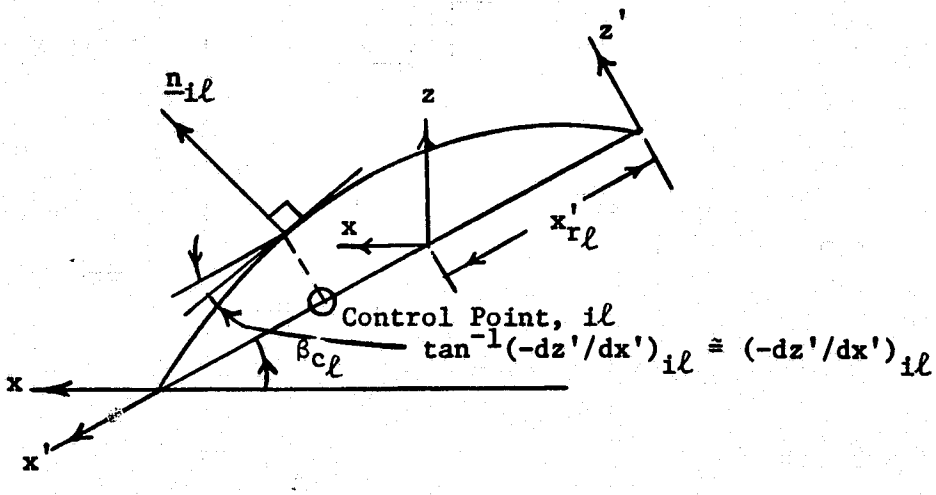

No Dihedral to Represent Radial Twist

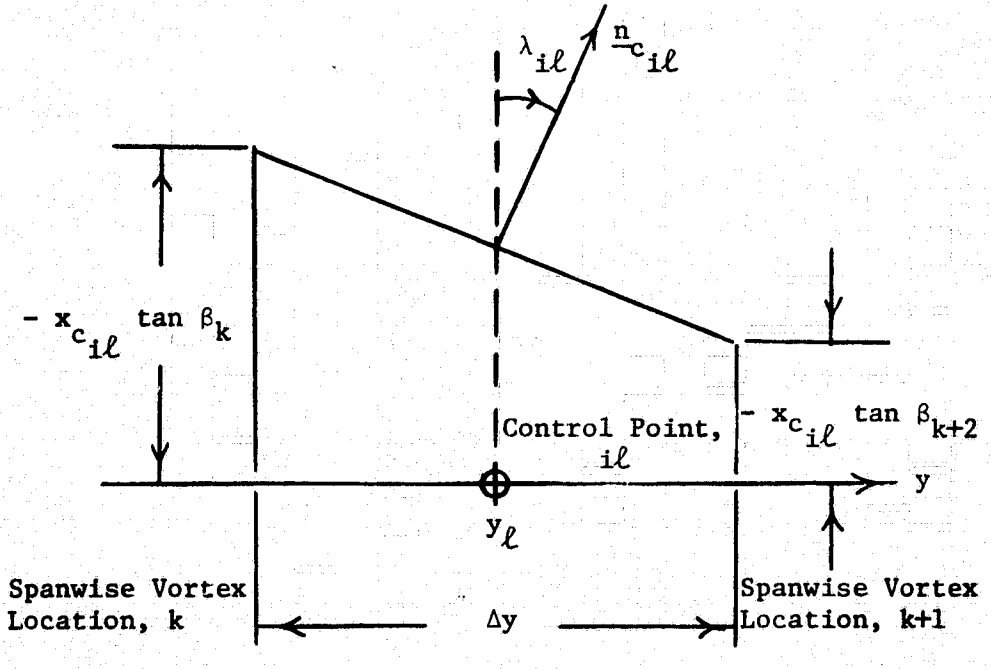

Local Dihedral at Control Point, $i\ell$

Figure 6. Details of Geometry and Circulation on a Trapezoidal Segment of the Lifting Surface.

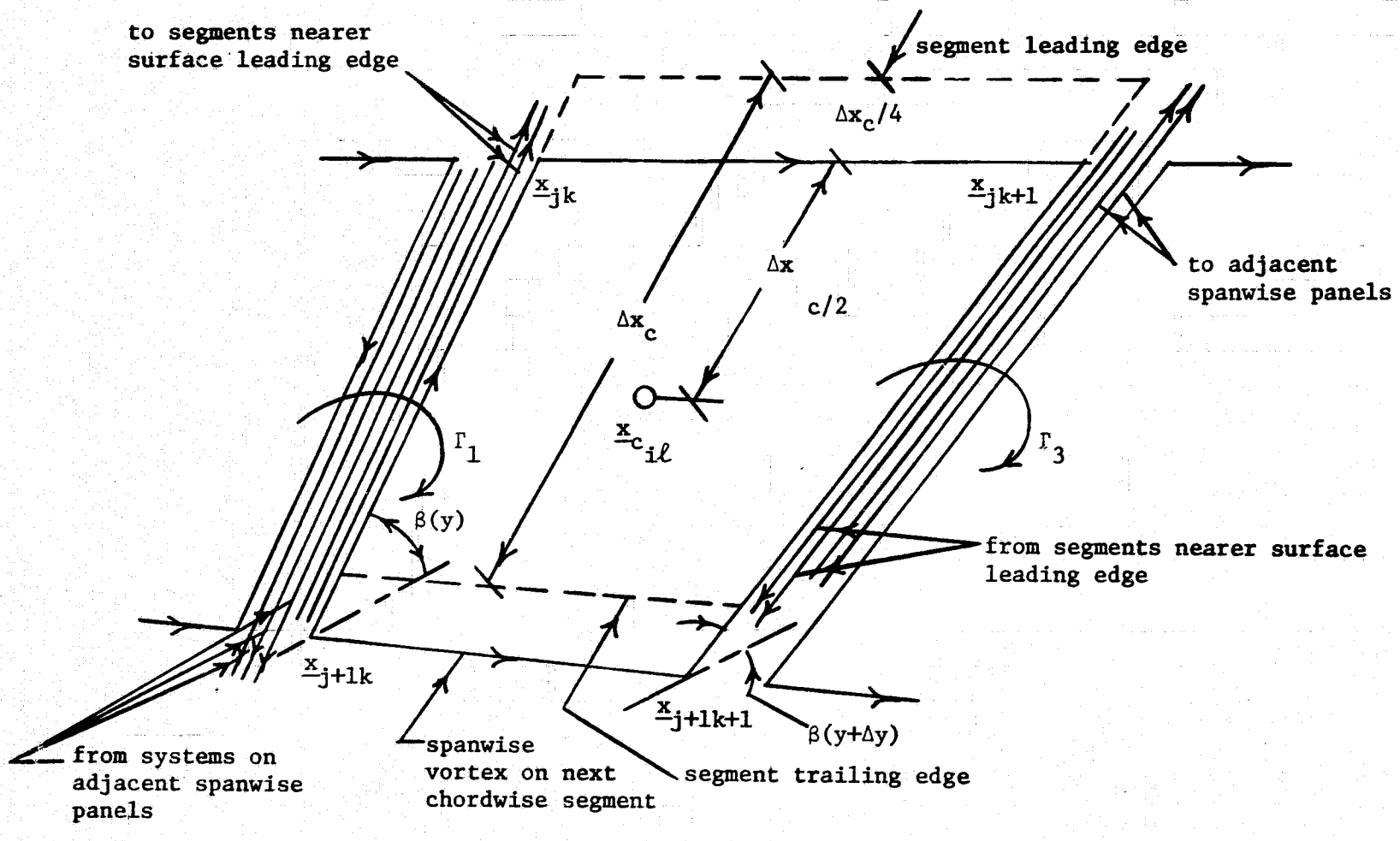

Figure 7. Flow and Force Geometry at Blade Radial Station.

Classical Steady Flow

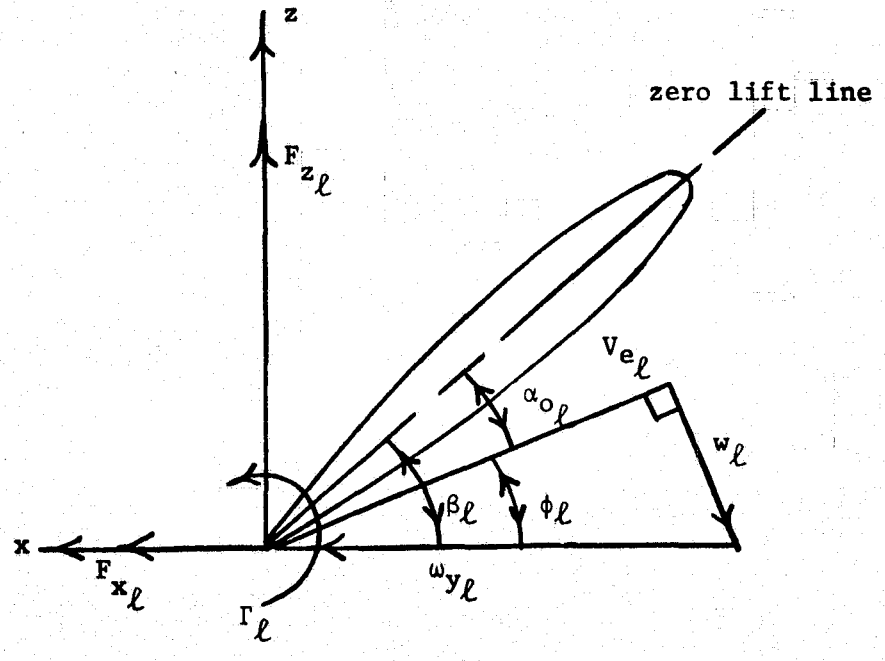

Figure 8. Comparison of Two Computation Systems for Vortex Lattice Computations.

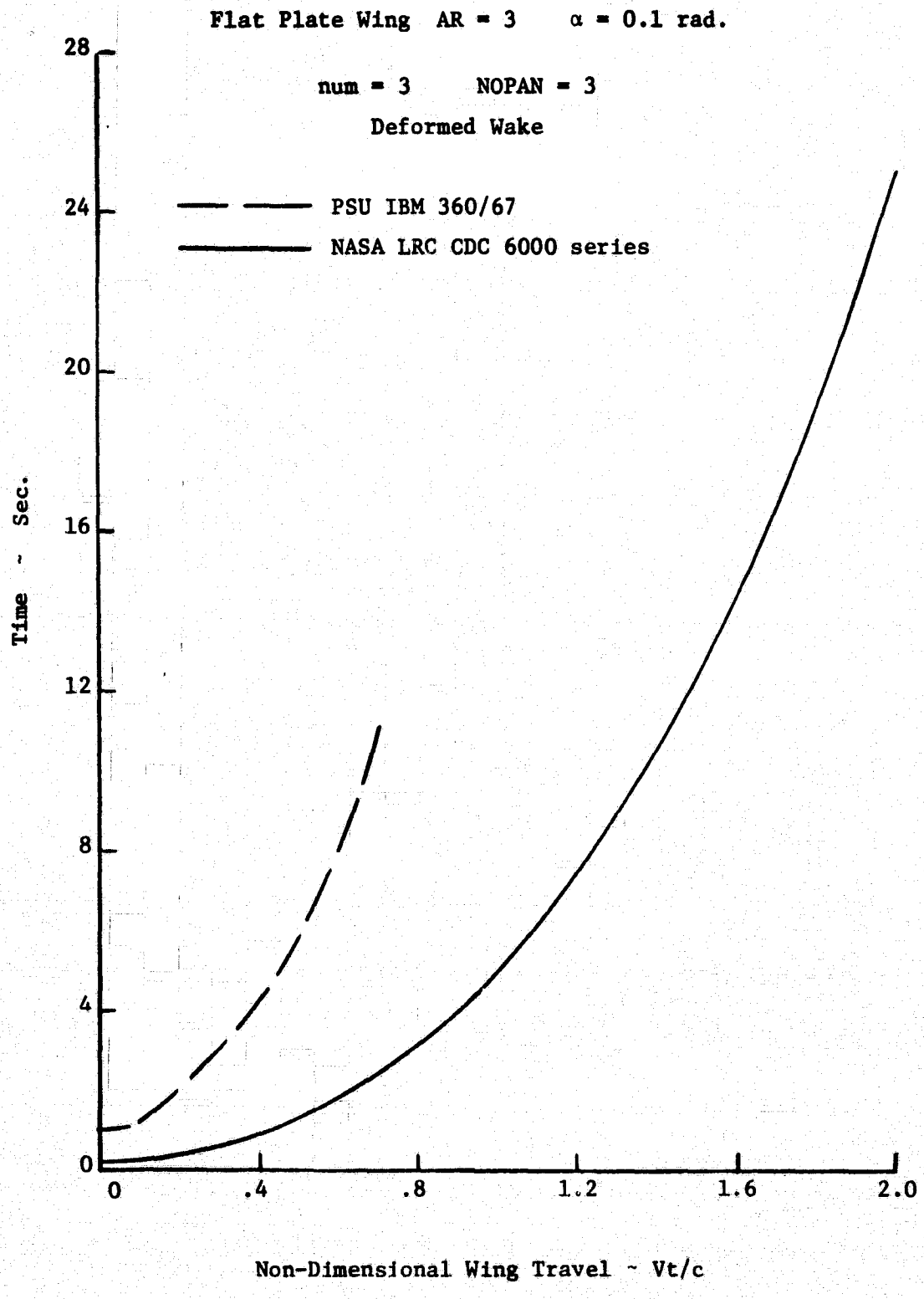

Figure 9. Effect of Orientation on Velocity Induced by a Straight Line Vortex Segment - h/ℓ Constant.

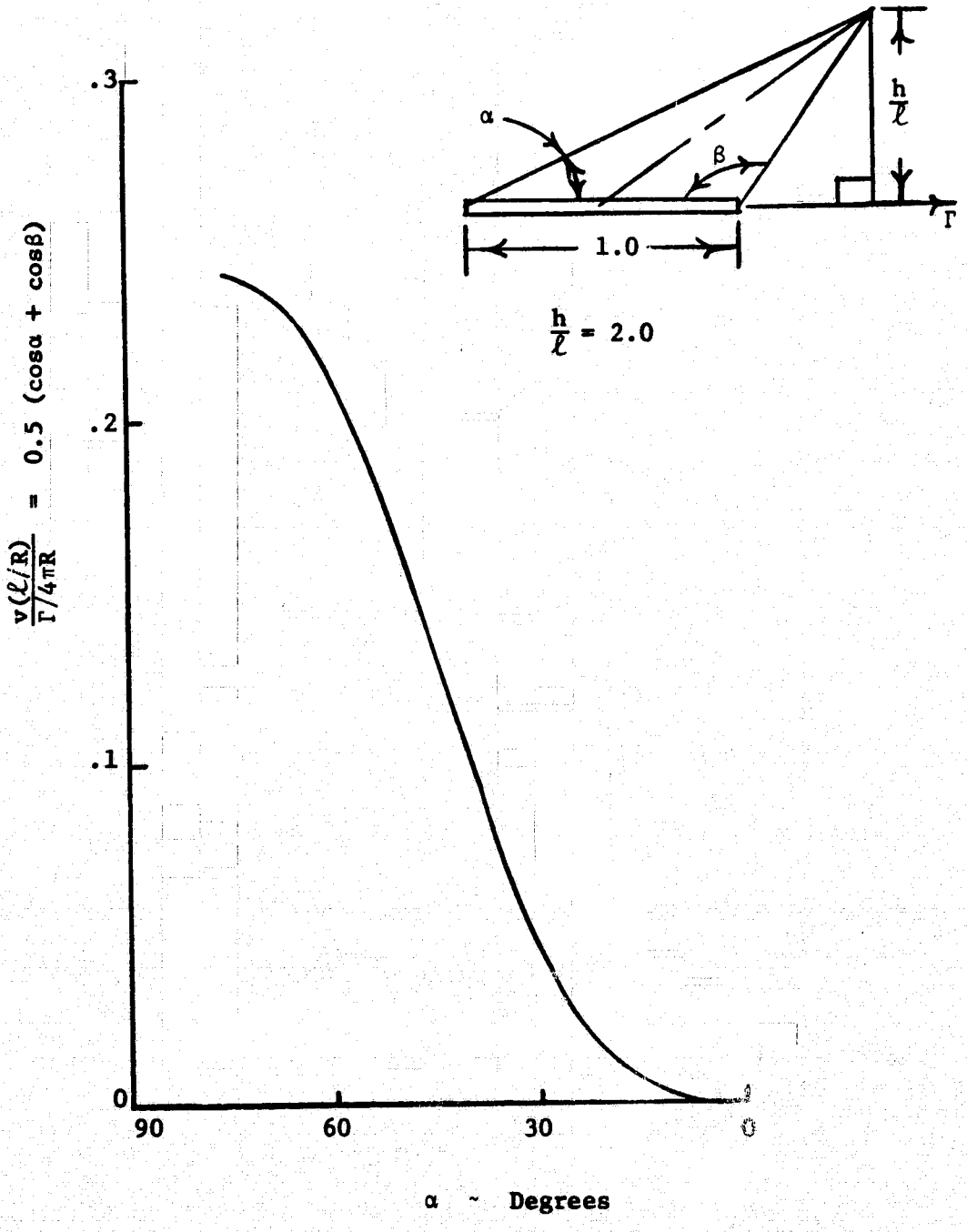

Figure 10. Effect of Orientation on Velocity Induced by a Straight Line Vortex Segment.

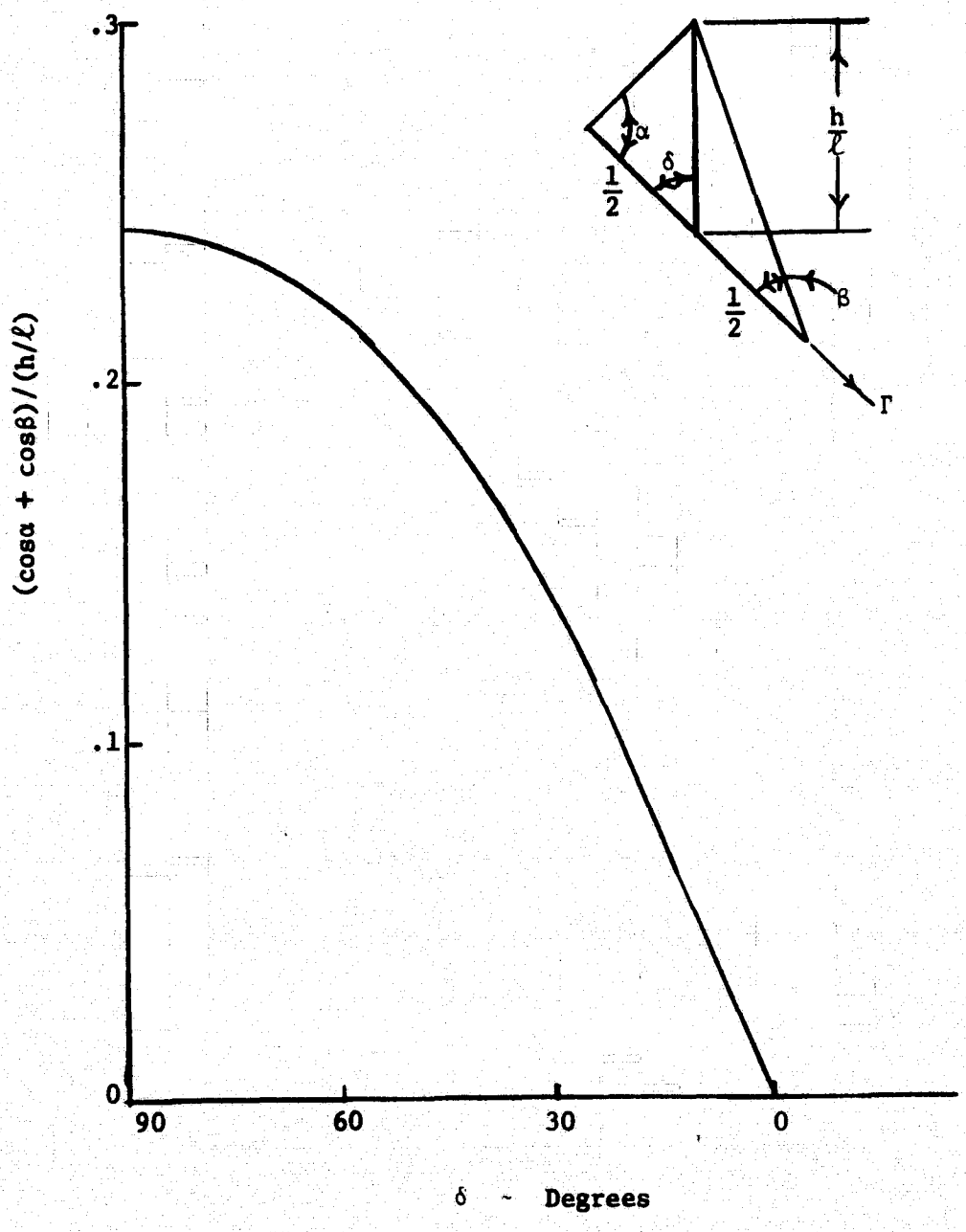

Figure 11. Correlation of Actual Vortex Segment Induced Velocity with Induced Velocity Based on Projected Length.

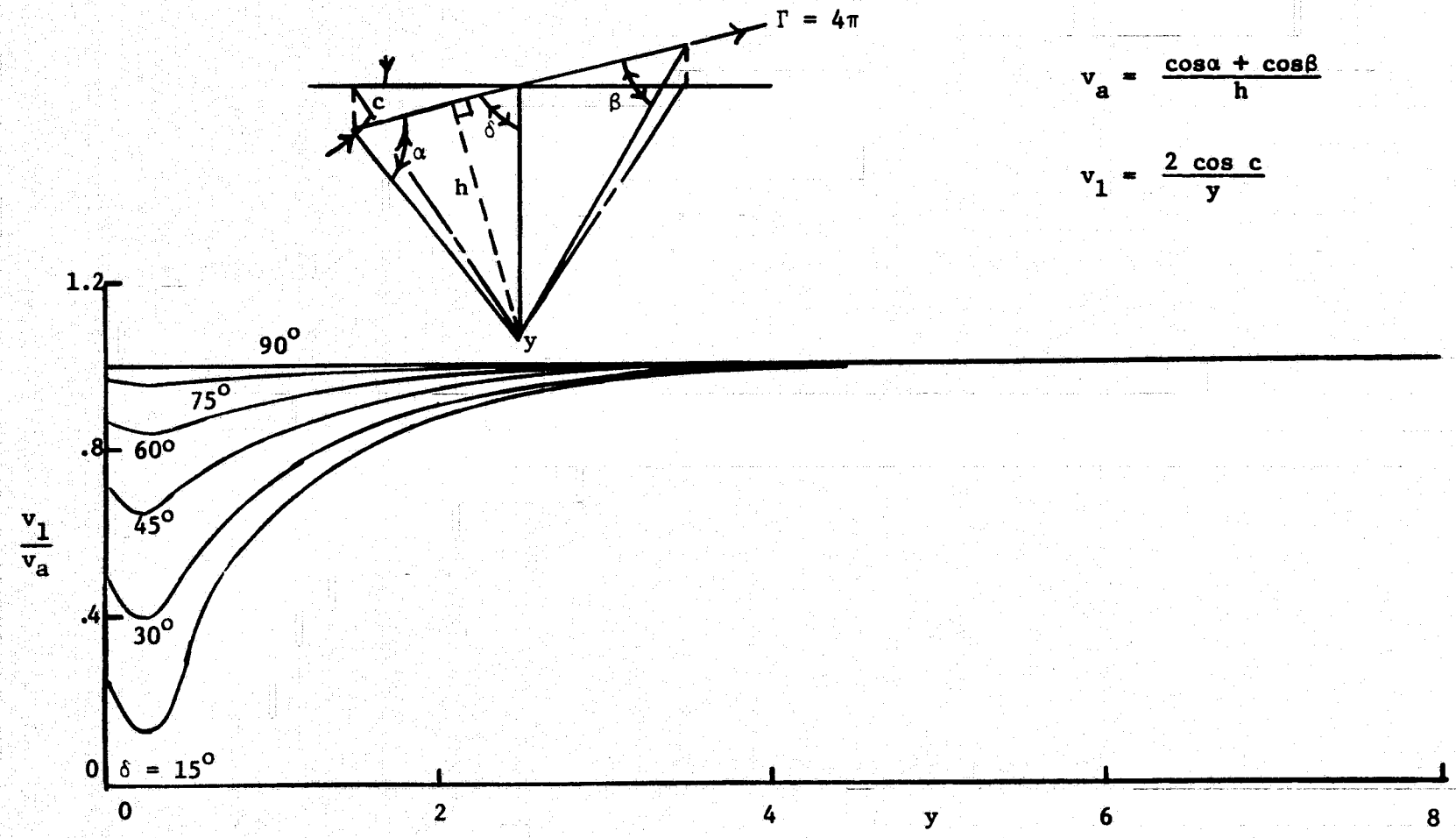

Figure 12. Variation of Velocity Induced at a Point by a Straight Line Vortex Segment.

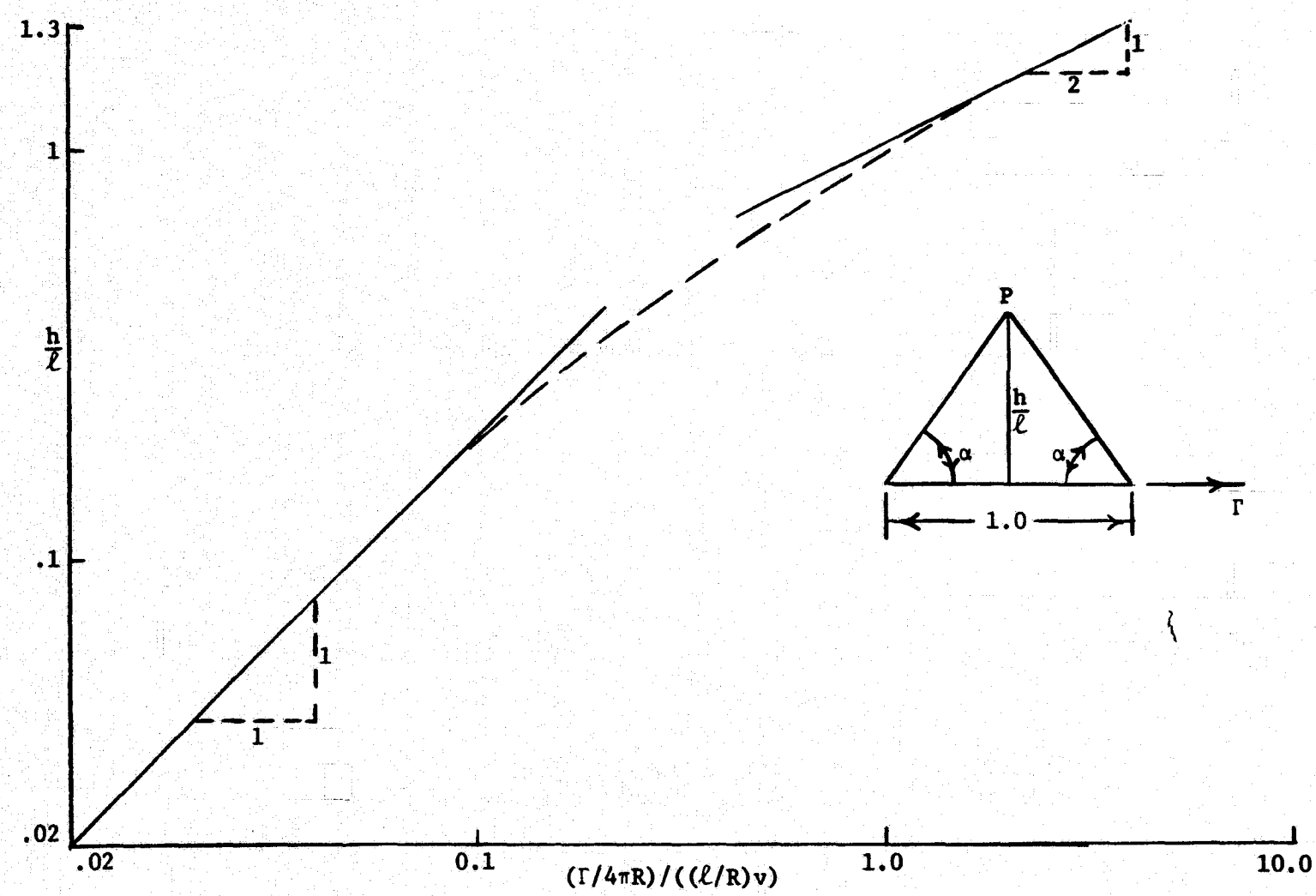

Figure 13. C_ℓ Growth Versus Wake Length Following an Impulsive Start.

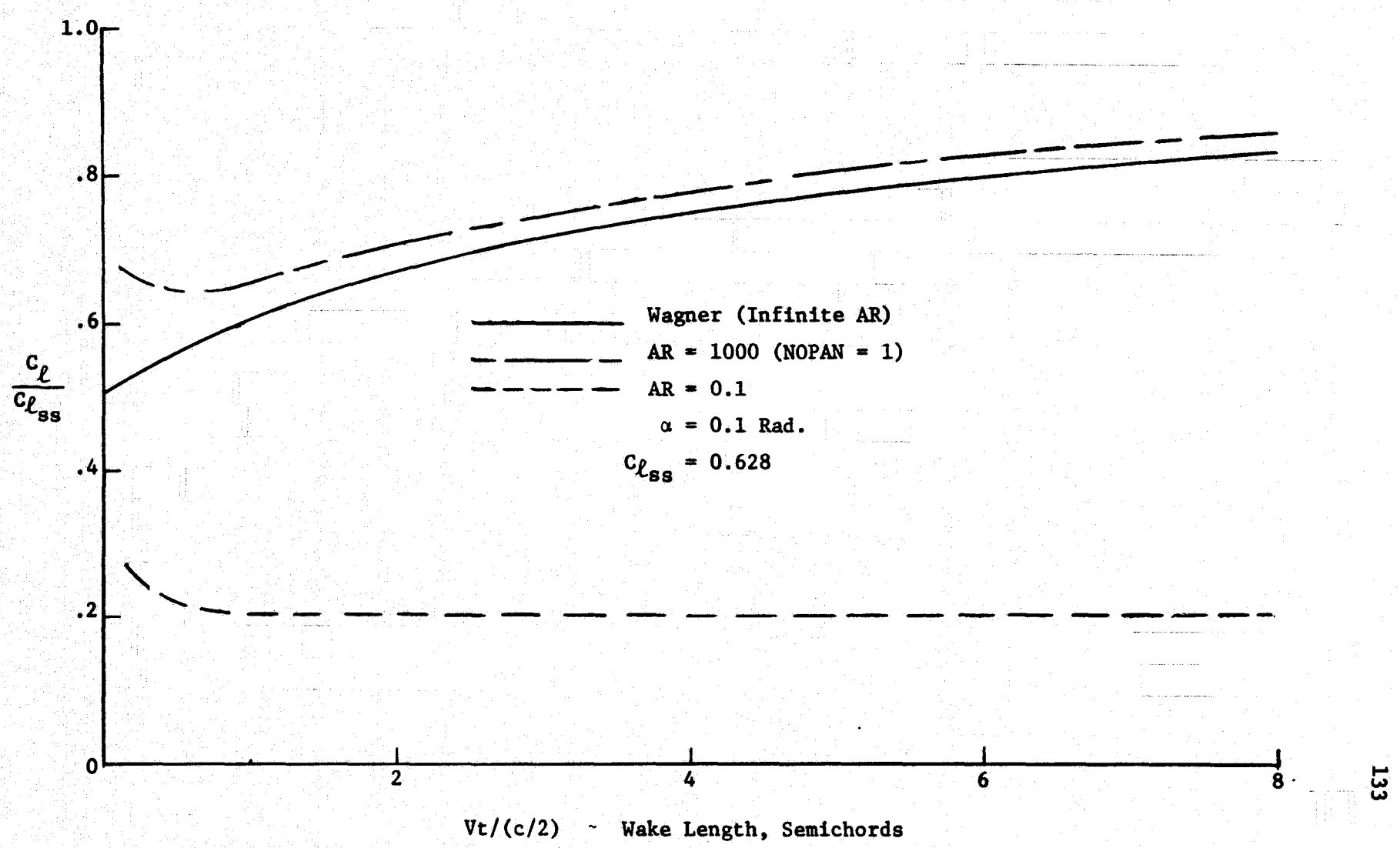

Figure 14. Effect of Time on Chordwise Pressure Distribution.

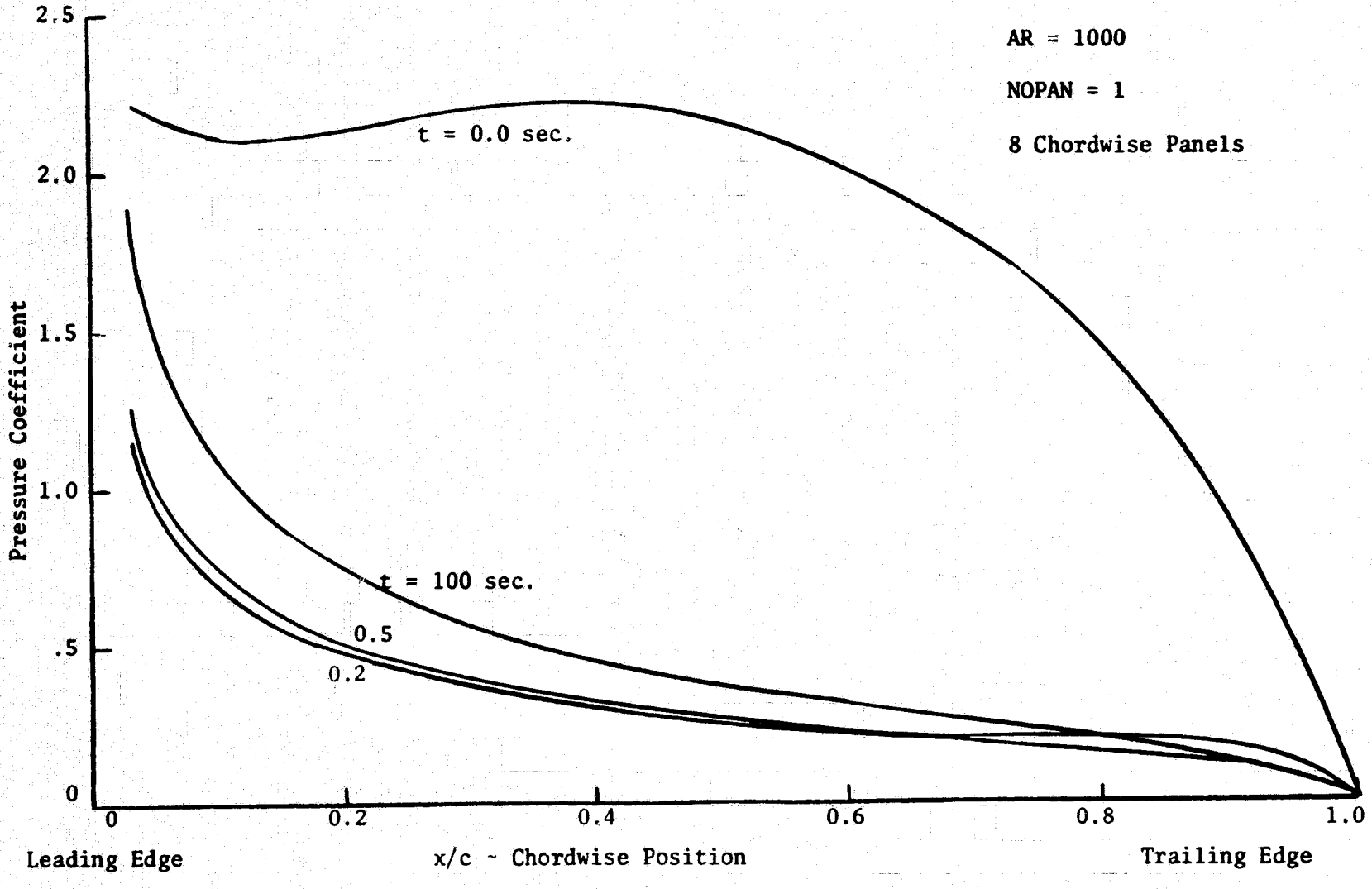

Figure 15. Effect of Number of Spanwise Panels on C_L.

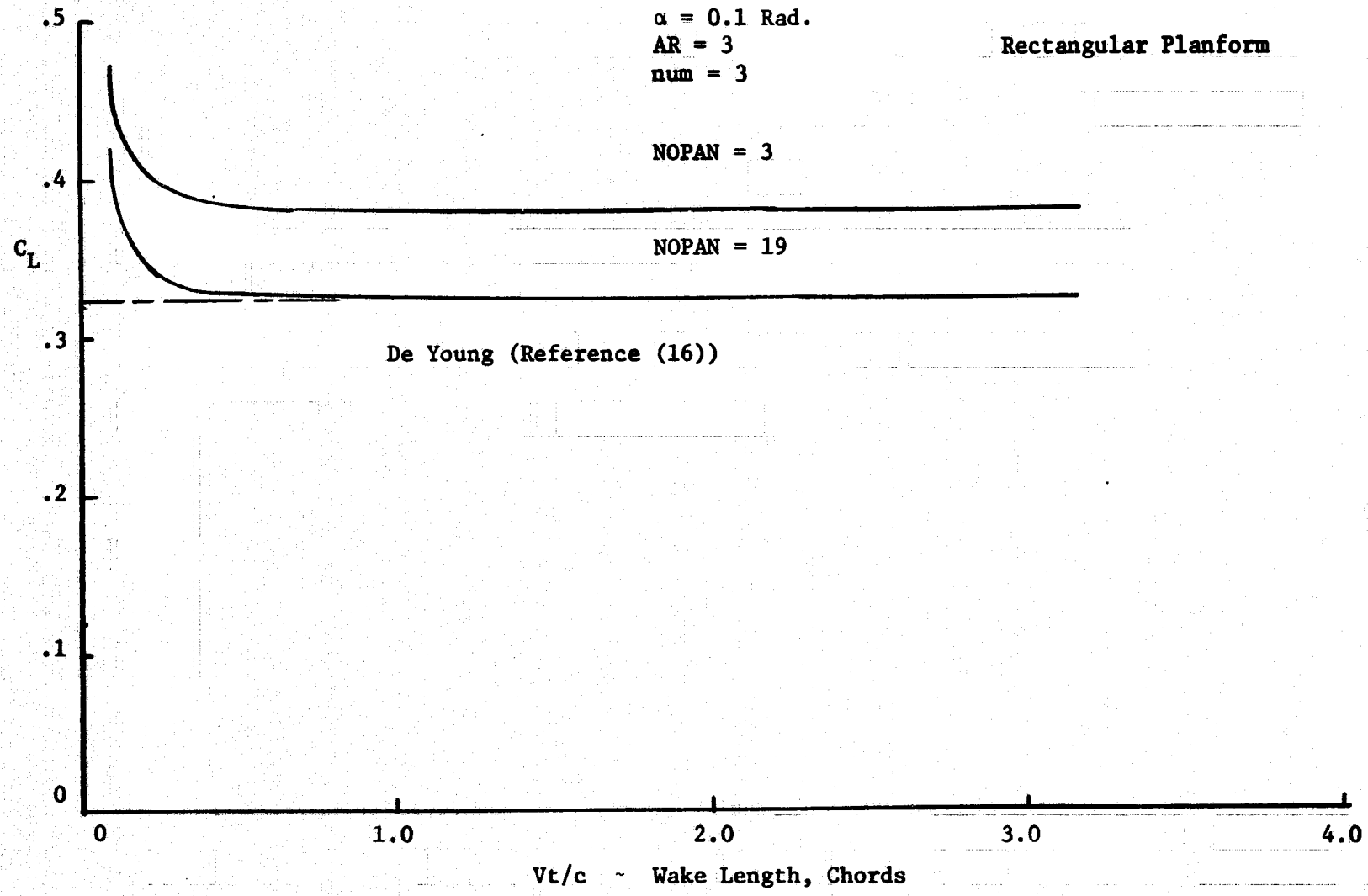

Figure 16. Effect of Number of Spanwise Panels on C_L.

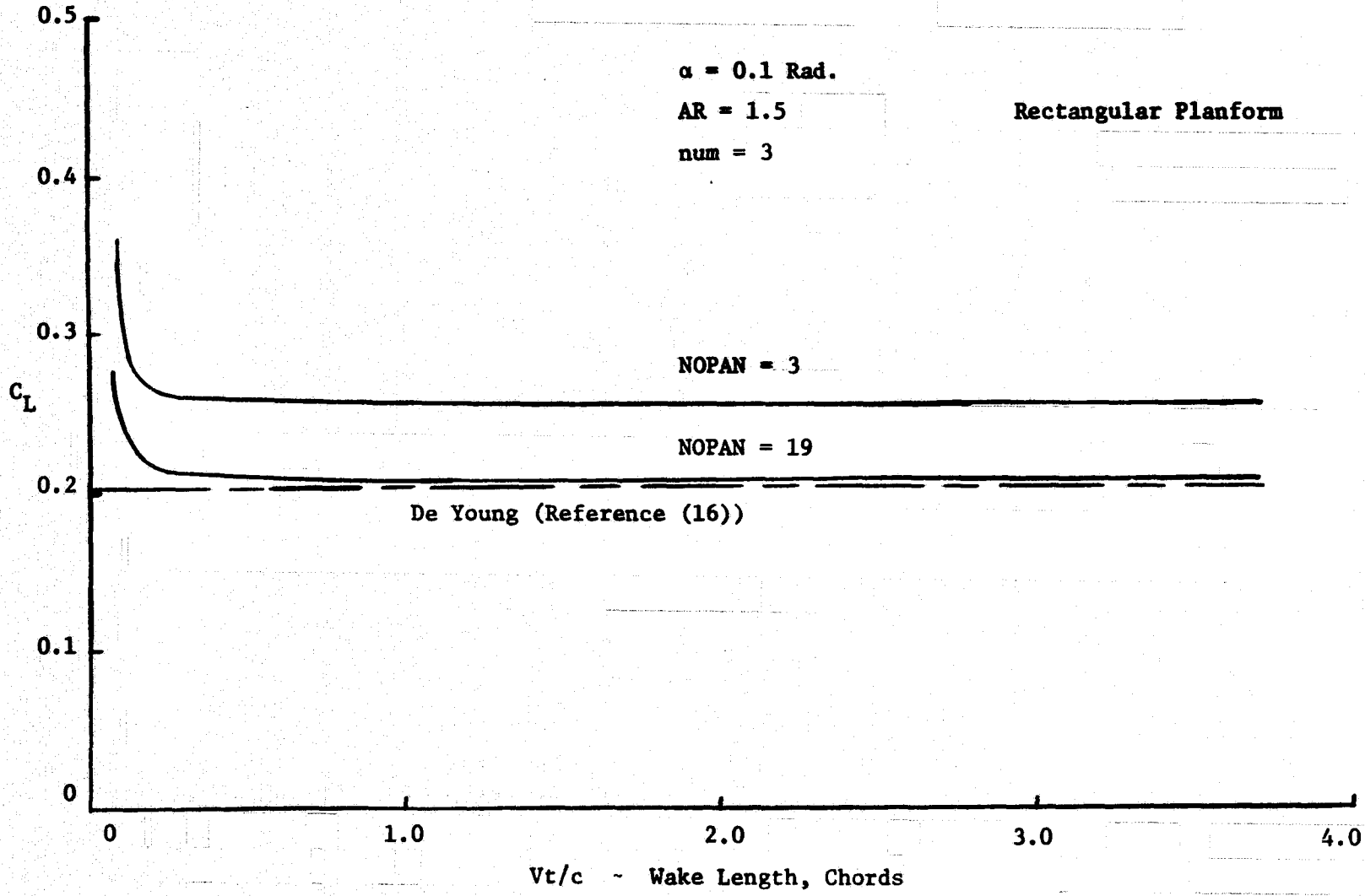

Figure 17. Effect of the Chordwise Distribution of Vorticity on Lift and Induced Drag.

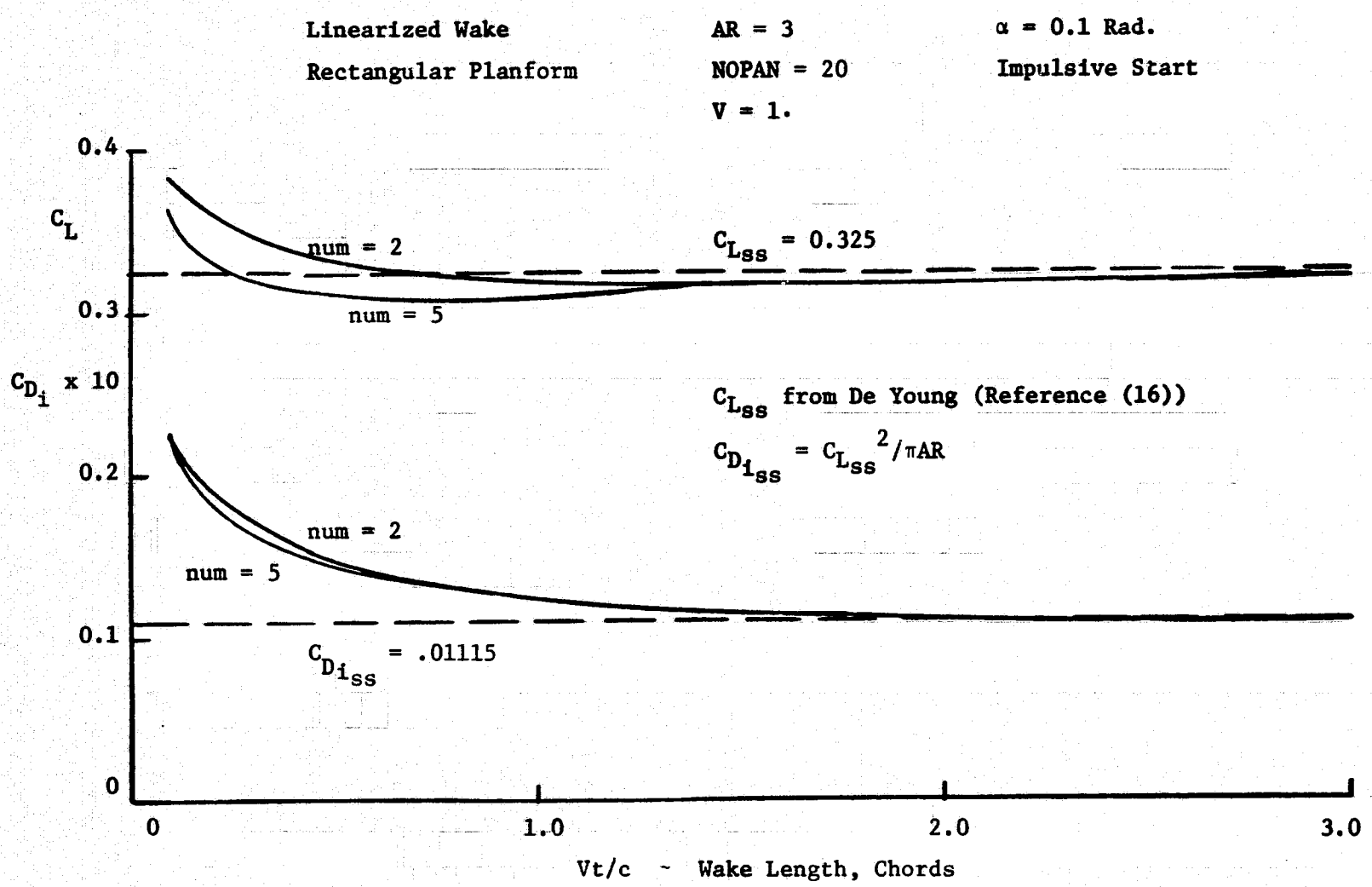

Figure 18. Effect of Number of Spanwise Panels on Induced Drag.

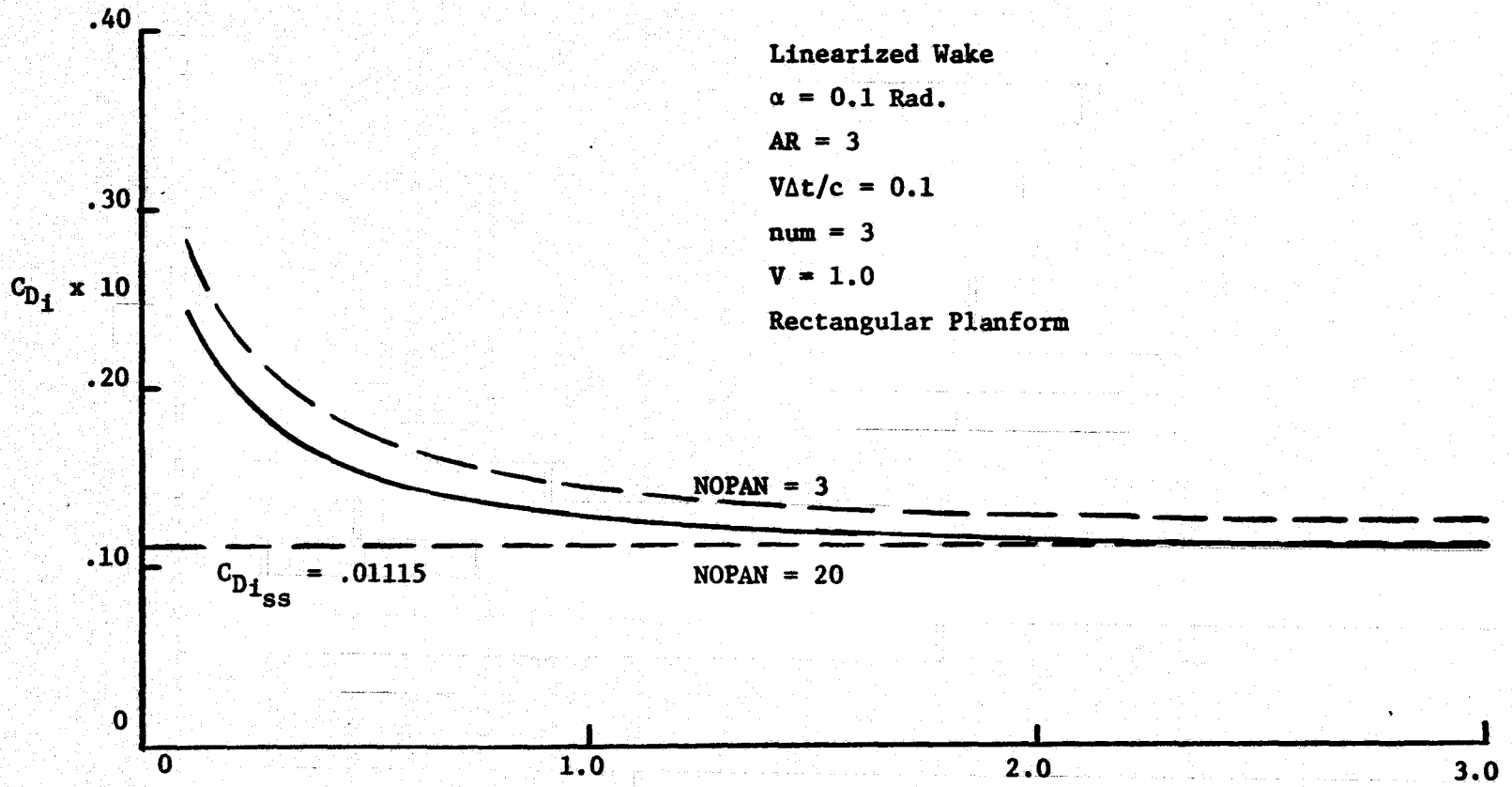

Figure 19. Effect of Wake Type and Boundary Condition Type on C_L.

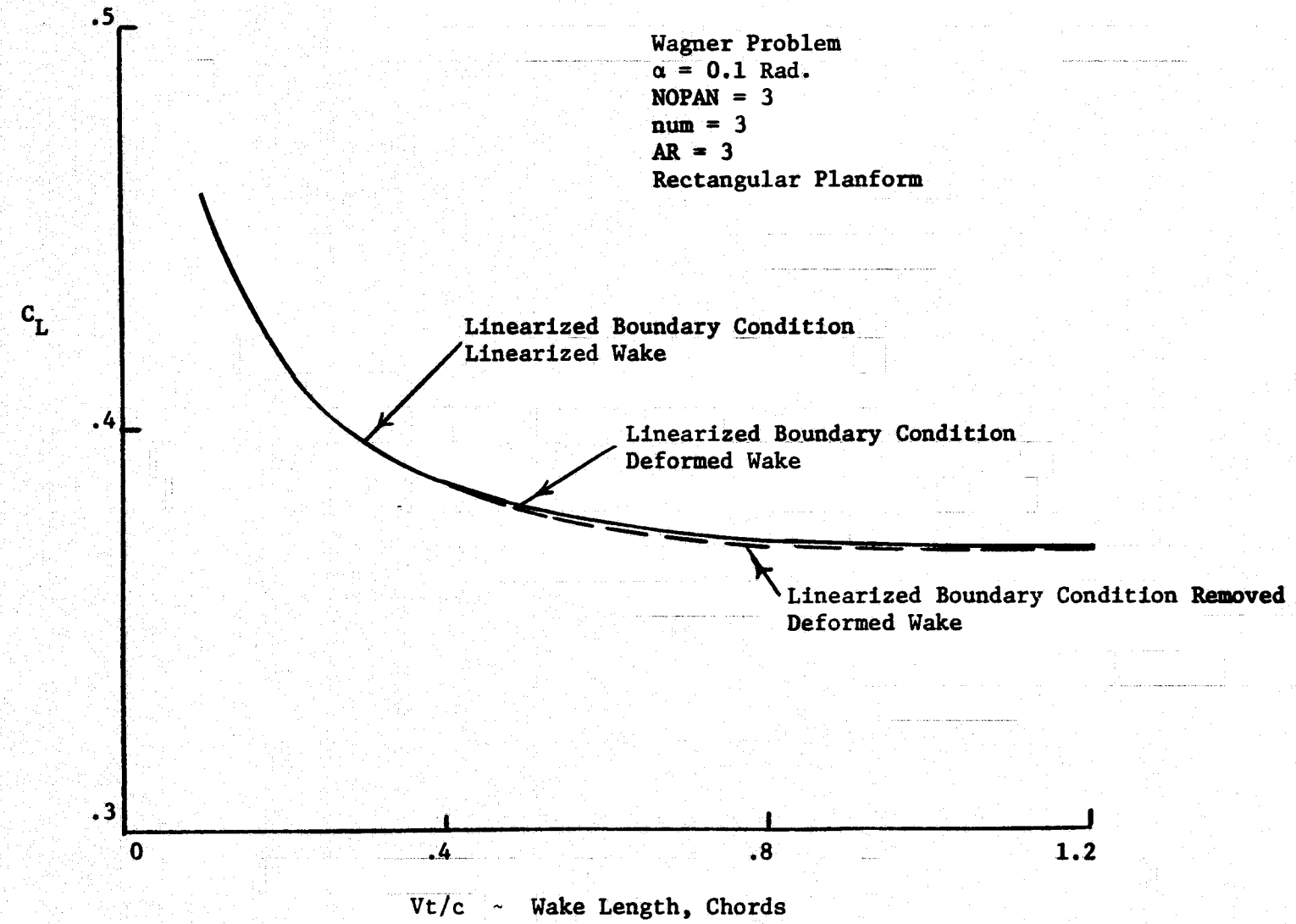

Figure 20. Downstream Profile of the Trailing Vortices for a Semi-Span.

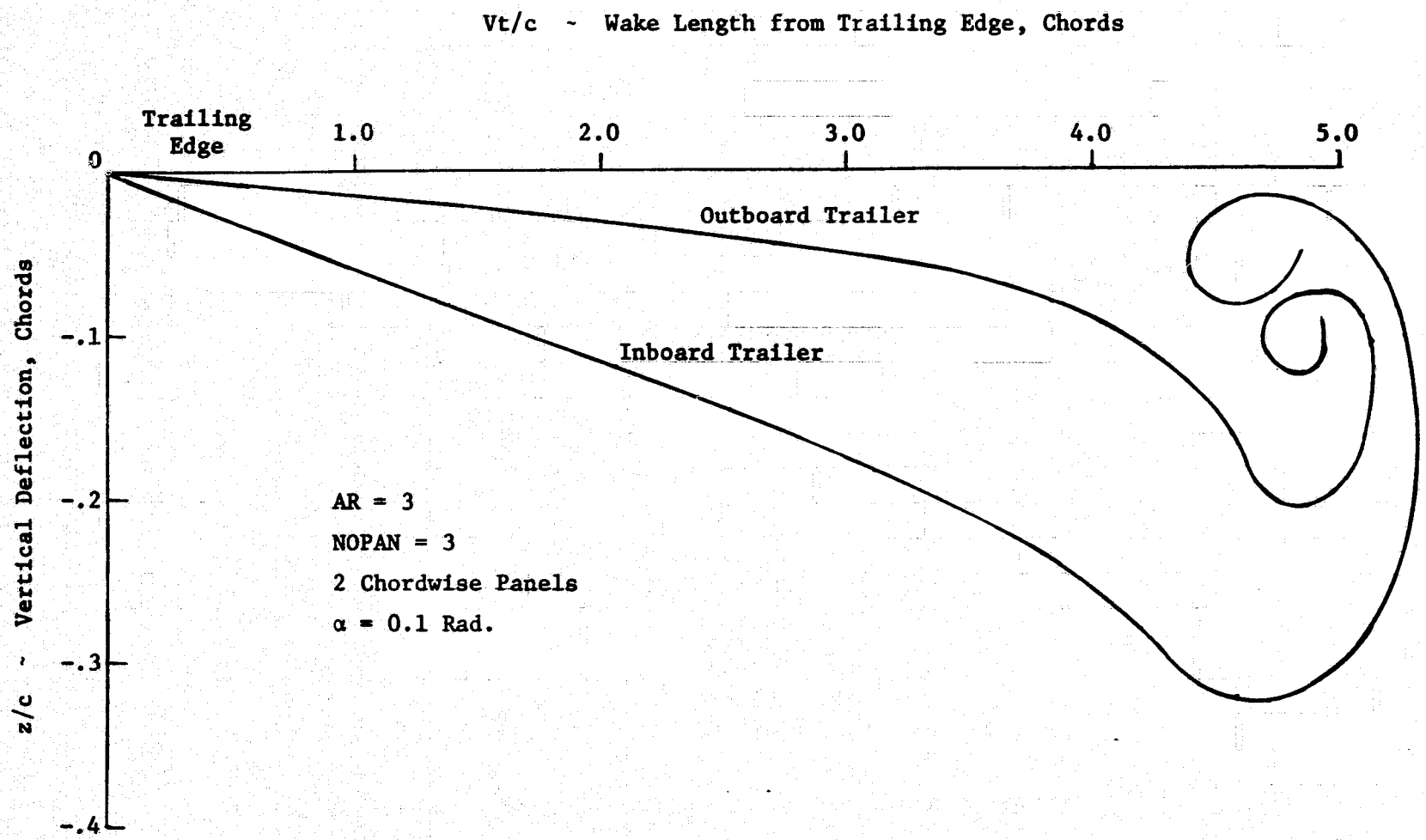

Figure 21. Downstream Profile of the Trailing Vortices for a Semi-Span.

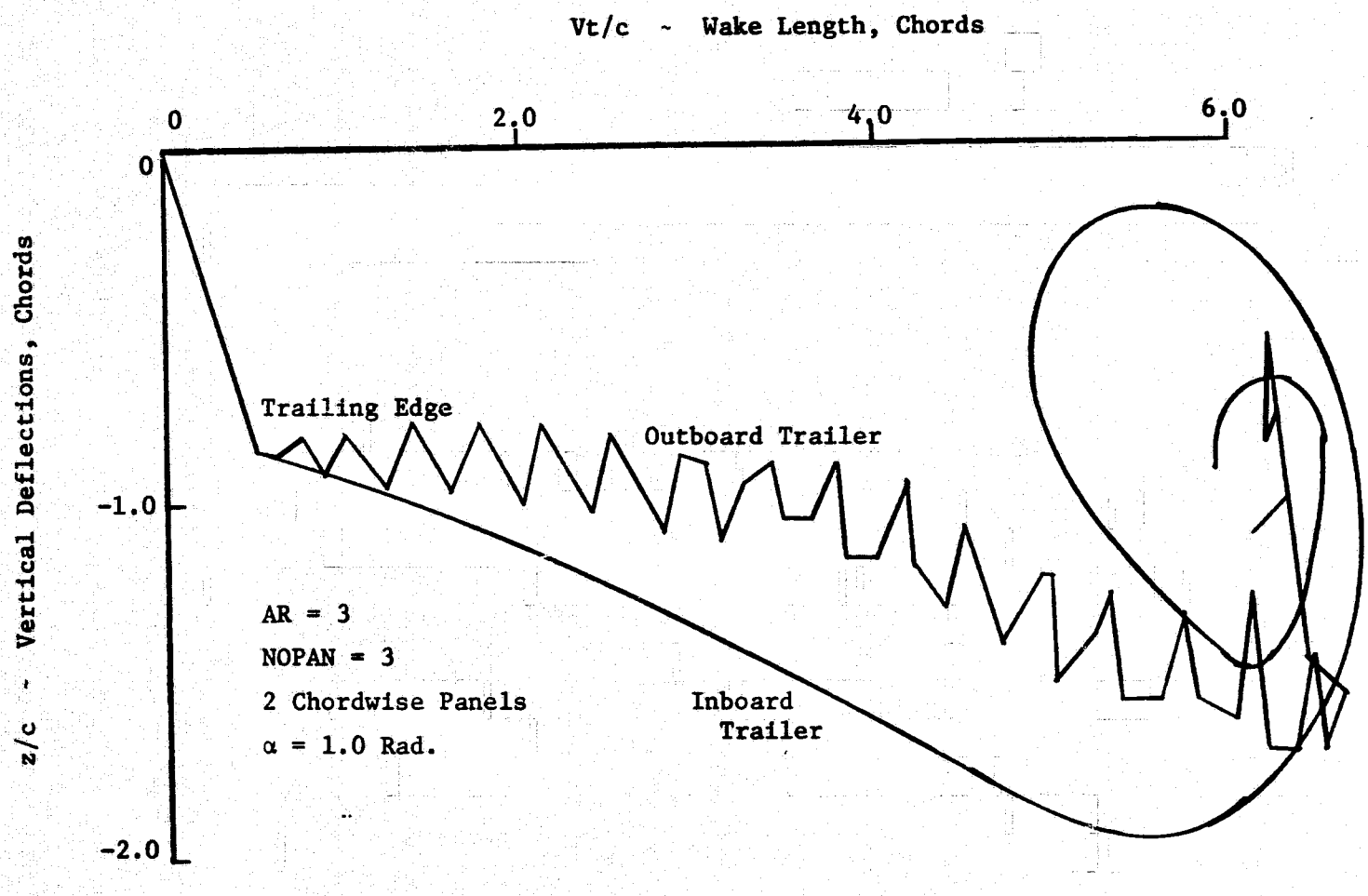

Figure 22. Wing Lift and Induced Drag Coefficients vs. Distance of Wing Travel from Rest.

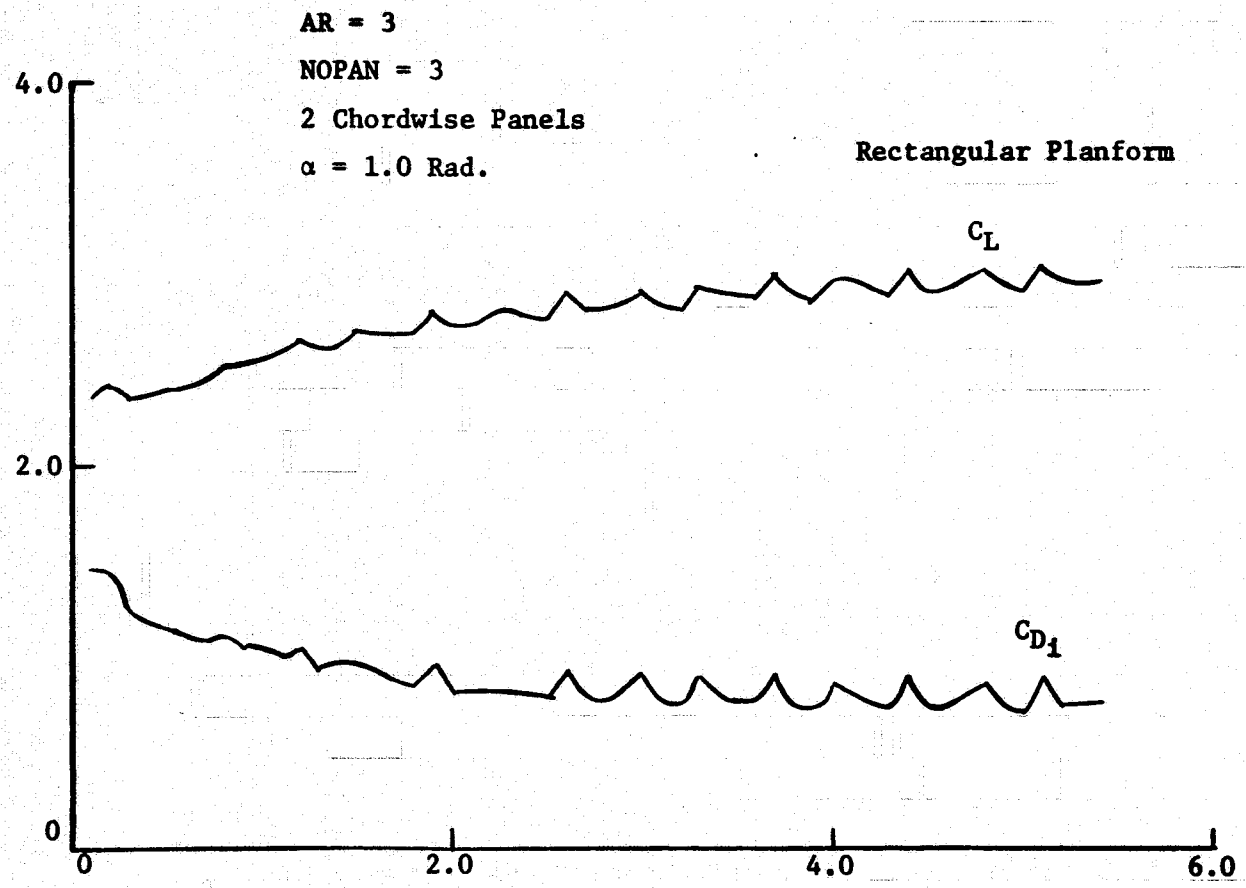

Figure 23. Comparison of Wake Convection Velocities - Z Component.

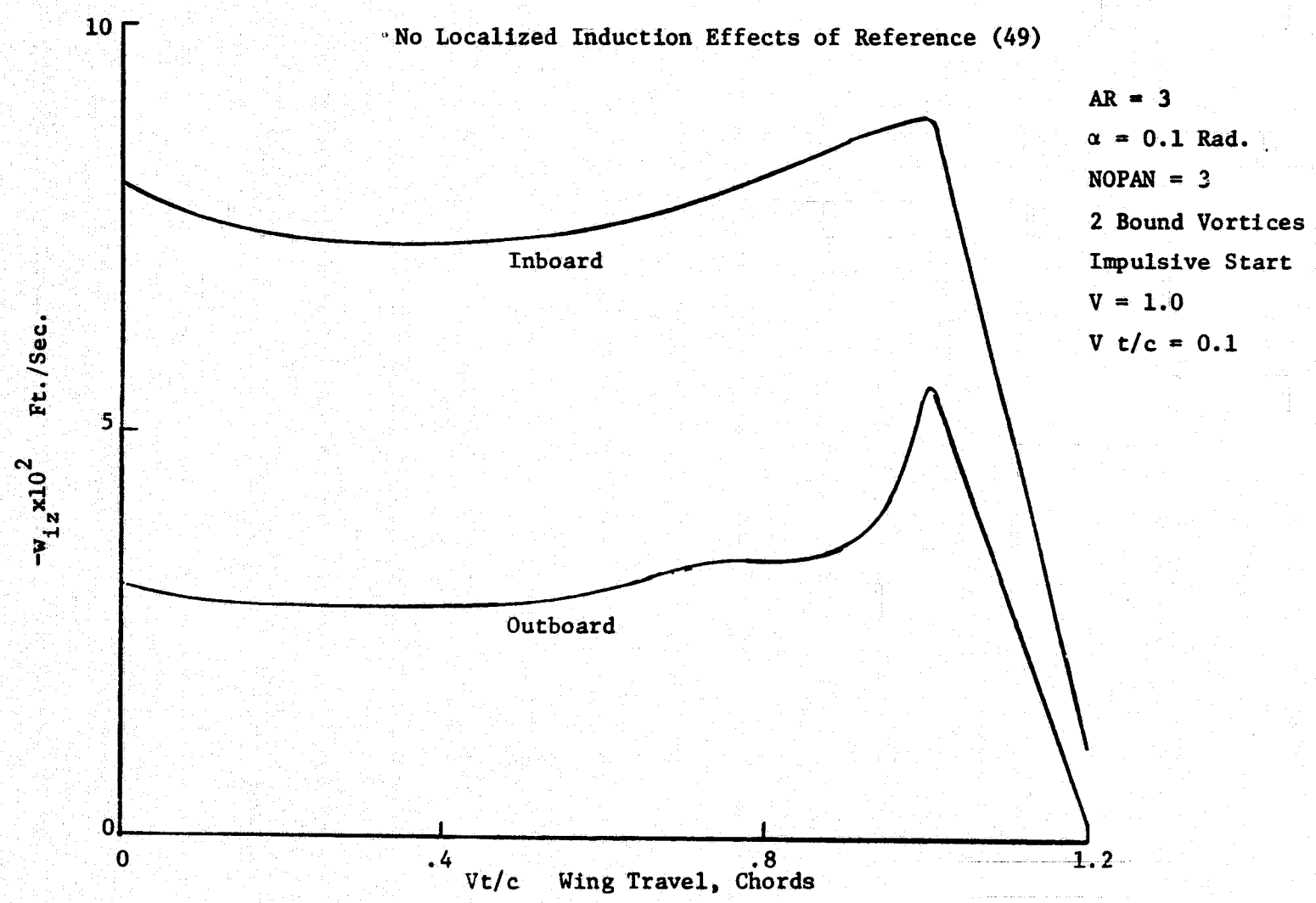

Figure 24. Comparison of Wake Convection Velocities - Y Component.

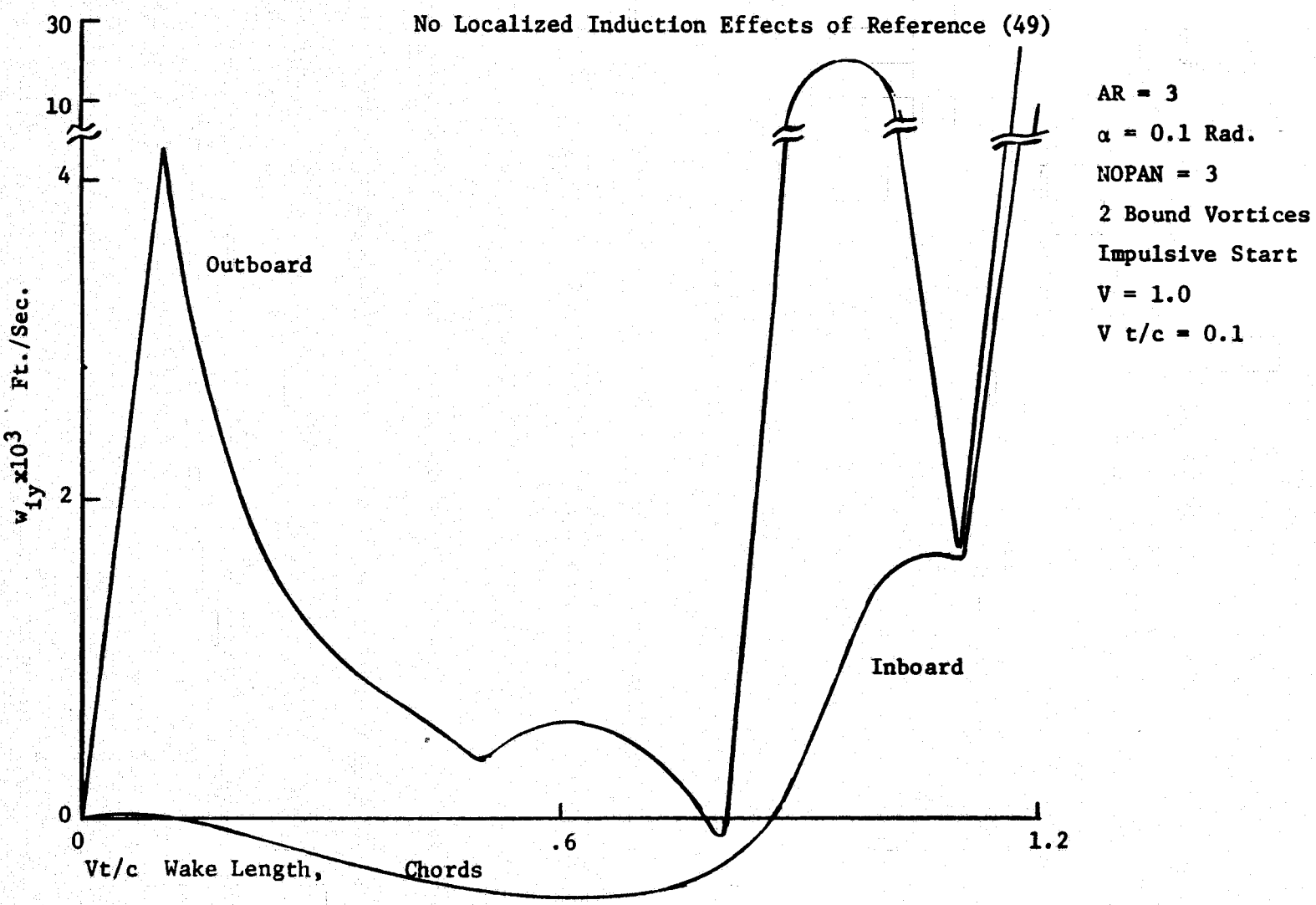

Figure 25. Comparison of Wake Convection Velocities - Z Component.

Localized Induction Effects of Reference (49)

AR = 3	Impulsive Start
α = 0.1 Rad.	V = 1
NOPAN = 3	V t/c = 0.1
2 Bound Vortices	

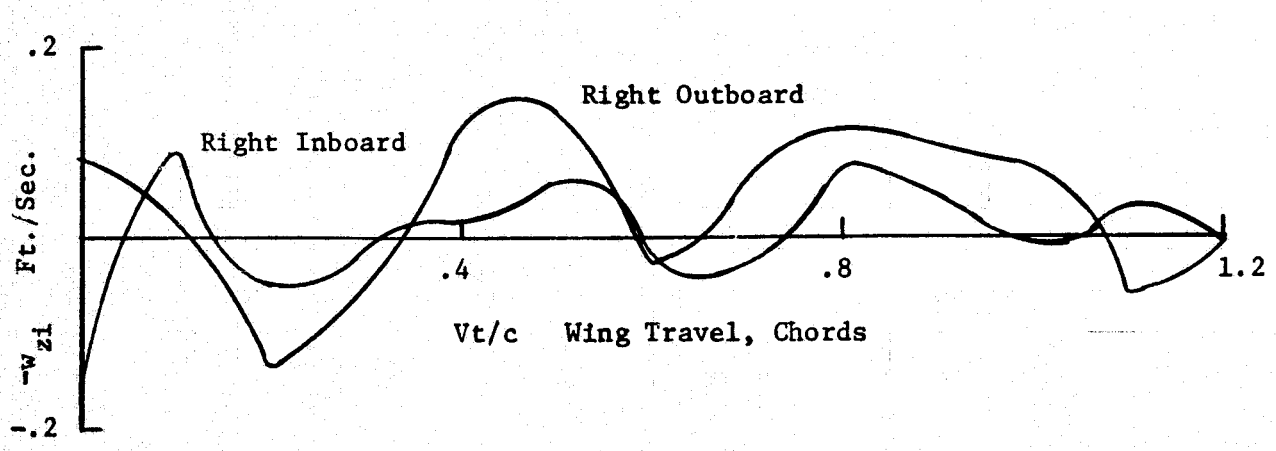

Figure 26. Comparison of Wake Convection Velocities - Y Component.

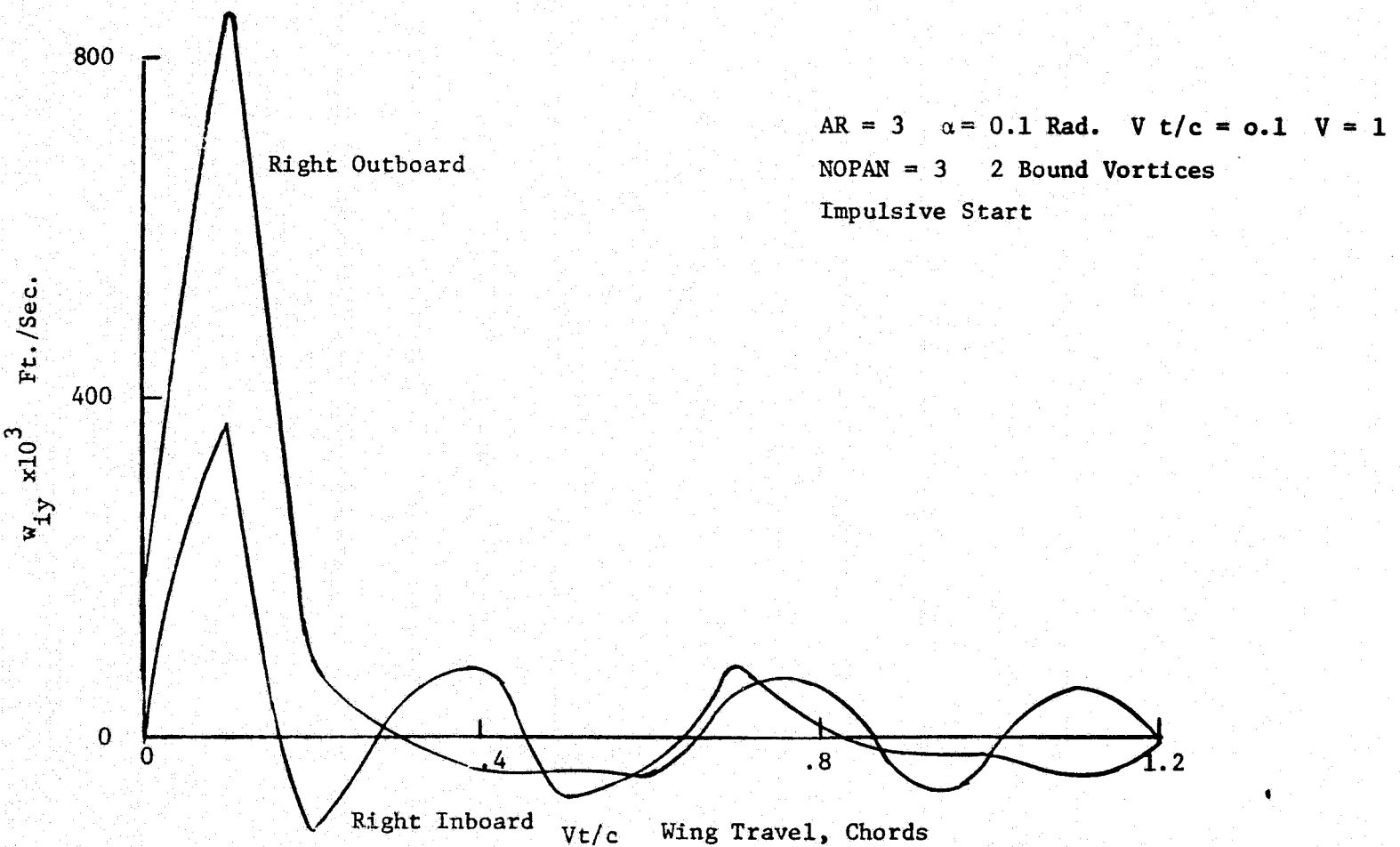

Figure 27. Self Induced Velocity by an Hyperbolic Spiral Vortex Filament.

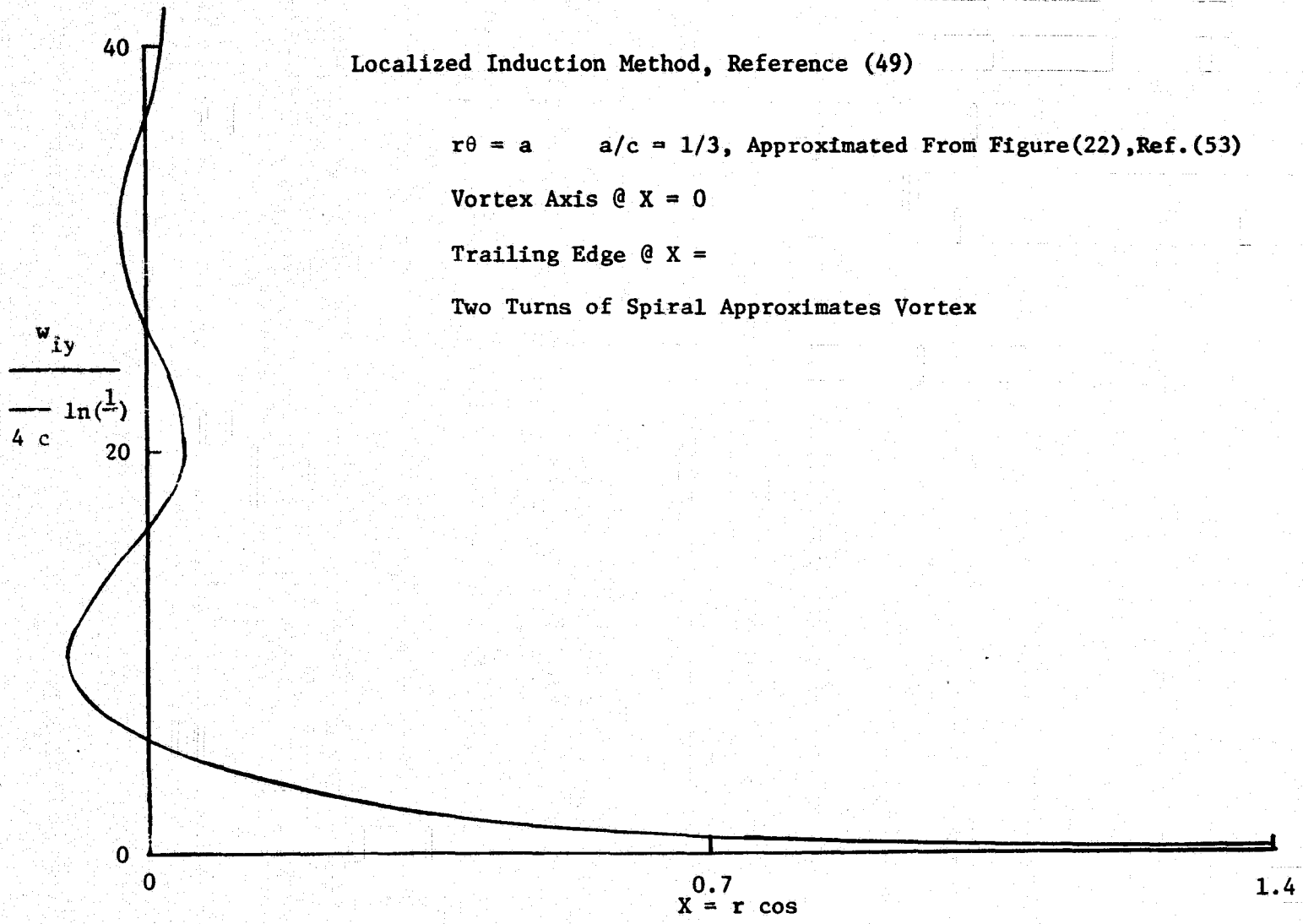

Figure 28A. Formation of Vortex Wake Behind Rectangular Wing, Classic Wake, Proportional Core.

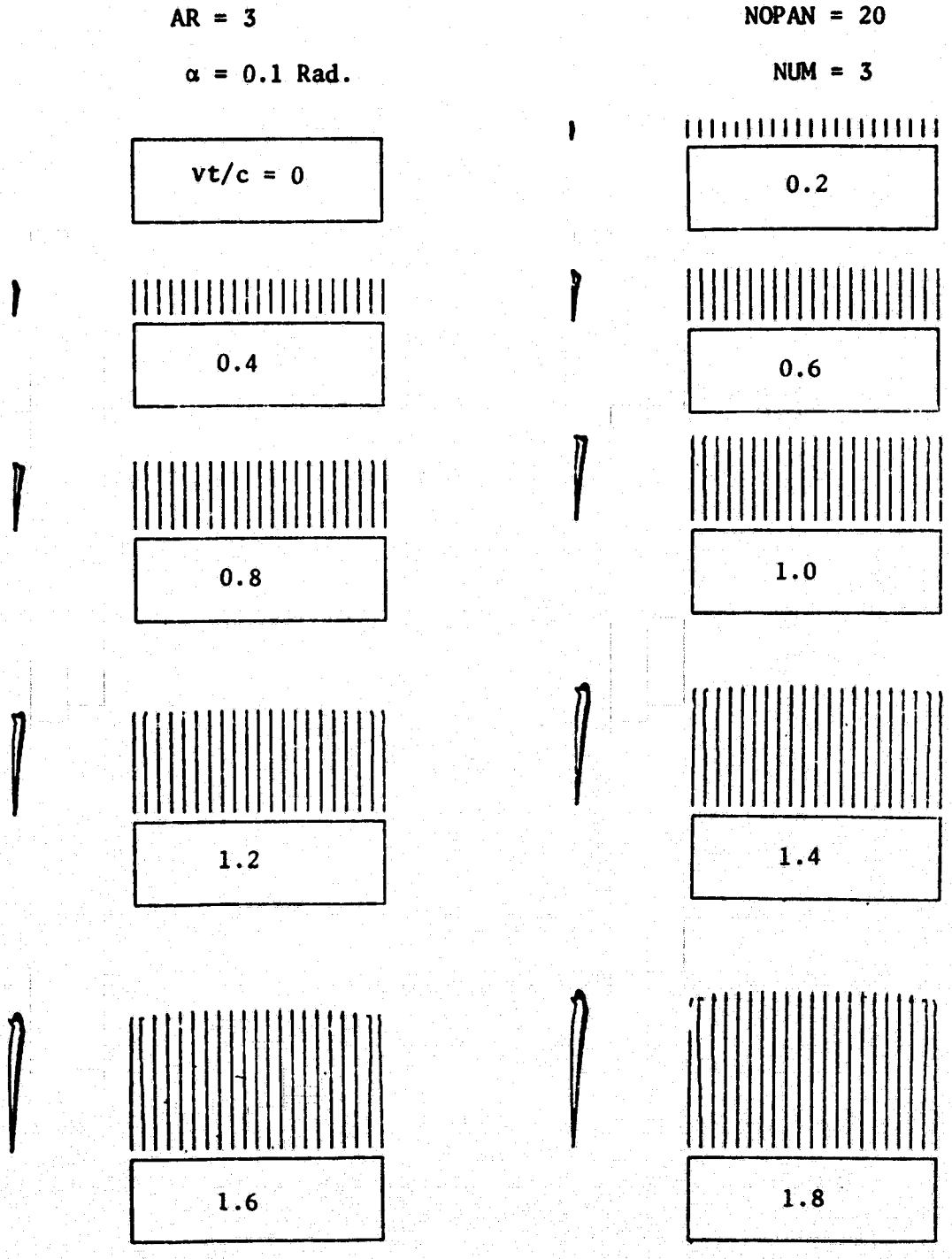

Figure 28B. Formation of Vortex Wake Behind a Rectangular Wing, Classic Wake, Proportional Core.

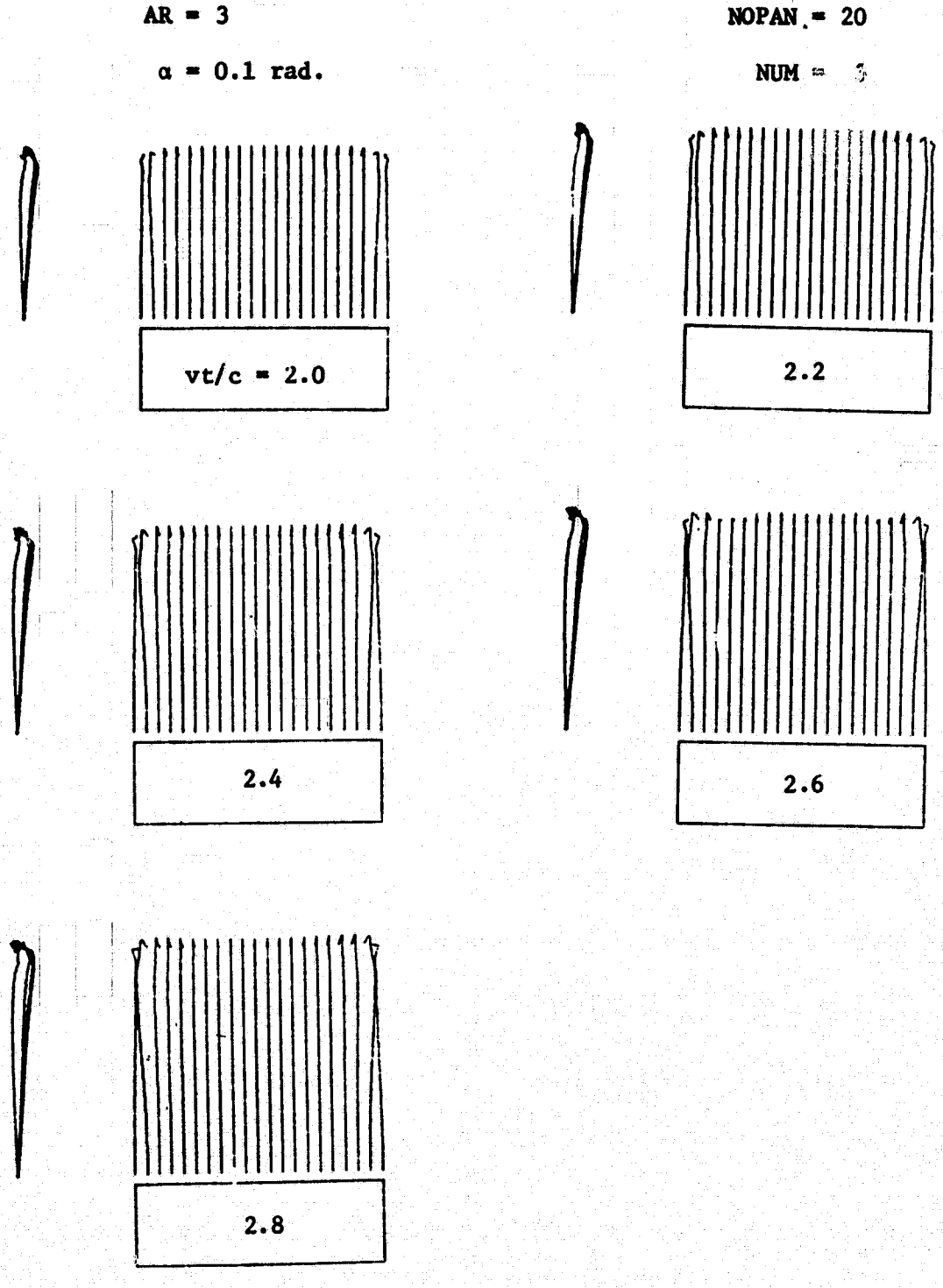

Figure 29A. Formation of Vortex Wake Behind a Rectangular Wing, Classic Wake, Fixed Core, $h_c = 10^{-6}$ ft.

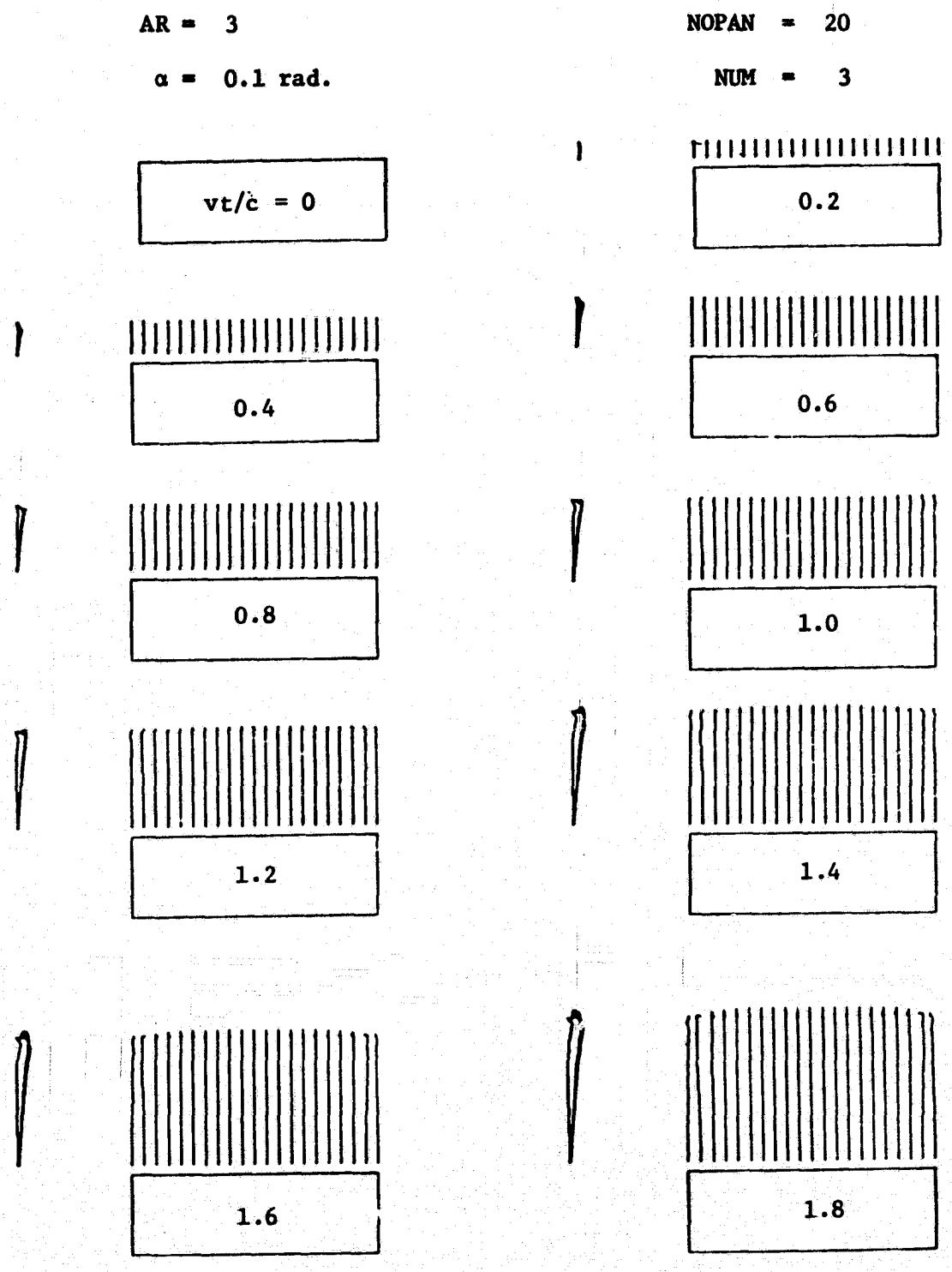

Figure 29B. Formation of Vortex Wake Behind a Rectangular Wing, Classic Wake, Fixed Core, $h_c = 10^{-6}$ ft.

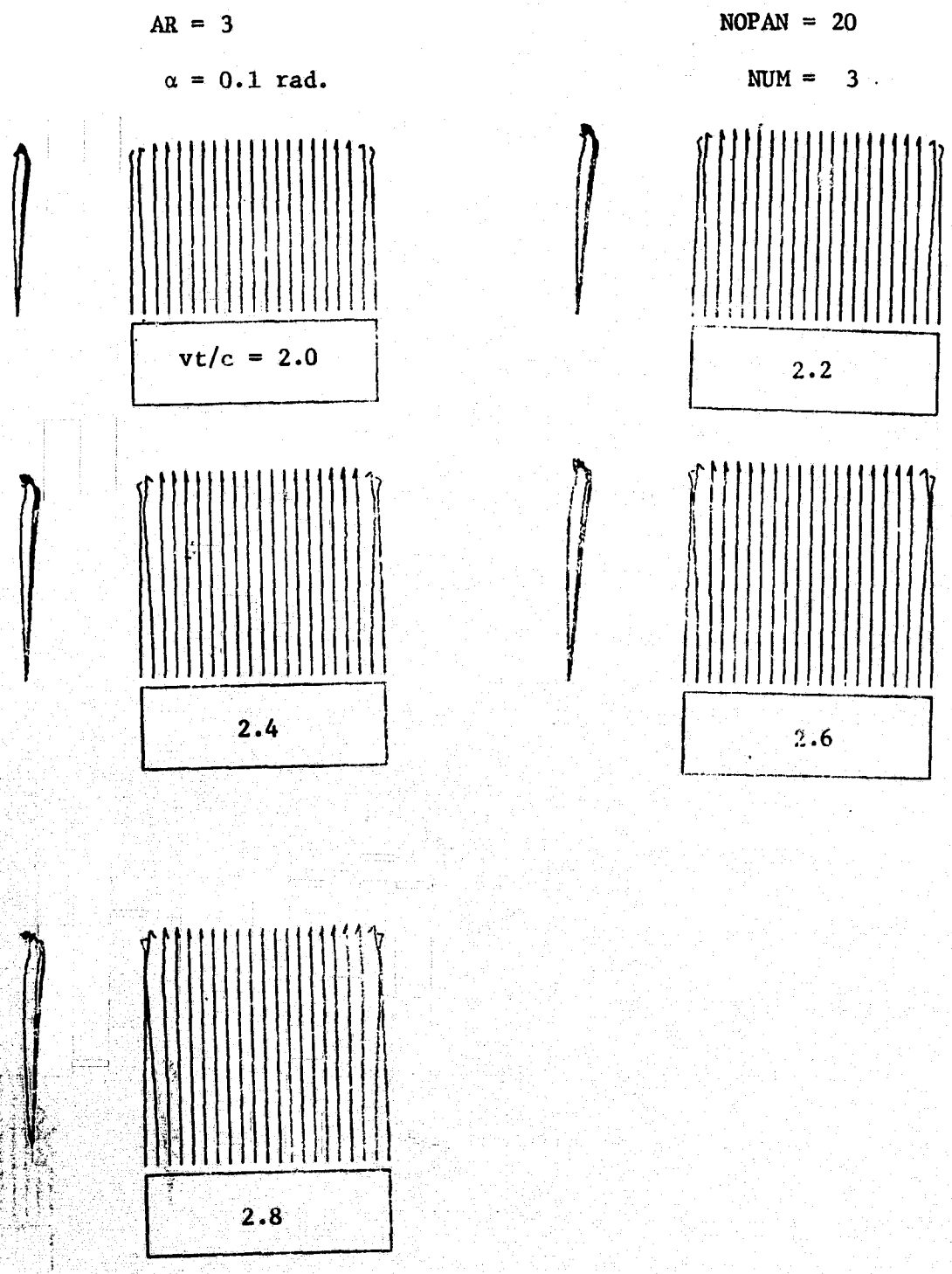

Figure 30A. Formation of Vortex Wake Behind a Rectangular Wing, Localized Induction Effect, Proportional Core.

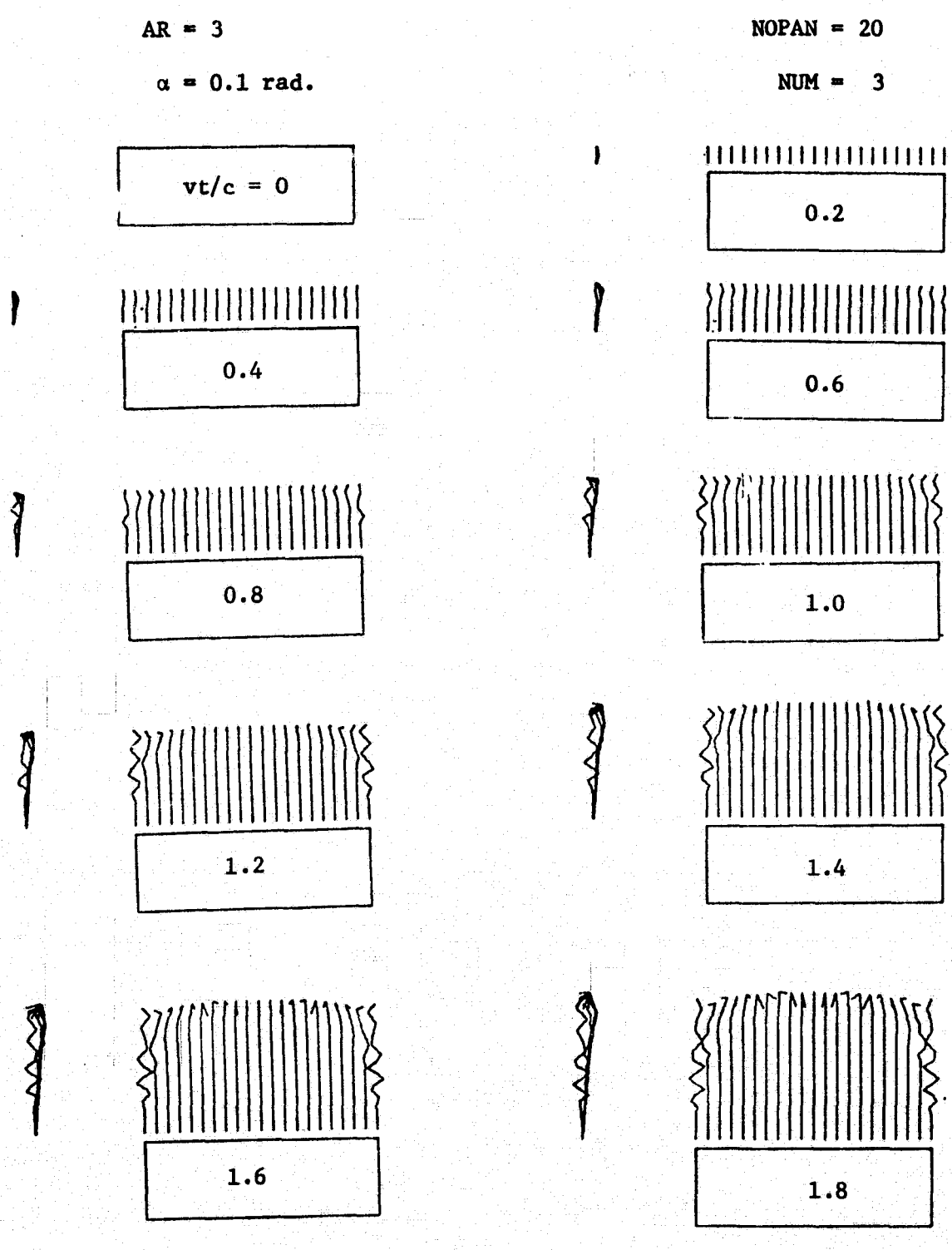

Figure 30B. Formation of Vortex Wake Behind a Rectangular Wing, Localized Induction Effect, Proportional Core.

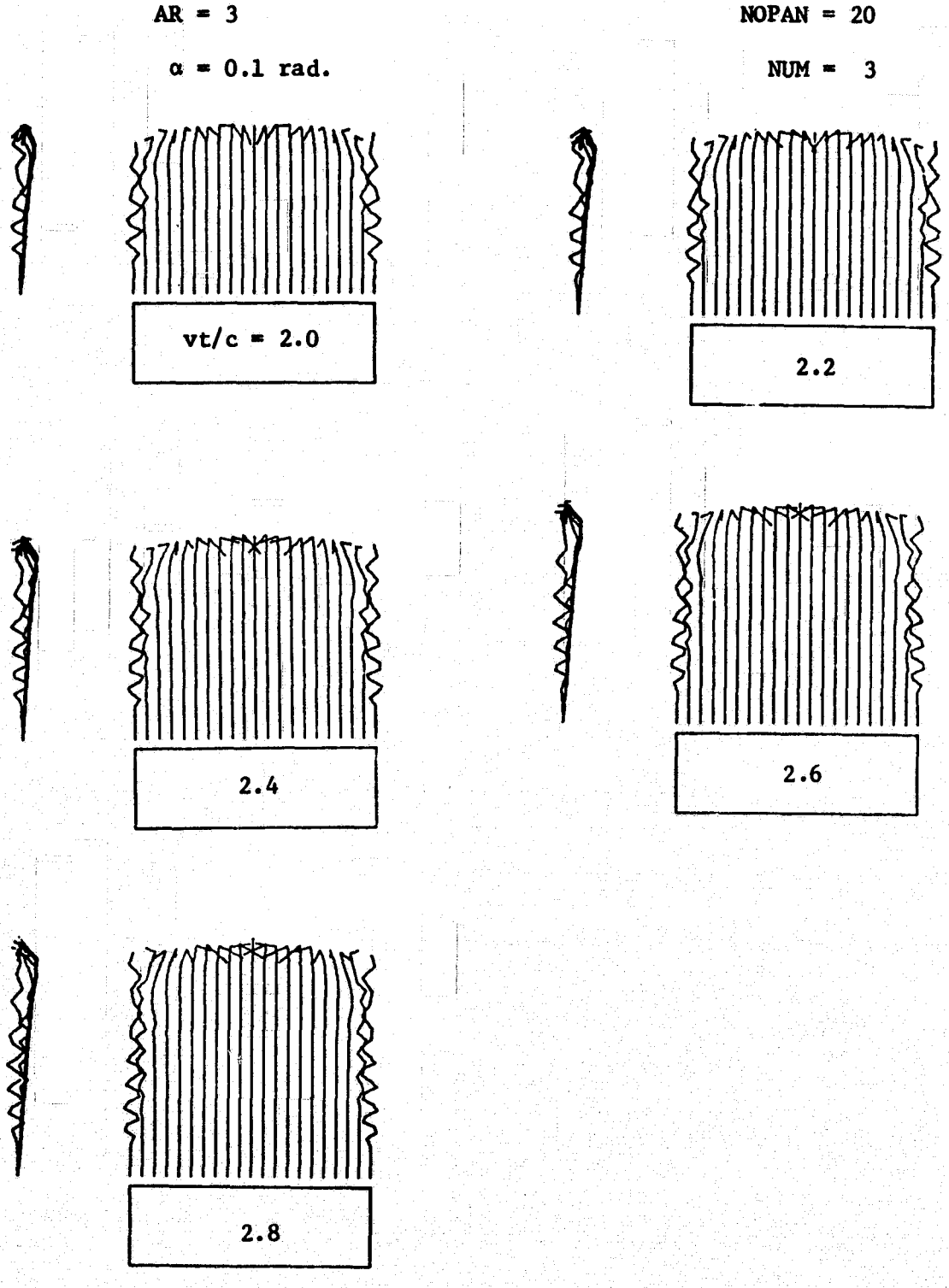

Figure 31A. Formation of Vortex Wake Behind a Rectangular Wing, Localized Induction Effect, Fixed Core, $h_c = 10^{-6}$ ft.

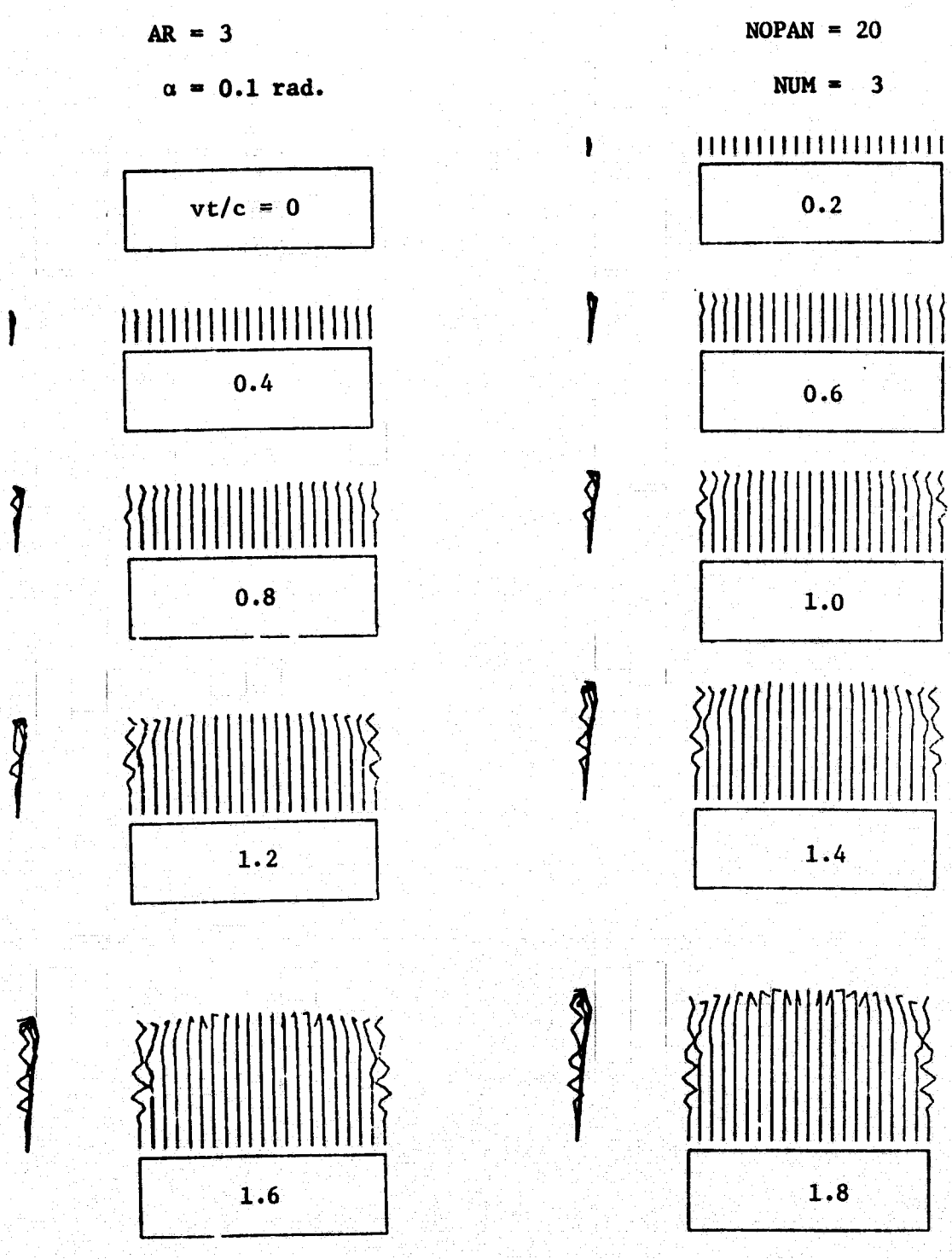

Figure 31B. Formation of Vortex Wake Behind a Rectangular Wing, Localized Induction Effect, Fixed Core, $h_c = 10^{-6}$ ft.

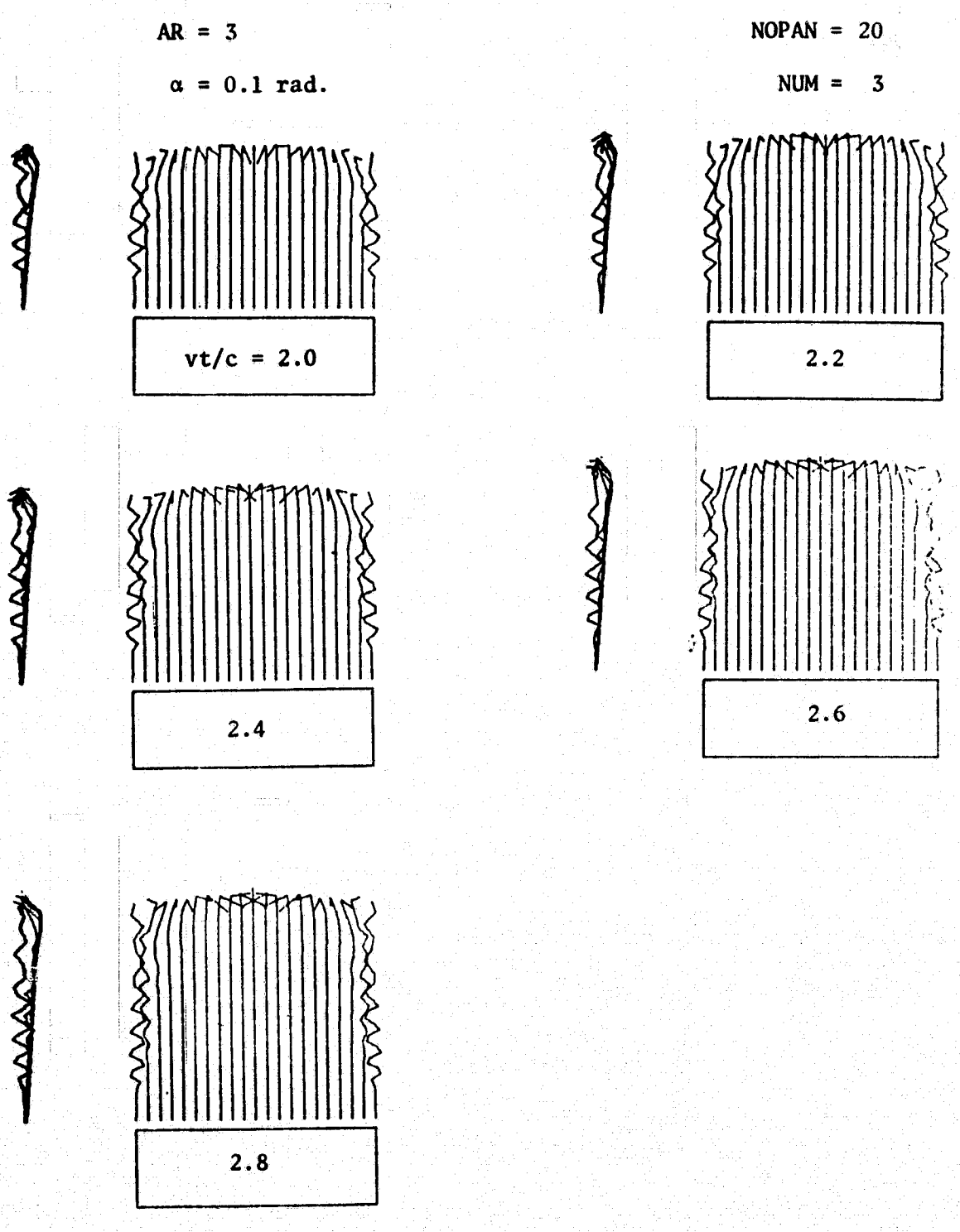

Figure 32A. Formation of Vortex Wake Behind a Rectangular Wing, Localized Induction Effect, Fixed Core, $h_c = 10^{-10}$ ft.

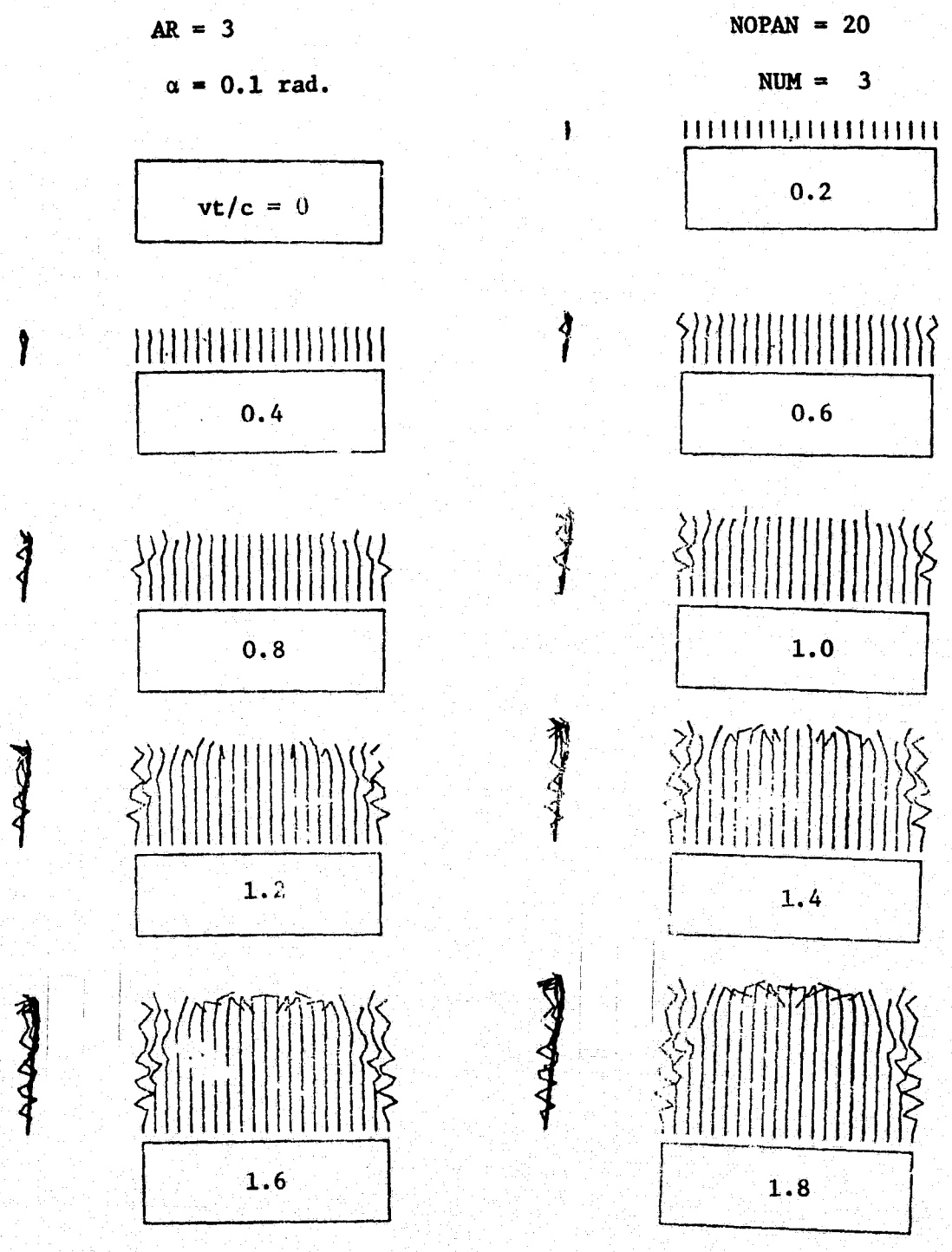

Figure 32B. Formation of Vortex Wake Behind a Rectangular Wing, Localized Induction Effect, Fixed Core, $h_c = 10^{-10}$ ft.

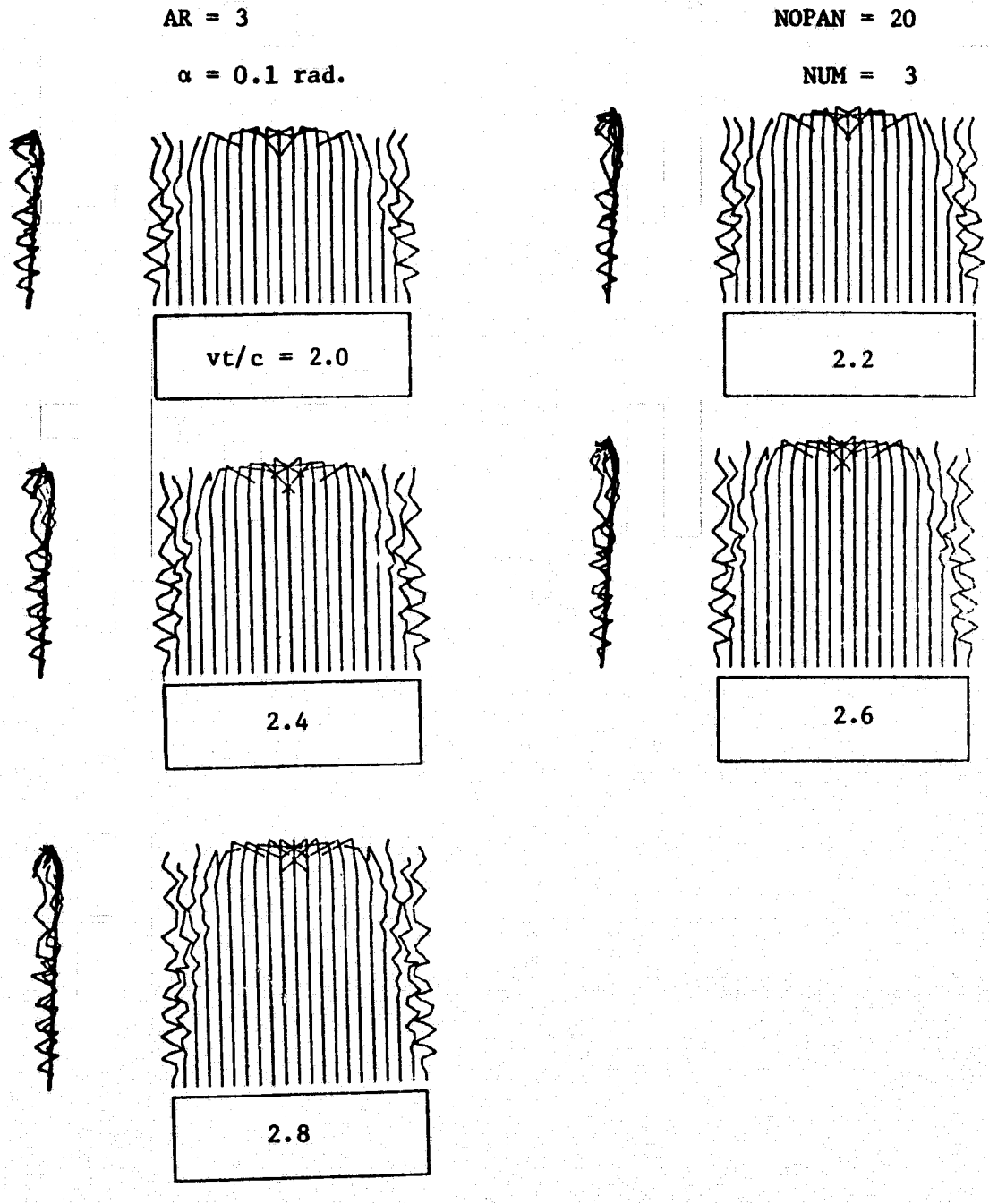

Figure 33. Effect of Wake Rollup on Finite Wing Performance.

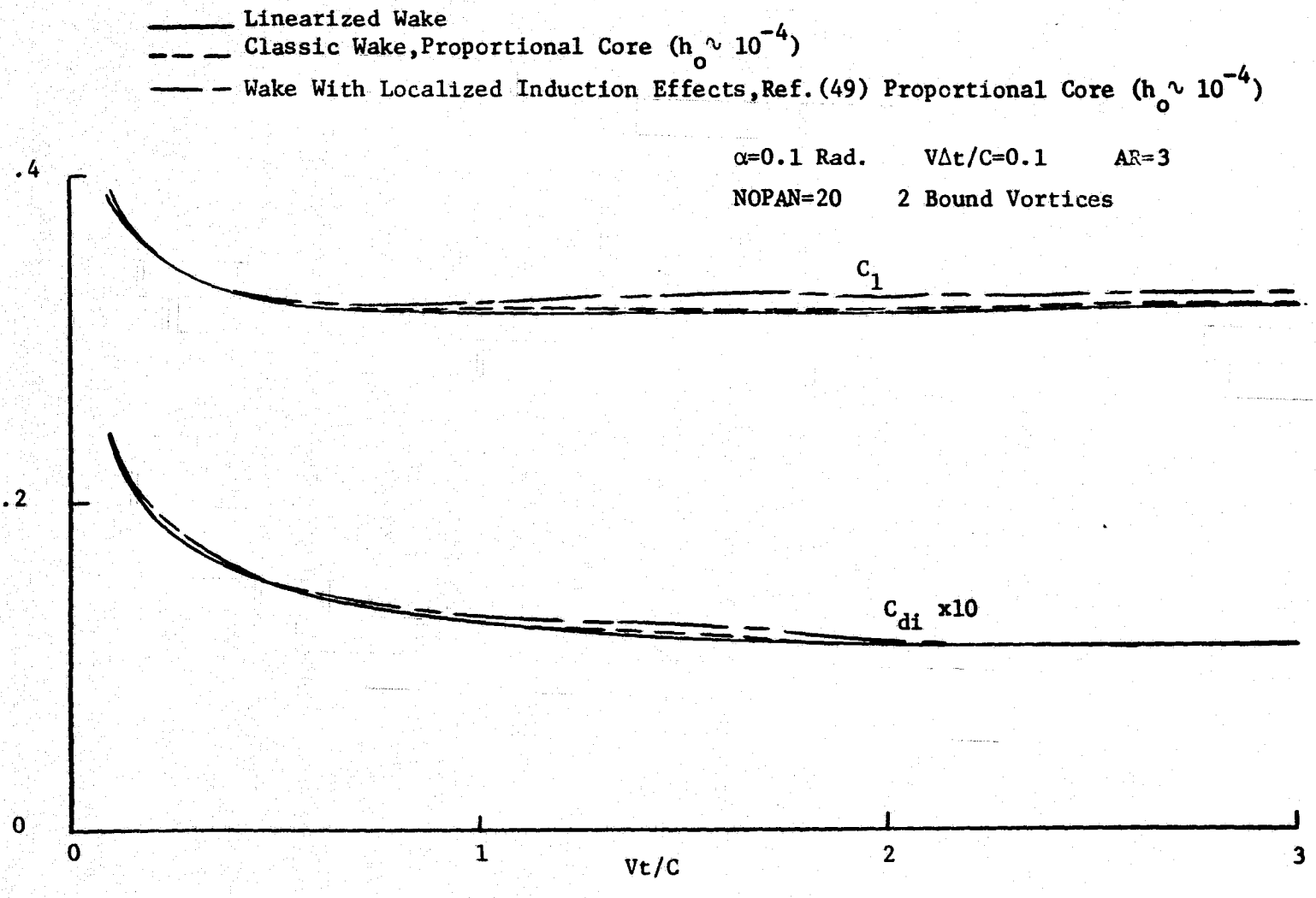

Figure 34. Effect of Wake Rollup on Finite Wing Performance.

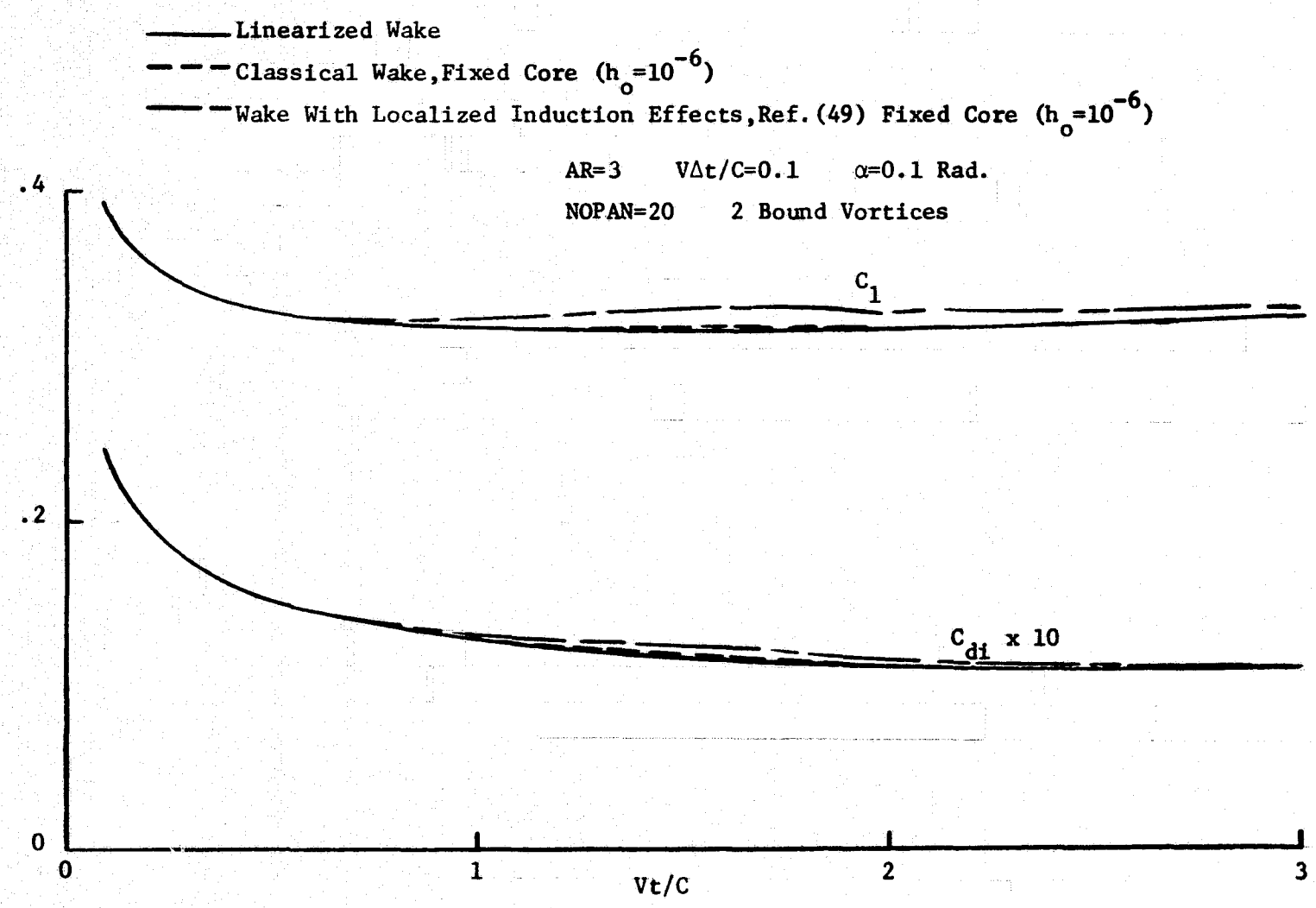

Figure 35. Comparison Between Direct Numerical Integration and Equation 52 for Thrust Determination.

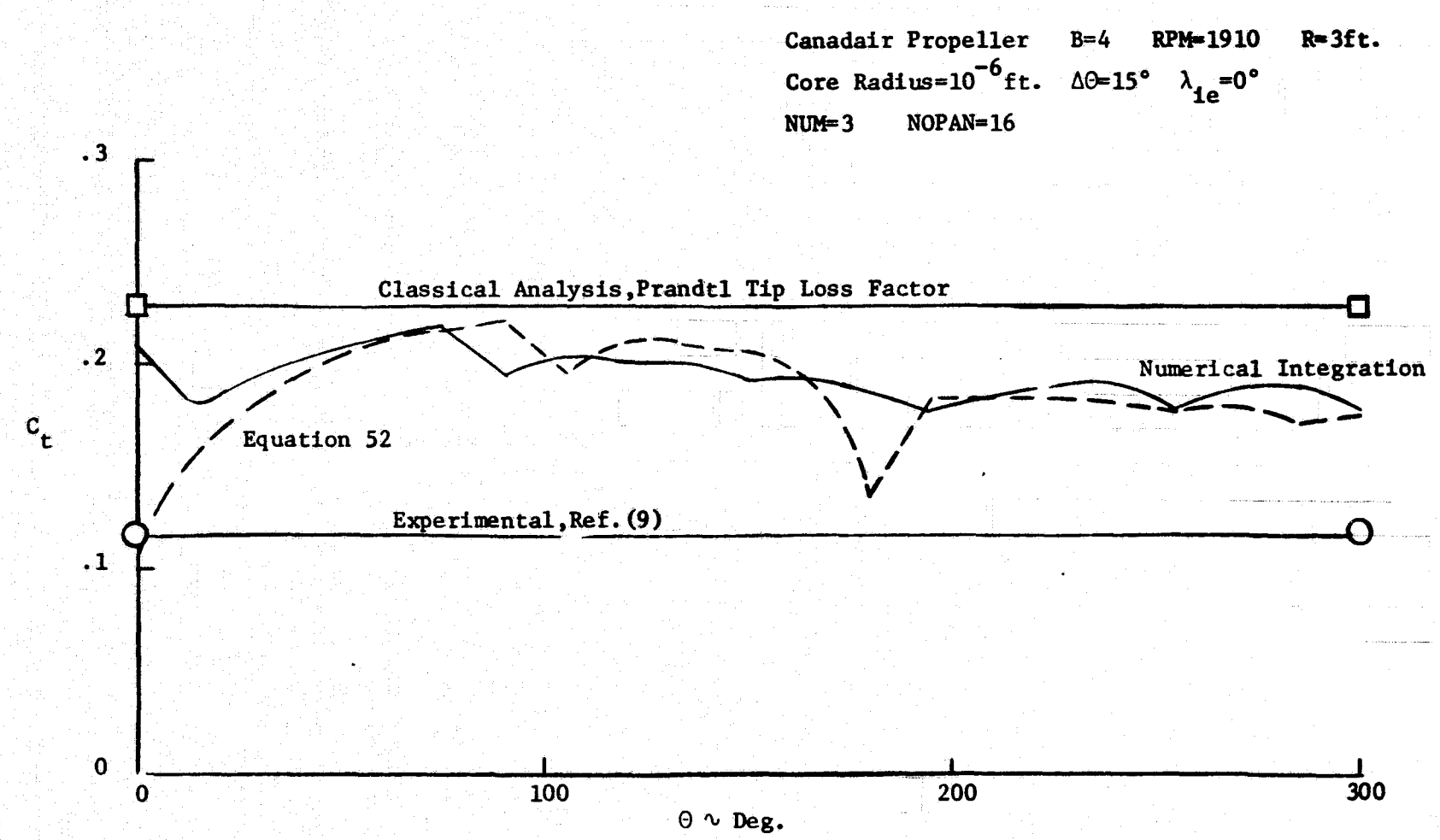

Figure 36. Comparison Between Direct Numerical Integration and Equation 52 for Thrust Determination.

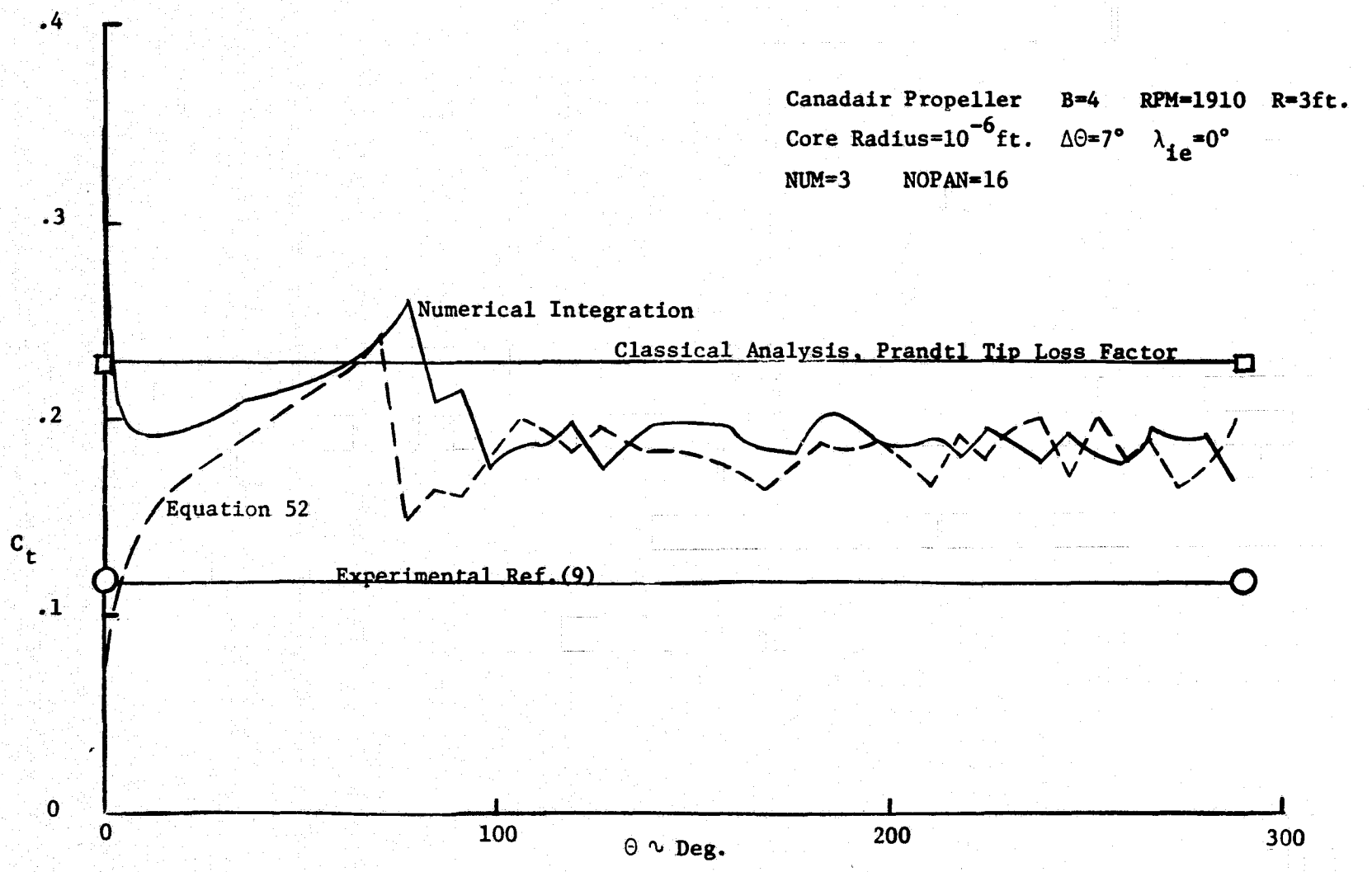

Figure 37. Comparison Between Direct Numerical Integration and Equation 52 for Thrust Determination.

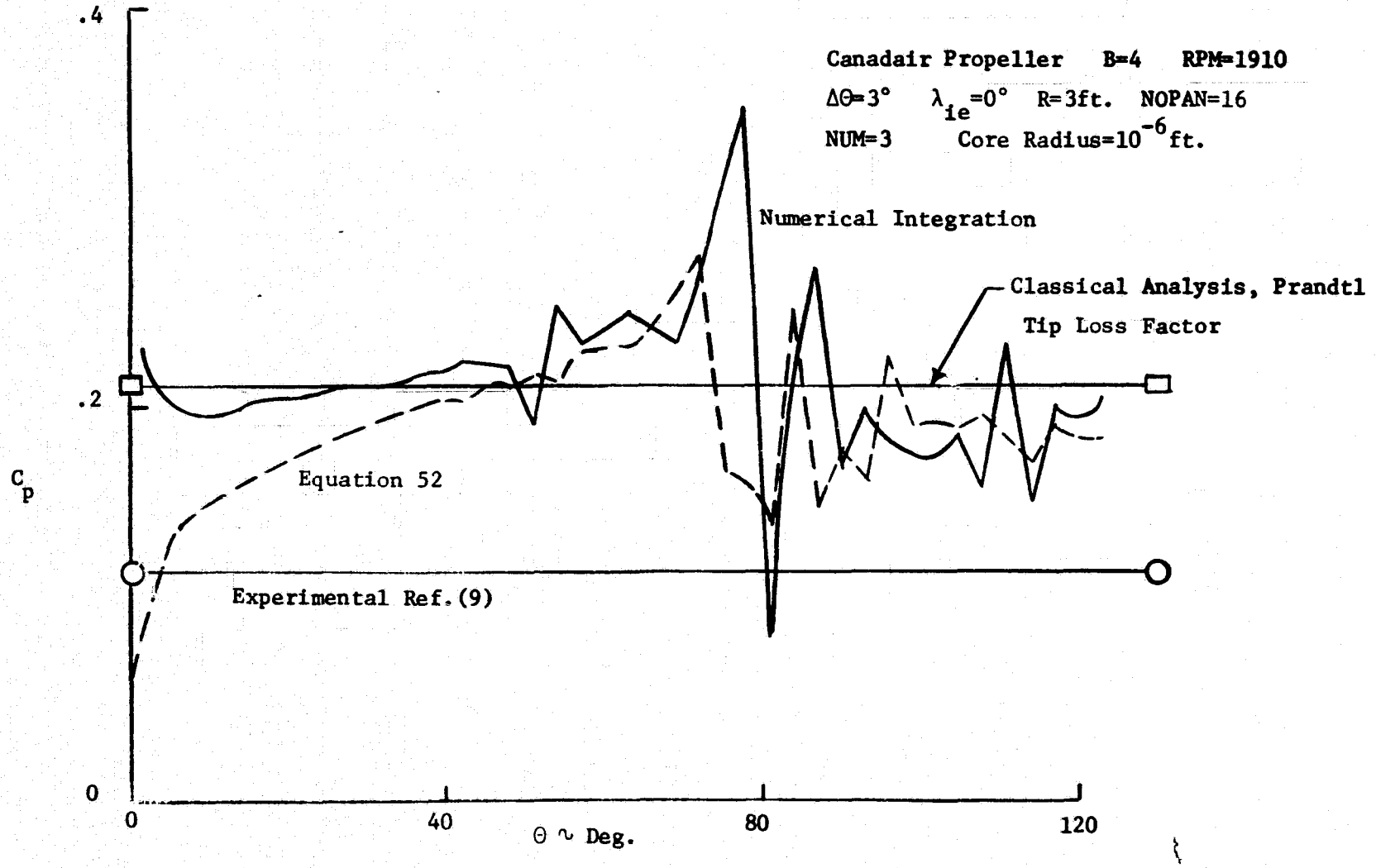

Figure 38. Comparison Between Direct Numerical Integration and Equation 52 for Power Determination.

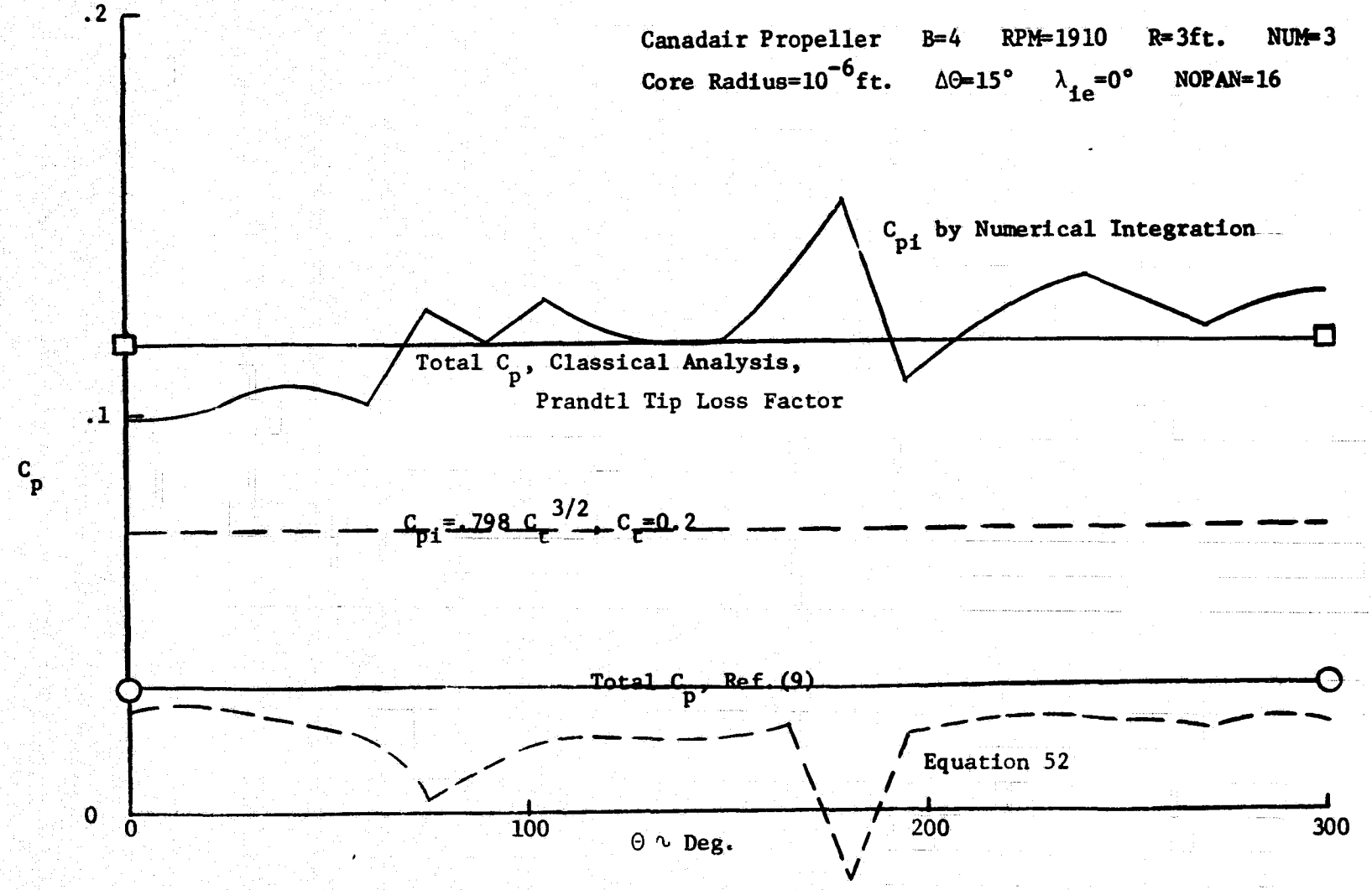

Figure 39. Comparison Between Direct Numerical Integration and Equation 52 for Power Determination.

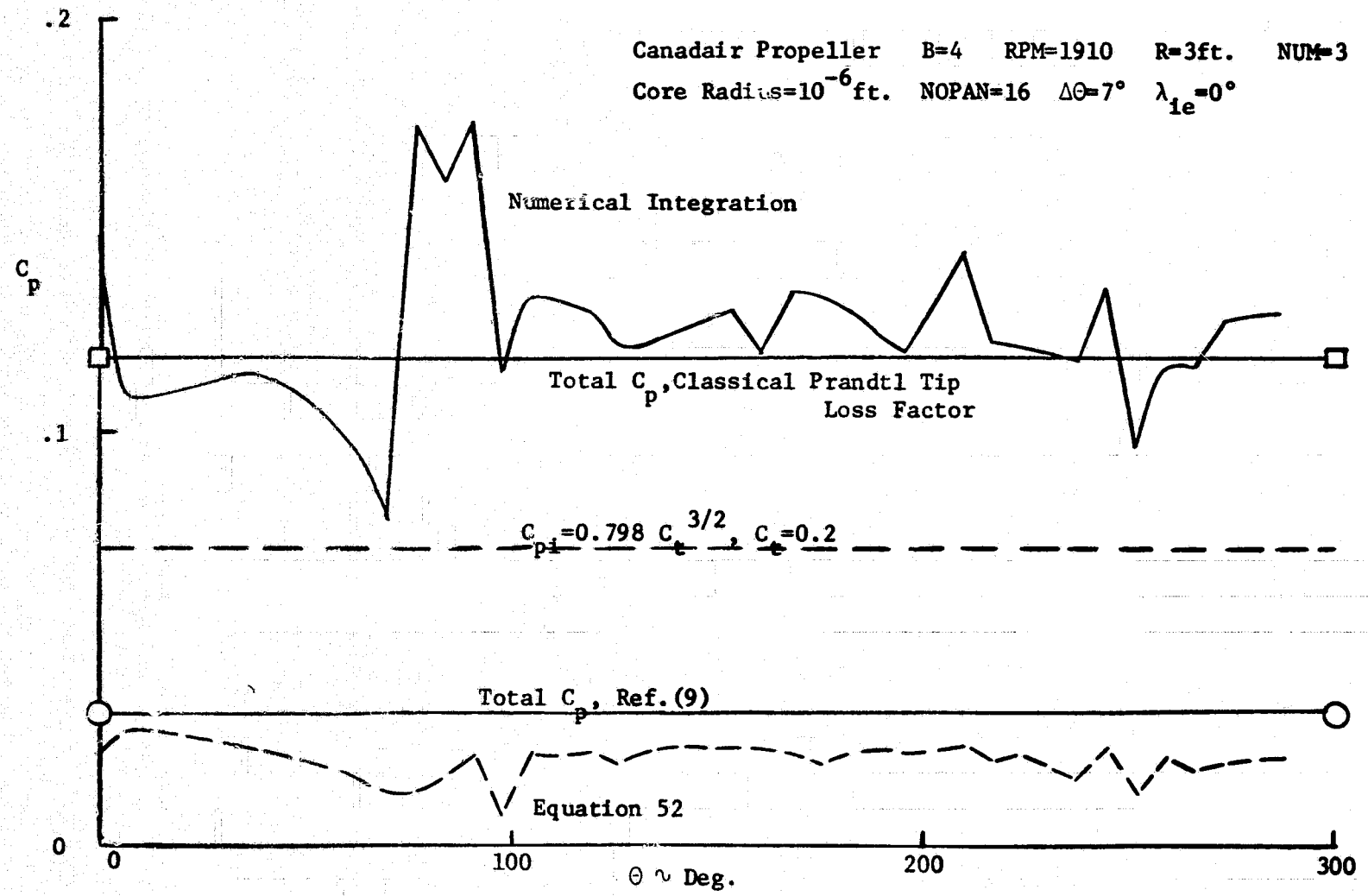

Figure 40. Comparison Between Numerical Integration and Equation 52 for Power Determination.

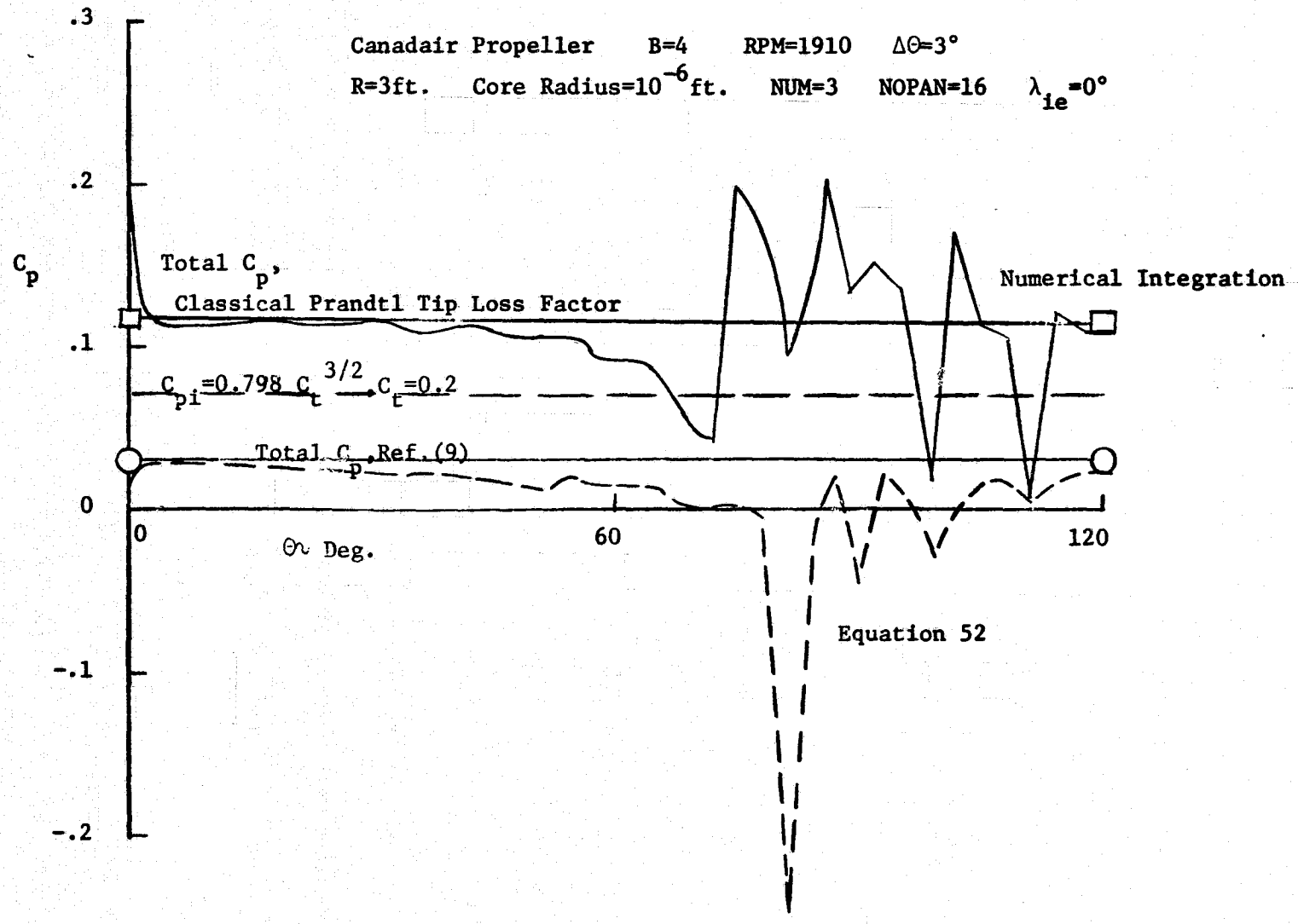

Figure 41. Effect of Azimuth Step Size on Bound Circulation.

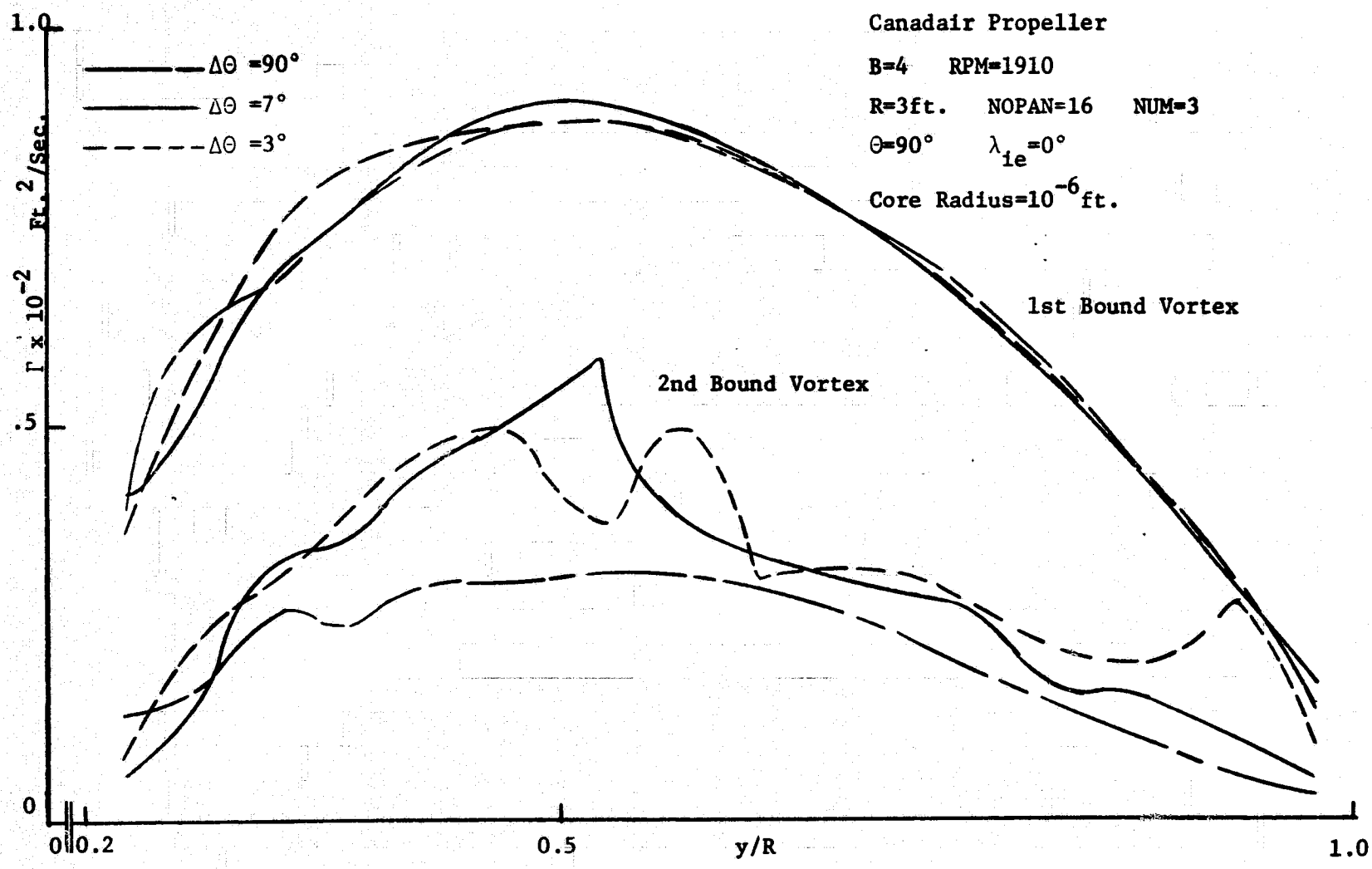

Figure 42. Effect of Azimuth Step Size on Spanwise Distribution of Blade Angle of Attack.

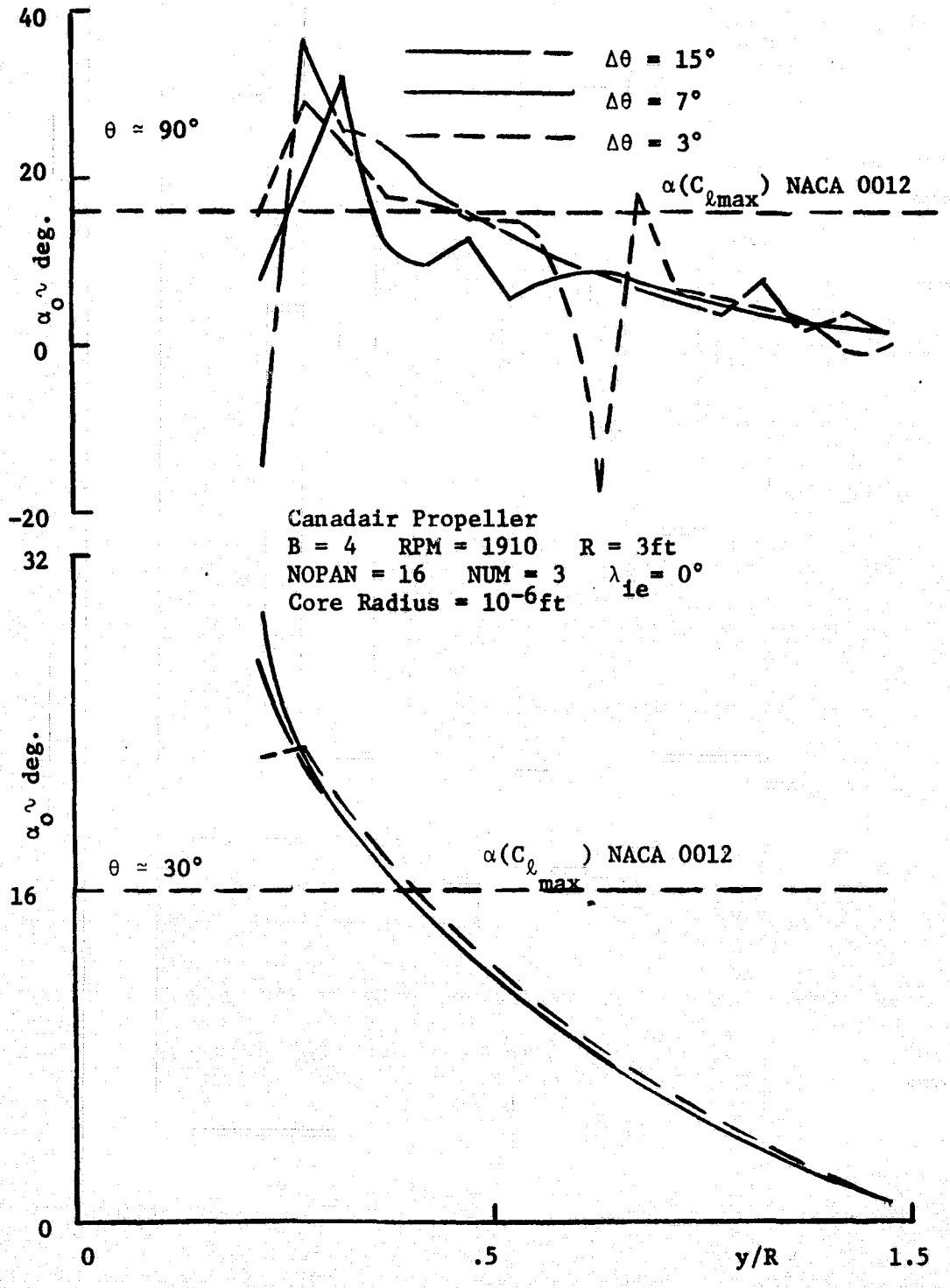

Figure 43. Comparison of Azimuth Step Size on Thrust and Induced Power Distributions.

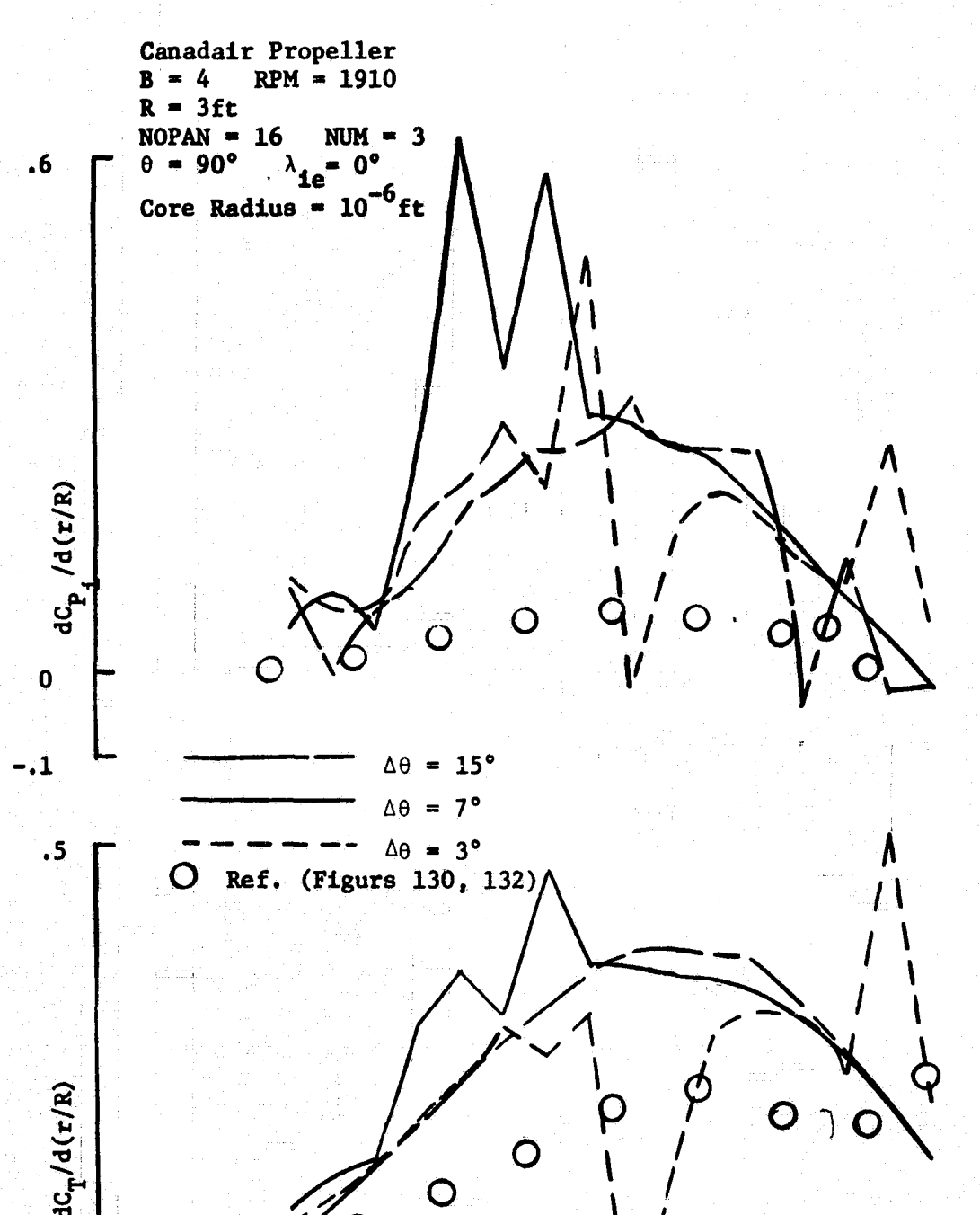

Figure 44. Propeller Vortex Wake Generation, $\Delta\theta = 15°$, $h_c = 10^{-6}$ ft.

Canadair Propeller, Reference (9)
B = 4, 16 Panels, One Blade Wake-Shown

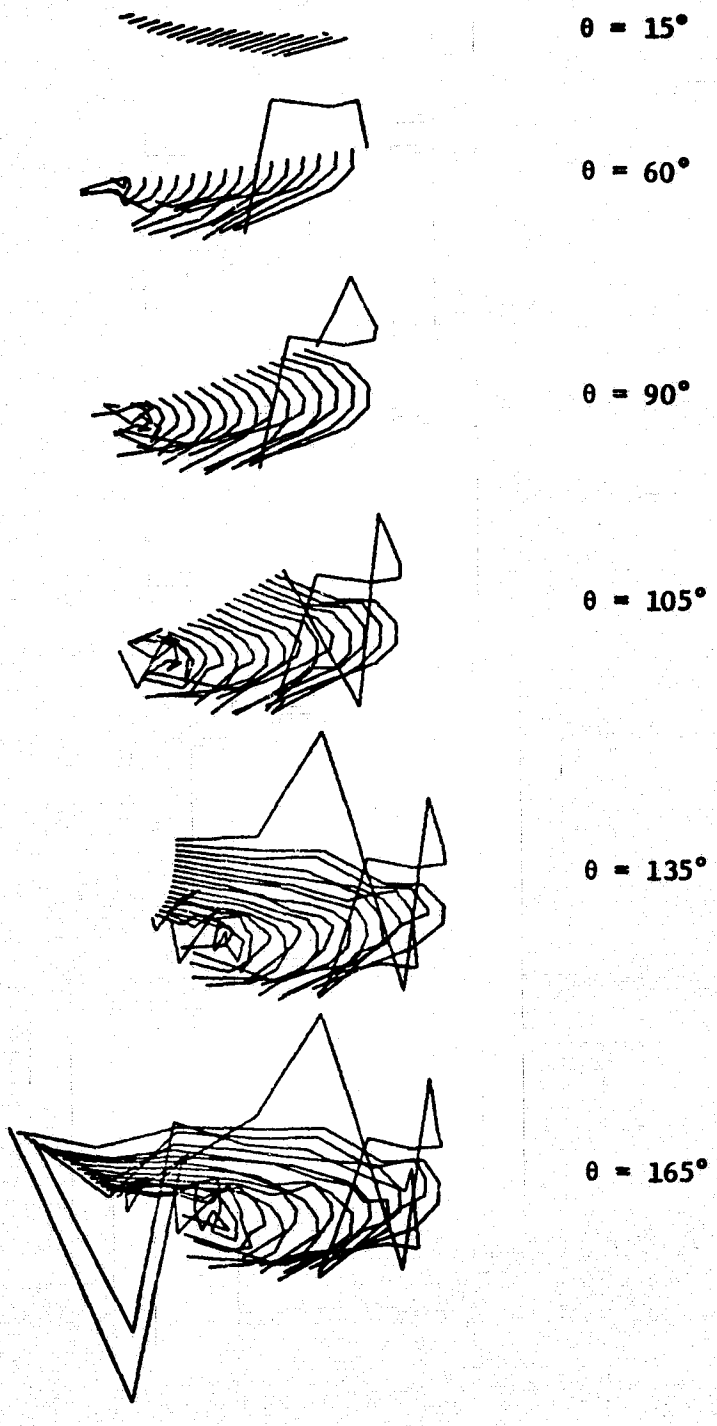

Figure 45. Propeller Vortex Wake Generation, $\Delta\theta = 7°$, $h_c = 10^{-6}$ ft.

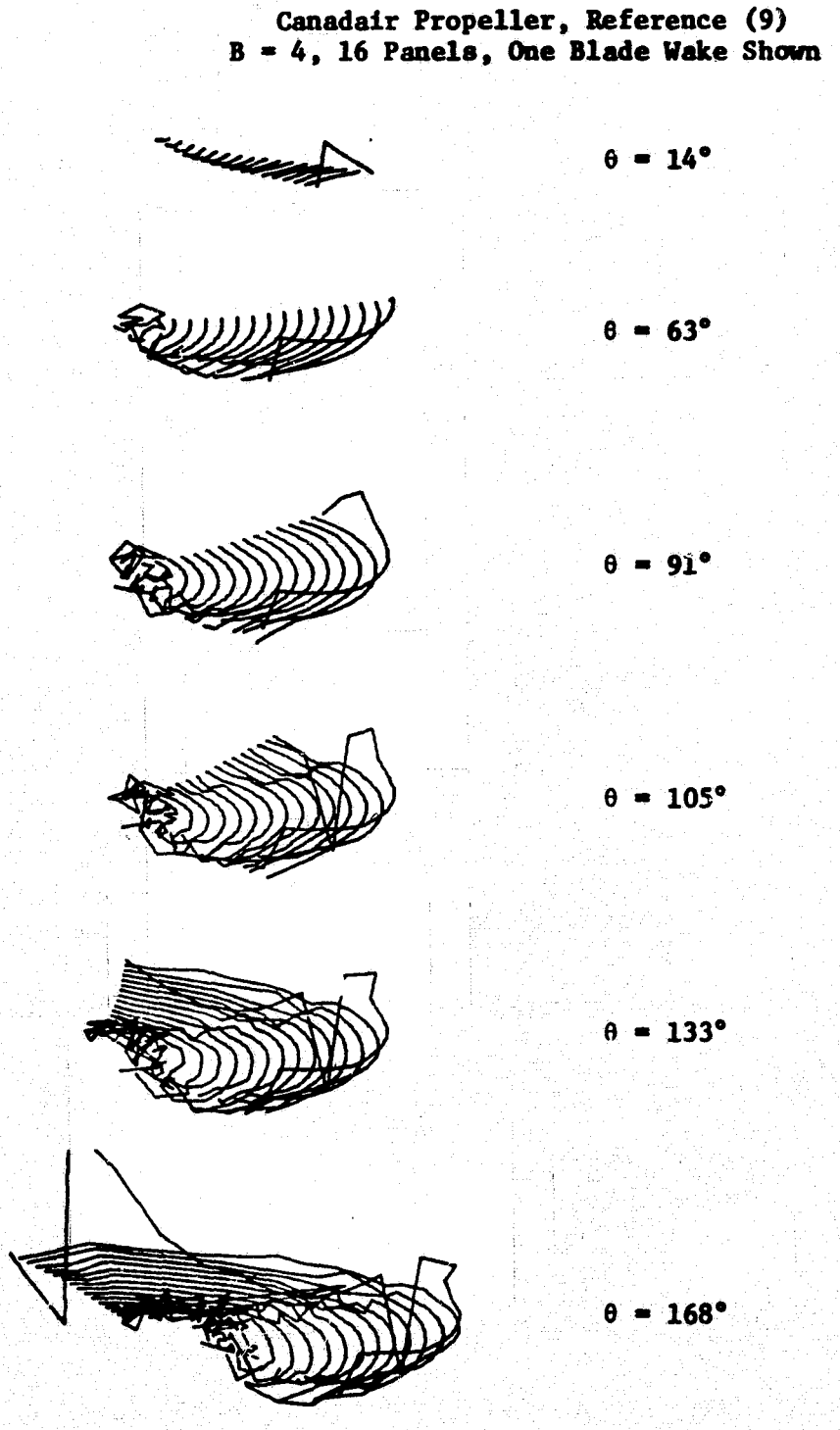

Figure 46. Propeller Vortex Wake Generation, $\Delta\theta = 3°$, $h_c = 10^{-6}$ ft.

Canadair Propeller, Reference (9)
B = 4, 16 Panels, One Blade Wake Shown

θ = 15°

θ = 60°

θ = 90°

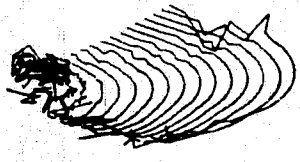

θ = 105°

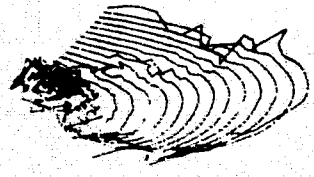

θ = 120°

Figure 47. Propeller Vortex Wake Generation, $\Delta\theta = 15°$, $h_c = 10^{-10}$ ft.

Canadair Propeller Reference (9)
B = 4, 16 Panels, One Blade Wake Shown

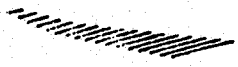

θ = 15°

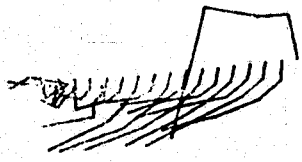

θ = 60°

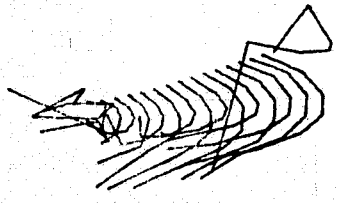

θ = 90°

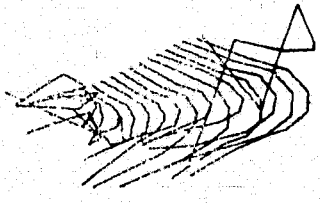

θ = 105°

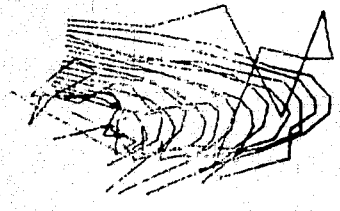

θ = 135°

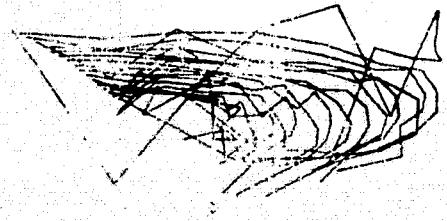

θ = 165°

Figure 48. Propeller Vortex Wake Generation $\Delta\theta = 15°$, Proportional Core.

Canadair Propeller, Reference (9)
B = 4, 16 Panels, One Blade Wake Shown

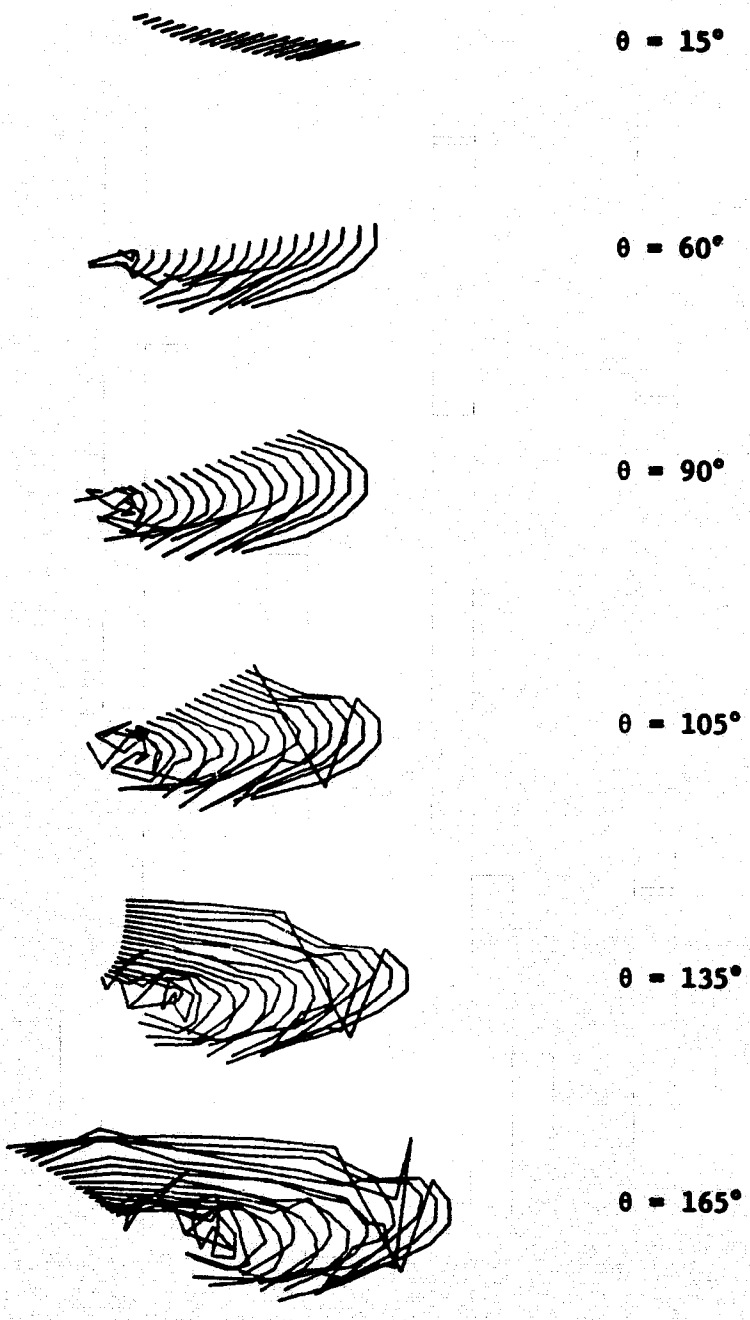

Figure 48. (cont.) Propeller Vortex Wake Generation, $\Delta\theta = 15°$, Proportional Core.

Canadair Propeller, Reference (9)
B = 4, 16 Panels, One Blade Wake Shown

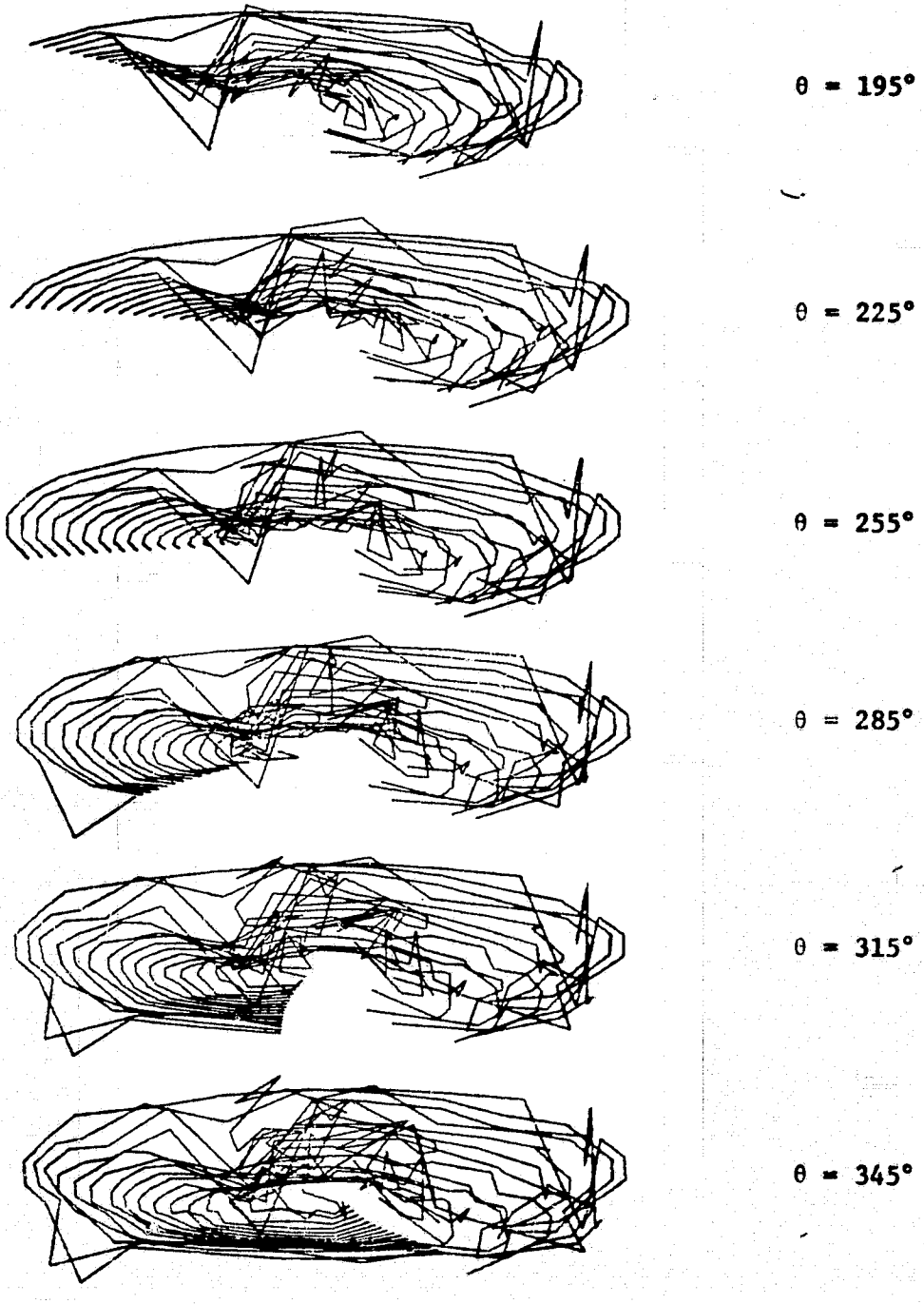

Figure 49. Effect of Spanwise Spacing and Blade Twist on Thrust Coefficient.

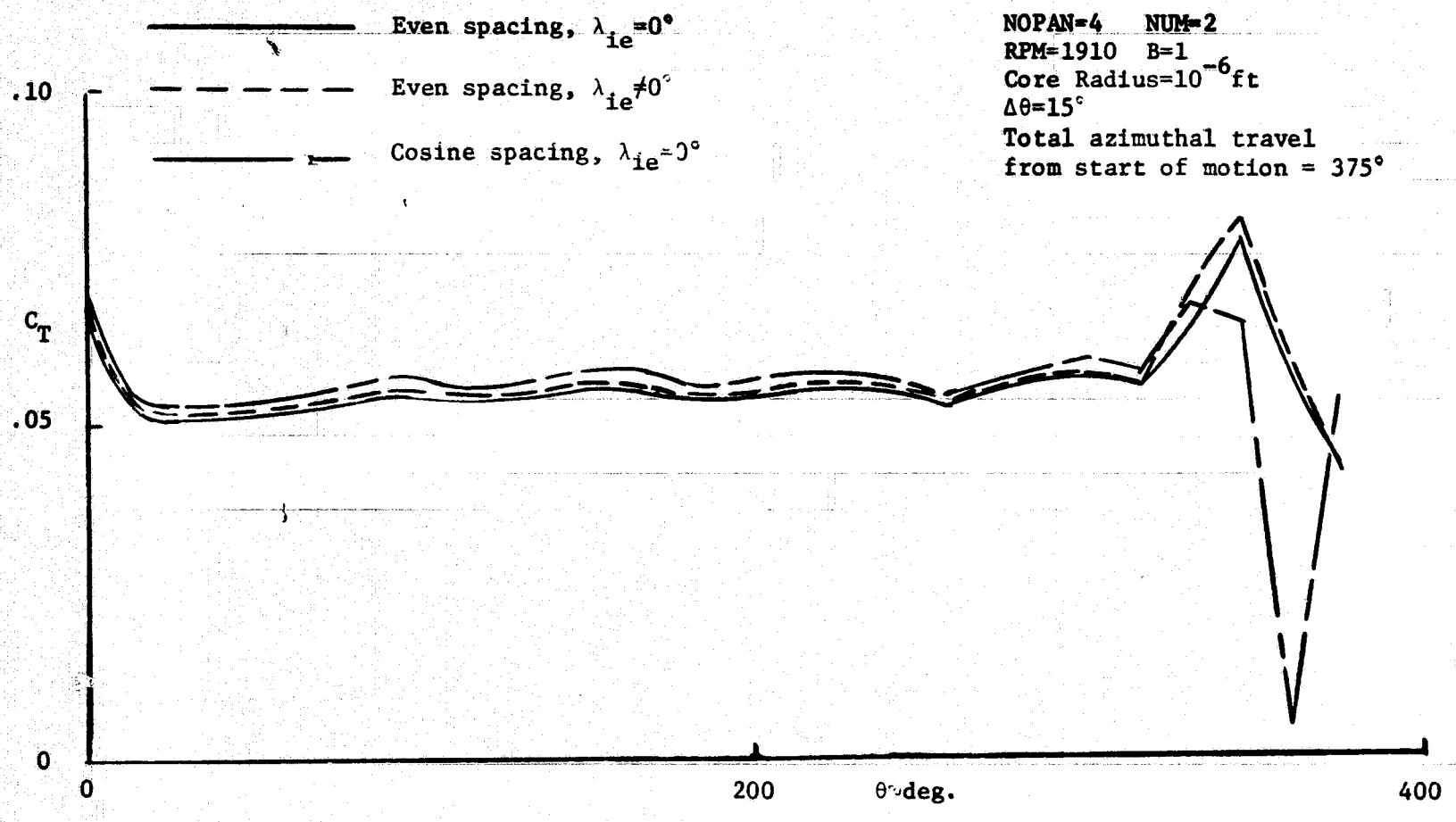

Figure 50. Effect of Spanwise Vortex Spacing on Spanwise Thrust Distribution.

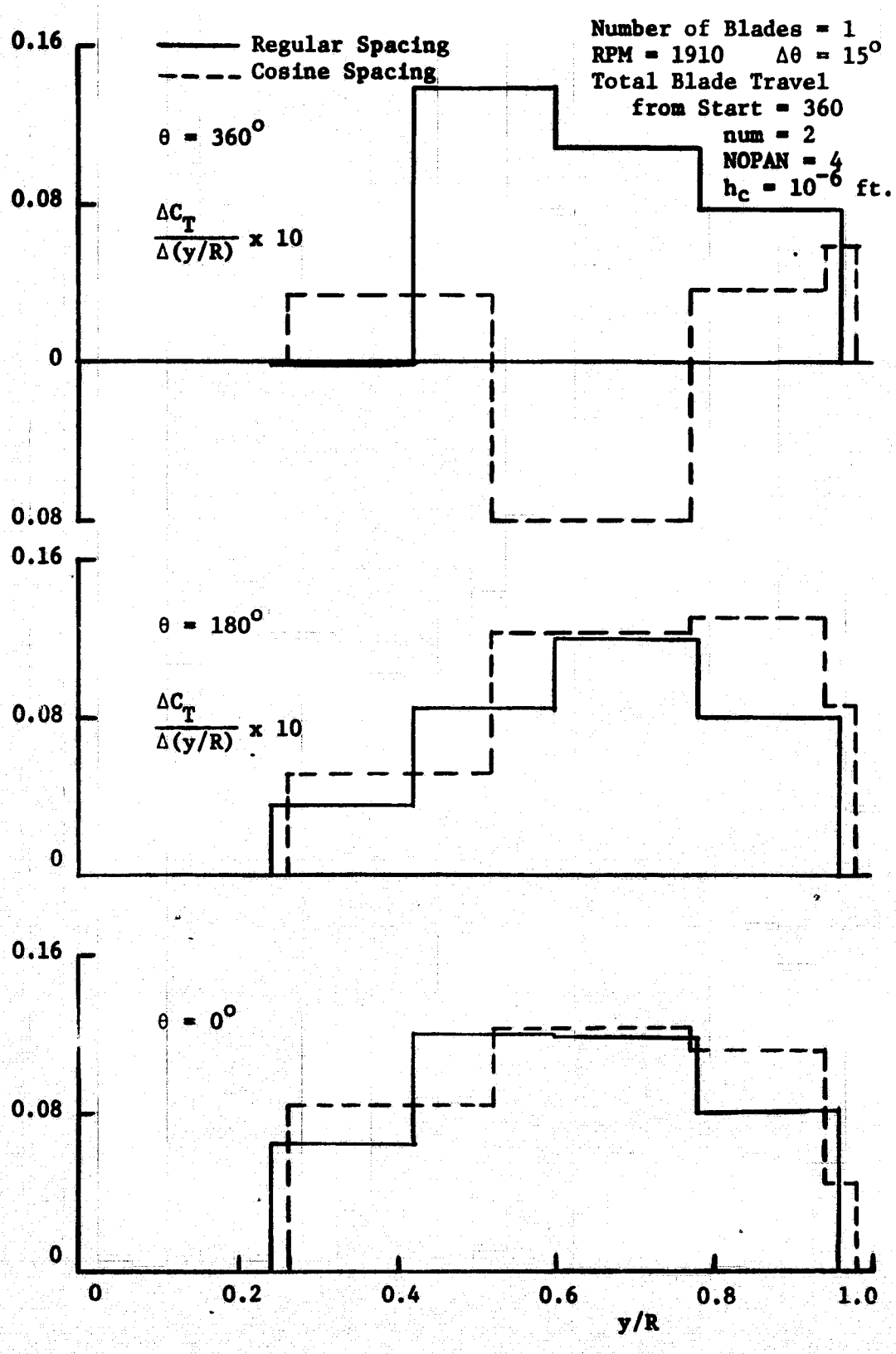

Figure 51. Effect of Spanwise Vortex Spacing on Effective Angle of Attack Distribution.

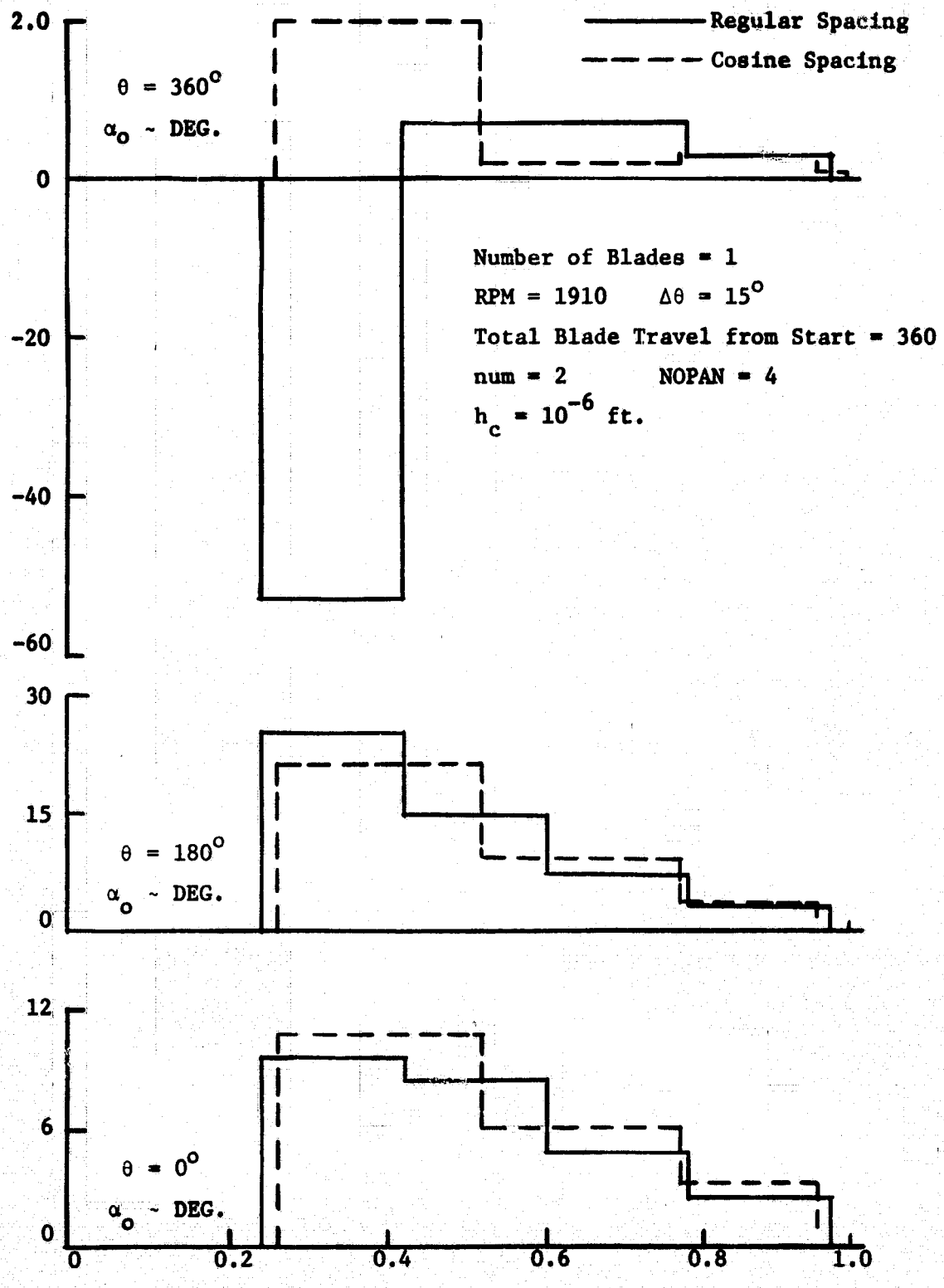

Figure 52. Time History of Performance of a Single Blade Propeller Starting Impulsively from Rest.

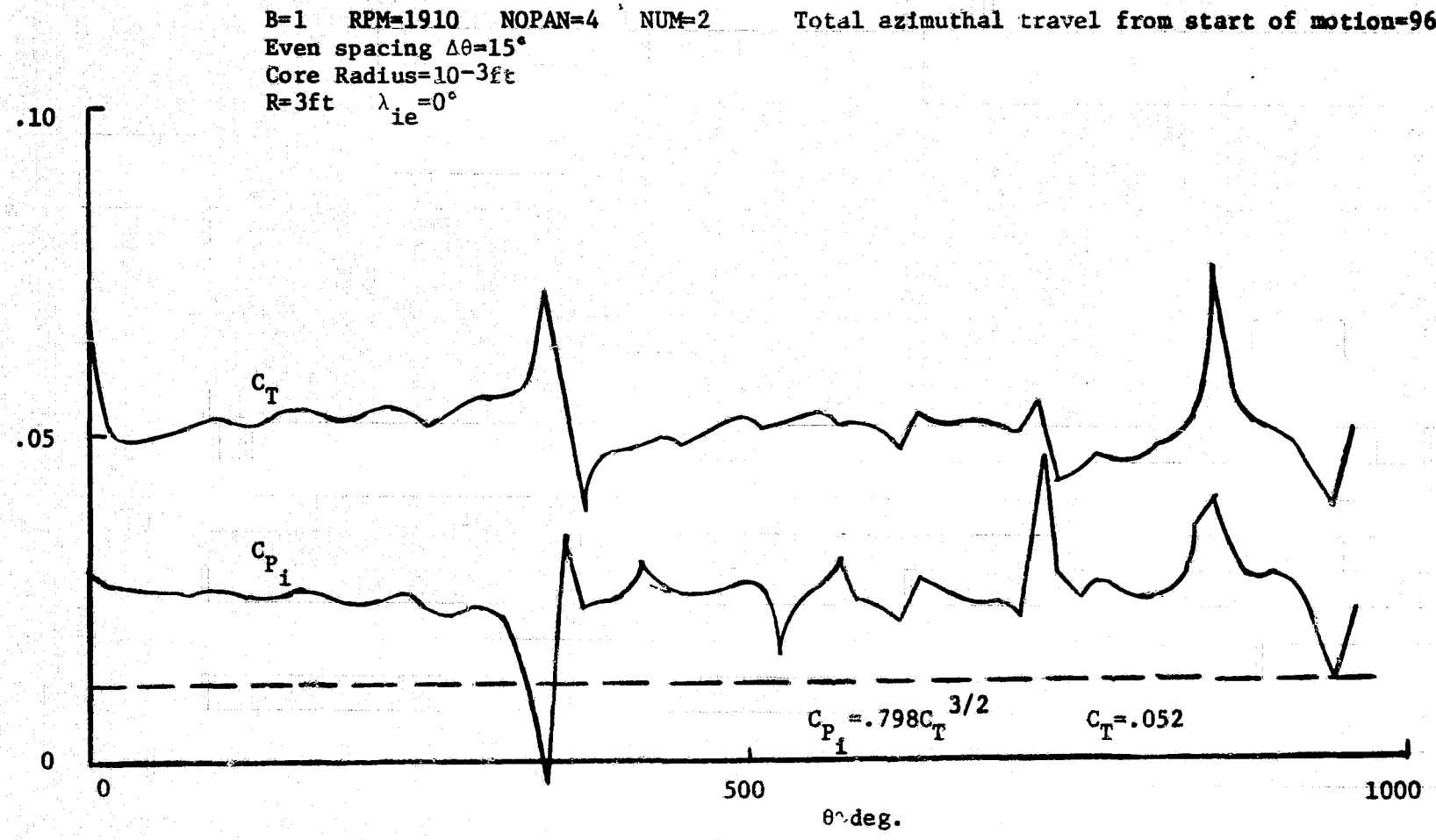

Figure 53. Time History of Performance of a Two Bladed Propeller Starting Impulsively from Rest.

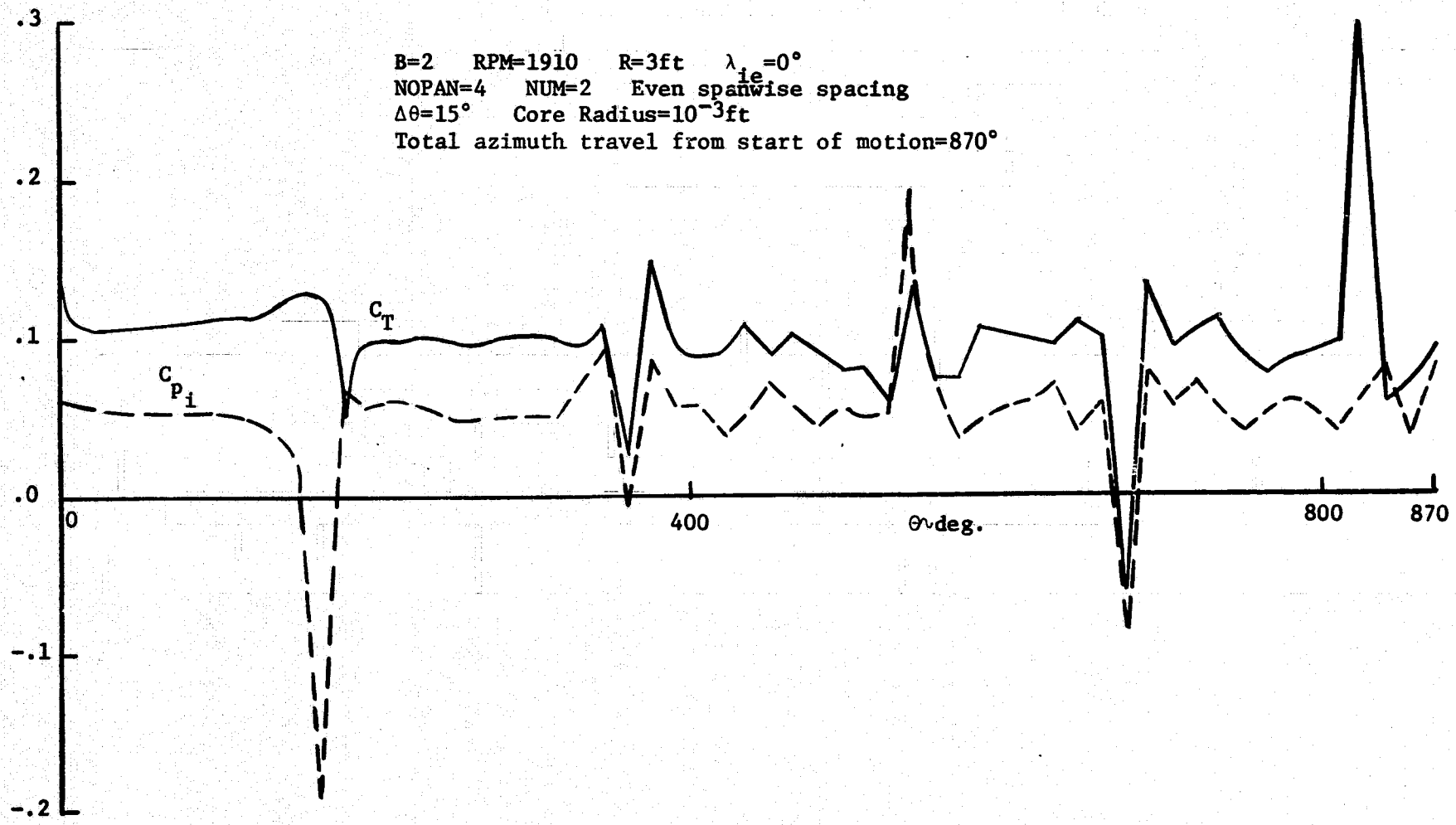

Figure 54. Propeller Vortex Wake Generation, $\Delta\theta = 15°$, $h_c = 10^{-3}$ ft.

Canadair Propeller, Reference (9)
B = 2, 4 Panels, One Blade Wake Shown

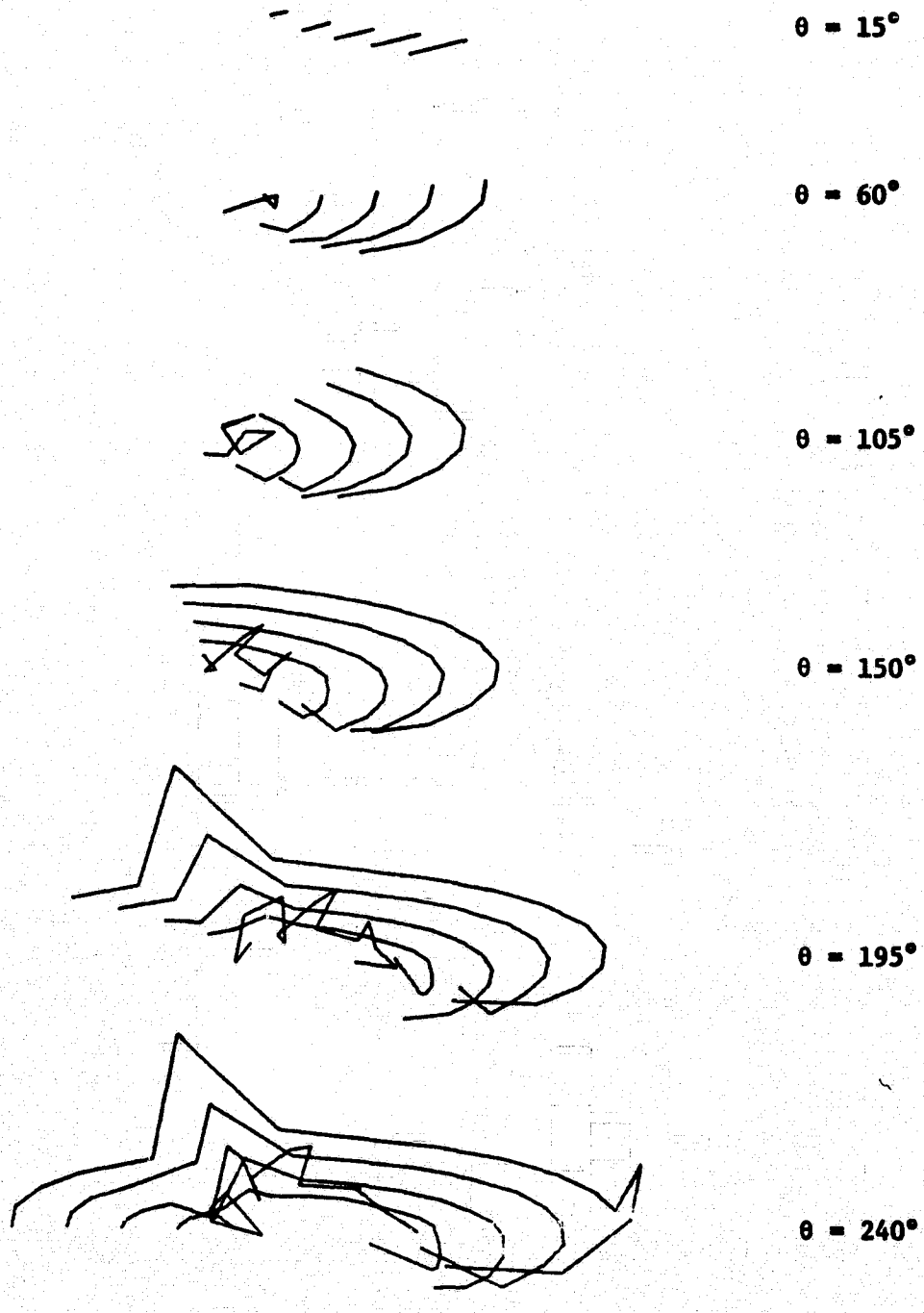

Figure 54. (cont.) Propeller Vortex Wake Generation, $\Delta\theta = 15°$, $h_c = 10^{-3}$ ft.

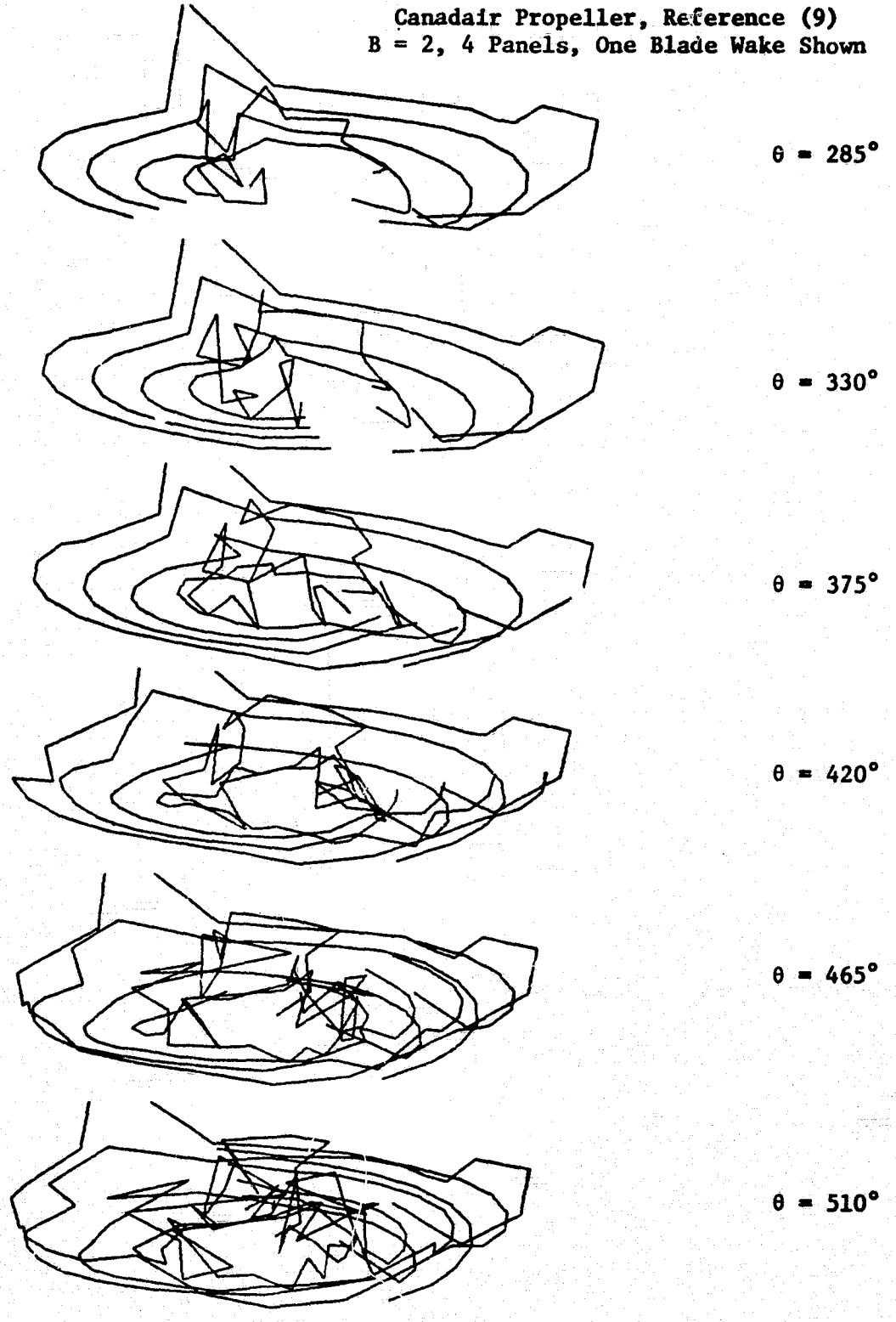

Figure 55. Effect of Curvature on Vortex Induced Velocity.